National Library
of Canada

Acquisitions and
Bibliographic Services Branch

395 Wellington Street
Ottawa, Ontario
K1A 0N4

Bibliothèque nationale
du Canada

Direction des acquisitions et
des services bibliographiques

395, rue Wellington
Ottawa (Ontario)
K1A 0N4

Your file Votre référence

Our file Notre référence

NOTICE

The quality of this microform is heavily dependent upon the quality of the original thesis submitted for microfilming. Every effort has been made to ensure the highest quality of reproduction possible.

If pages are missing, contact the university which granted the degree.

Some pages may have indistinct print especially if the original pages were typed with a poor typewriter ribbon or if the university sent us an inferior photocopy.

AVIS

La qualité de cette microforme dépend grandement de la qualité de la thèse soumise au microfilmage. Nous avons tout fait pour assurer une qualité supérieure de reproduction.

S'il manque des pages, veuillez communiquer avec l'université qui a conféré le grade.

La qualité d'impression de certaines pages peut laisser à désirer, surtout si les pages originales ont été dactylographiées à l'aide d'un ruban usé ou si l'université nous a fait parvenir une photocopie de qualité inférieure.

Canada

UNIVERSITY OF ALBERTA

THE QUANTIFICATION OF BRAIN IRON USING PROTON MRI

BY

FRANK QING YE

A THESIS SUBMITTED TO THE FACULTY OF GRADUATE STUDIES AND RESEARCH IN PARTIAL FULFILLMENT OF THE REQUIREMENTS FOR THE DEGREE OF DOCTOR OF PHILOSOPHY

IN

MEDICAL SCIENCES

DEPARTMENT OF BIOMEDICAL ENGINEERING

EDMONTON, ALBERTA

FALL 1995

ISBN 0-612-06312-7

Canada

University of Alberta
Edmonton

Division of Neurology

Canada T6G 2B7

2E3 Walter C. Mackenzie Health Sciences Centre
8440 - 112 Street

July 11, 1995

Division of Neurology
Phone [illegible]
Fax (403) 492-[illegible]

Drs. [illegible]
Fax [illegible]

For urgent Neurology
consultation 492-[illegible]
request neurologist on call

M.H. Brooke
Director
MD FRCPC
Tel 492-[illegible]

[illegible]
MD Diplomate ABPN
Tel 492-[illegible]

[illegible]
MD FRCPC
Tel 492-[illegible]

D.S. [illegible]
BSc MD FRCPC
Tel 492-[illegible]

[illegible]
MD PhD FRCPC
Tel 492-[illegible]

R. [illegible]
MSc PhD
Tel 492-[illegible]

W.R.W. Martin
MD FRCPC
Tel 482-8032

G. Monckton
MD FRCPC
Tel 492-[illegible]

A.M.W. [illegible]
MD FRCPC
Tel 492-[illegible]

[illegible] Roberts
MD FRCPC
Tel 450-7[illegible]
482-8932
Fax 450-7633

P. Stenerson
MD, FRCPC
Tel: 492-1926

K.G. Warren
MD, FRCP(C)
Tel. 492-6298

EEG Lab 492-6856

Re: **Frank Qing Ye**
Ph. D. Thesis

This letter confirms my permission for the use of the following two manuscripts in Mr. Ye's thesis. These papers are both currently under review for publication in peer-reviewed journals.

1. Martin WRW, Ye FQ, Allen PS. Increasing striatal iron content with aging: a risk factor for free radical mediated neuronal damage. Submitted to *Neurology*.

2. Ye FQ, Allen PS, Martin WRW. Basal ganglia iron content in Parkinson's disease measured with magnetic resonance. Submitted to *Movement Disorders*.

Sincerely,

W. R. Wayne Martin, M.D., F.R.C.P.C.
H.M. Toupin Professor of Neurology

University of Alberta
Edmonton

Canada T6G 2G3

Department of Biomedical Engineering
Faculty of Medicine

10-102 Clinical Sciences Building
Telephone (403) 492-6330
Fax (403) 492-8239
E-mail biomed.eng@ualberta.ca
WEB site http www.biomed.ualberta.ca

10 July 1995

To Whom It May Concern

Re: Ph.D. Thesis of Frank Q. Ye

This letter is to confirm formally that it is entirely acceptable to me that Frank Ye use the material from our joint publications in his Ph.D. thesis. I trust this statement satisfies your requirements for co-authorship permission.

Sincerely,

P. S. Allen

Peter S. Allen
Professor and Chair

PSA:mg

UNIVERSITY OF ALBERTA

LIBRARY RELEASE FORM

NAME OF AUTHOR: Frank Qing Ye

TITLE OF THESIS: The Quantification of Brain Iron Using Proton MRI

DEGREE: Doctor of Philosophy in Medical Sciences

YEAR THIS DEGREE GRANTED: 1995

Frank Q. Ye

Frank Q. Ye
715#, 8515-112 Street
Edmonton, Alberta
T6G 1K7

Date: July 12, 1995

University of Alberta

Faculty of Graduate Studies and Research

The undersigned certify that they have read, and recommend to the Faculty of Graduate Studies and Research for acceptance, a thesis entitled THE QUANTIFICATION OF BRAIN IRON USING PROTON MRI submitted by FRANK QING YE in partial fulfillment of the requirements for the degree of DOCTOR OF PHILOSOPHY in MEDICAL SCIENCES.

Dr. P. S. Allen (Supervisor)

Dr. W. R. W. Martin

Dr. R. E. Snyder

Dr. D. J. Griffiths

Dr. D. G. Hughes

Dr. R. J. Ordidge (External Examiner)

Date: 21 June 95

To Kui, and to our parents,

for all their love and support.

ABSTRACT

A brain iron quantification technique is presented for measuring the variations of basal ganglia iron content in Parkinson's disease, using magnetic resonance imaging. The technique is based on measuring the interecho time dependence of the transverse relaxation enhancement of water protons that is brought about by the paramagnetic brain iron. This interecho time dependence is postulated to be the consequence of the heterogeneous cellular sequestration of brain iron, and is exploited to provide an index for the tissue iron content.

The postulated mechanism of the interecho-time-dependent transverse relaxation enhancement was systematically studied in a paramagnetic suspension of red blood cells and in excised brain tissue. The mechanism, when incorporated into a computer simulation of the experimental data, reproduced the enhancement dependencies on the interecho time, on the cellular magnetization difference, and on changes in cell shape. The interecho-time-dependent enhancement, δR_{2app}, in excised basal ganglia grey matter was found to correlate with independent measurements of the tissue iron concentration ($r=0.81$, $p<0.001$).

An imaging sequence was developed for the in-vivo measurement of δR_{2app} so that a regional index for brain iron could be obtained. When tested on phantoms over a relevant but limited range of magnetization difference values, δR_{2app} demonstrated a linear dependence on the magnetization difference with a sensitivity of $\sim 2\ s^{-1}A^{-1}m$. When tested on a group of age-range-limited healthy volunteers, that index proved capable of distinguishing two iron-rich basal ganglia structures, namely, the globus pallidus and the putamen, from each other and from other structures of lesser iron content.

In a preliminary clinical application, twenty healthy volunteers whose age-range spanned five decades were studied for the age-related iron accumulation, and twelve patients with Parkinson's disease were compared with age-matched controls. The volunteers displayed an age-correlated increase in the regional iron index in the putamen ($r=0.76$, $p<0.001$) and in the caudate head ($r=0.69$, $p<0.001$). The patients displayed increases in the iron index of 42% in the putamen ($p<0.05$) and 33% in the globus pallidus ($p<0.05$). These regional iron indices also correlated with the clinical measures of disease severity ("r" ranges from 0.64 to 0.76, $p<0.05$).

ACKNOWLEDGEMENT

I would like to thank my supervisor, Dr. Peter S. Allen, for his supervision over the past six years. He has been very supportive in many aspects of my work and life. I have learnt a great deal from him, especially in presenting ideas and writing manuscripts.

I am grateful to Dr. W. R. Wayne Martin who, in the past four years, acted like a co-supervisor in my research. He not only provided supervision in the neurological aspects of this research, but also had complete confidence in me that provided encouragement to overcome a few difficulties in this project.

Dr. Richard E. Snyder kindly made many grammatical corrections and good suggestions to my thesis prior to its submission to the examining committee. Thanks are extended as well to the other members in the examining committee who also made good suggestions for the final revision of this thesis.

Various technical assistance should be acknowledged. Joanne Hodder carried out the clinical assessment and provided nursing care to the patients and to the elderly controls at the time of the imaging study. Her delightful personality and excellent working skills helped us to recruit a large pool of volunteers willing to take part in this study. Damyanti Bhardwaj assisted in preparation of the red blood cell suspensions and in dissecting the samples of grey matter tissue. Dan Gheorghiu wrote the pulse program code on the Philips system for implementation of the modified spin echo imaging sequence. Brain tissue specimens were kindly provided by the National Neurological Research Specimen Bank, VAMC, Los Angeles. The brain iron analysis using atomic absorption spectrometry was performed by Dr. Audette of the Dept. of Laboratory Medicine.

I am grateful to the volunteers who took part in this study, particularly to those patients with Parkinson's disease. Though their names are not to be revealed, their contribution to this study is to be remembered.

Quite a few people in our NMR laboratory provided friendly support to my work in the past six years. Dr. Gang Zhu, when he was with this group, often shared his research experience with me and offered good advice. Dan Doran was always available when I needed a trouble shooter for the Bruker spectrometer. Christian Beaulieu helped

to measure the water diffusion coefficients in some of my samples to verify the values used in the simulation. He and the other fellow graduate students in the lab, Pat, Alan, and Frances, were valuable resources for experimental experiences and stimulating discussion. Dr. Qing-an Meng provided a few good suggestions.

Many other people in the department also gave me all sorts of help at various occasions. Their names will be remembered, Carol, Rosie, Maisie, Ivy and Edmund, Chen and Ian, Chris, Mark, Richard, Ravi, Karim, ...

The Department of Biomedical Engineering (formerly known as the Department of Applied Sciences in Medicine) and Dr. Peter S. Allen kindly provided me a research assistantship during the six years of my graduate study.

Finally, I must thank Kui, my sweetheart. Her love and support have made my success possible and more enjoyable. Our parents, sisters, and brothers, who live overseas, were always supportive and always wished us happiness and success.

TABLE OF CONTENTS

LIST OF TABLES

LIST OF FIGURES

LIST OF SYMBOLS AND ABBREVIATIONS

$\mathbf{B}$	Net magnetic field (induction) vector
B_d	z component of the dipolar magnetic field
$\mathbf{B}_{loc}$	Dipole magnetic field of a magnetic moment
B_{L1} , B_{L2}	Effective magnetic field (z component) representing all sources of magnetism inside the first/second sphere of Lorentz
$<B_{L2}>$	Average field over the second sphere of Lorentz
$\mathbf{B}_o$	External static magnetic field vector
B_o	Magnitude of $\mathbf{B}_o$
$\mathbf{B}_{eff}$	Effective magnetic field vector in the rotating frame
B_p	Effective (z component) magnetic field at a proton site, p, in a cell suspension
$B^{(j)}(r_k)$	Effective (z component) magnetic field experienced by the j^{th} spin at location $\mathbf{r}_k$ prior to its k^{th} random-walk jump
$\mathbf{B}_1$	Externally applied radio-frequency magnetic field vector
B_1	Amplitude of $\mathbf{B}_1$ field
CD	Caudate nucleus
CPMG	Carr-Purcell-Meiboom-Gill
CSF	Cerebrospinal fluid
D	Diffusion coefficient
D_e, D_i	Extra/Intra cellular water diffusion coefficient
DyDTPA	Dysprosium-diethylenetriaminepentaacetic acid
$\mathbf{e}_x$, $\mathbf{e}_y$, $\mathbf{e}_z$	Cartesian unit vectors
E	Interaction energy
E_ℓ	Spin energy of an energy eigenstate
FID	Free induction decay

G	Magnitude of magnetic field gradient
GdDTPA	Gadolinium-diethylenetriaminepentaacetic acid
GP	Globus pallidus
$\hbar$	Planck's constant divided by 2π
$\mathcal{H}$	Hamiltonian
$\mathcal{H}_d$	Dipolar Hamiltonian of a spin pair
HD	Huntington's disease
$HO^{\bullet}$	Hydroxyl free radical
H_2O_2	Hydrogen peroxide
$\mathbf{I}$	Spin (angular moment) operator
I	Spin quantum number
I_z	z component spin quantum number
$\hat{I}^+$, $\hat{I}^-$	Raising/Lowering spin operator
$\hat{I}_x$, $\hat{I}_y$, $\hat{I}_z$	Cartesian components of spin operator
$\mathbf{J}$	Angular momentum
J_o, J_1, J_2	Spectral density functions
k	Boltzmann's constant
L-dopa, levodopa	Levodihydroxyphenylalanine
ℓ	An integer or half-integer
M	Longitudinal magnetization
MRI	Magnetic resonance imaging
$\mathbf{m}$	Net nuclear magnetization of a spin ensemble
m	Magnitude of net nuclear magnetization
m_x, m_y, m_z	Components of net nuclear magnetization

m_{xy}	Magnitude of transverse nuclear magnetization
m_o	Magnitude of equilibrium nuclear magnetization of a spin ensemble
MHz	Megahertz
MAO	Monoamine oxidase
$MPDP^+$	1-methyl-4-phenyl-2,3-dihydropyridinium
MPP^+	$MPDP^+$, the 1-methyl-4-phenylpyridinium species
MPTP	1-methyl-4-phenyl-1,2,3,6-tetrahydropyridine
MR	Magnetic resonance
MRI	Magnetic resonance imaging
MSA	Multiple system atrophy
NMR	Nuclear magnetic resonance
N	Spin population
n	Number of net aligned (relative to $\mathbf{B}_o$) proton spins in an ensemble
n_o	Number of net aligned (relative to $\mathbf{B}_o$) proton spins in an equilibrium ensemble
N_α , N_β	Spin population in the specified orientation
N_α^o, N_β^o	Spin population in the specified orientation at equilibrium
NAD^+	nicotinamide adenine dinucleotide
N_s	Number of water proton spins used in simulating relaxation enhancement
O_2^-	Superoxide
p_a, p_b	Relative water population in the hydrated/bulk phase
p_e , p_i	Relative spin population in extra/intra cellular compartment
P_{enter} , P_{exit}	Entrance/Exit probability of traversing the RBC membrane
P_{ve} , P_{vi}	Relative volume of extra/intra cellular compartment

P_{vs}	Volume fraction of magnetic spheres in solution
PBS	Phosphate buffered saline
PD	Parkinson's disease
PDI	Peripheral decarboxylase inhibitors
PDRS	Parkinson's disease rating scale
PM	Putamen
PS	Parkinsonian syndromes
$\mathbf{r}$	displacement vector
r, θ, ϕ	Spherical-polar coordinates of displacement vector
r	Correlation coefficient, or Magnitude of $\mathbf{r}$
R_1	Longitudinal relaxation rate, inverse of T_1
R_2	Transverse relaxation rate, inverse of T_2
R_2^*	Rate constant , inverse of T_2^*
R_{2app}	Apparent Transverse relaxation rate, inverse of T_{2app}
R_2°	Apparent Transverse relaxation rate in cell lysate
RBC	Red blood cell
RF	Radio frequency
ROI	Region of interest
SN	Substantia nigra
SND	Striatonigral degeneration
SOD	Superoxide dismutase
T	Absolute temperature, or Tesla
T_1	Longitudinal relaxation time
T_2	Transverse relaxation time

T_{2app}	Apparent transverse relaxation time obtained at a specific interecho time in a spin-echo or CPMG sequence.
T_2^*	Time constant characterizing decay of FID in an inhomogeneous static magnetic field
TE	Echo time
TH	Thalamus
TR	Sequence repetition time
UPDRS	Unified Parkinson's disease rating scale
W, $W_{\alpha\beta}$, $W_{\beta\alpha}$	Probability of spin transition rate between energy eigenstates
w_e, w_i	Extra/Intra cellular water concentration
α, β	Eigenstate of a proton spin orienting parallel/antiparallel to the static magnetic field
α_c	Demagnetizing factor determined by the shape of a cell surface
α_s	Demagnetizing factor determined by the shape of a sample surface
δt	Time between consecutive random-walk jumps
χ_e, χ_i	Volume magnetic susceptibility of extra/intra cellular compartment
χ_m	Molar magnetic susceptibility
$\delta\omega$	Difference in the average proton resonance frequency between intra and extra cellular compartments
$\Delta\omega$	Characteristic variation of field perturbation in units of the proton Larmor frequency
ΔB	Magnetic field inhomogeneity
ΔB_{os}	Variance of field variation across the sample of interest
ΔM	Magnetization difference
ΔR_2	Difference in apparent transverse relaxation rate between an RBC suspension sample and the corresponding lysate sample

δR_{2app}	Difference in R_{2app} between two measurements using different values of the interecho time. It is a measure of the interecho time dependent relaxation enhancement.
ΔR_{2app}	An imaging-based, regional δR_{2app} that has been corrected by an in-slice background subtraction to reduce interscan variations.
ΔR_2^{ex}	Enhancement that is brought about by two-site proton exchange on the apparent transverse relaxation rate determined by means of a CPMG sequence.
$\Delta\Phi$	Phase accumulation
Δ_{180}	Interecho time (or refocussing interval) in a CPMG sequence
ε	A fitting parameter
Φ	Phase of a proton spin or a spin isocromat
γ	Gyromagnetic ratio
$\boldsymbol{\mu}$	Magnetic moment
μ_o	The permeability of free space
λ	radius
ρ	A rate constant that represents an empirical characterization of the interecho time dependence of R_{2app}
σ_G	Variance of internal gradient distribution in a sample containing heterogeneous susceptibility
τ	Correlation time characterizing the transmembrane diffusion in cell suspensions.
τ_c	Rotational diffusion correlation time characterizing internal molecular motion
τ_D	Characteristic diffusive correlation time of water molecules in a sample containing heterogeneity in susceptibility
τ_i	Average life time of intracellular water protons in cell suspensions
ω	Frequency of the radiofrequency B_1 field
$<\omega^2>$	The second moment of the line shape of non-moving spin pairs

ω_o	Larmor frequency
$\psi(t)$	Wave function at time t
Π	Torque
Ω	Angular velocity
$(90°)_x$	90° RF pulse in the x direction in the rotating frame
$(180°)_y$	180° RF pulse in the y direction in the rotating frame

CHAPTER 1

Introduction

1.1 Overview of the Thesis

The enhancement of the nuclear magnetic resonance (NMR) relaxation rate of water protons by paramagnetic substances has become an increasingly important issue in in-vivo magnetic resonance imaging (MRI). The clinical importance of this enhancement can be seen in the imaging of the basal ganglia of the brain (1-2) and in the imaging of the liver (3), since in both organs naturally accumulated or pathologically exaggerated iron deposition is present. This enhancement is also essential to the application of paramagnetic MRI contrast agents (4-5) and in functional MRI studies of the brain (6-7). Although relaxation enhancement of the protons of solvent water by a paramagnetic solute through the electron-proton spin interaction was studied and analyzed quantitatively many years ago (8-9), our current understanding of relaxation enhancement in tissue remains largely qualitative or semi-quantitative (10-12). One of the difficulties in achieving a quantitative understanding of enhancement in tissue arises from the complicated heterogeneous distribution of paramagnetic substances in that milieu, either accumulating naturally or administered exogenously. In the study of relaxation enhancement caused by iron in the brain, the lack of a thorough and quantitative understanding of the relaxation mechanism has hindered the development of MRI techniques suitable for reliable in-vivo iron quantification. In-vivo techniques for iron quantification would be of particular value for the clinical evaluation of neurodegenerative disorders (13-18) such as Parkinson's disease and Huntington's disease.

This study was motivated by the interest of measuring changes in brain iron in Parkinson's disease. The overall objective of this study is, through quantitative studies of the paramagnetic relaxation enhancement of water protons, to increase our knowledge of the enhancement effect and to develop and apply MRI techniques for the specific in-vivo quantification of brain iron.

The relaxation enhancement effect of brain iron was suggested by the signal hypointensity of some iron-rich basal ganglia brain nuclei observed in heavily T_2-weighted images obtained at high magnetic field strengths of 1.5 T (1-2). While signal hypointensity can help to delineate those iron-rich brain nuclei in T_2-weighted images and may also give a coarse measure of regional iron changes, a more precise quantitative measure is desirable for the clinical assessment of brain iron concentrations. Although the easily measurable transverse relaxation time, T_2, is believed to be affected by tissue iron, it does not correlate well with iron concentration in brain tissues (19-20). Reliable quantification of brain iron requires relaxation measurements that are more specific, possibly arising through a separation of the iron-related enhancement from relaxation that is largely independent of iron.

One such relaxation measurement is proposed and evaluated in this study. It exploits the interecho time dependence of the apparent transverse relaxation rate to characterize the relaxation enhancement. This enhancement and its dependence on the interecho time is postulated as arising from the heterogeneous brain iron distribution.

The Ph.D. programme reported in this thesis consists of three parts. They are first, an experimental evaluation and theoretical simulation of the relaxation enhancement in paramagnetic suspensions of red blood cells. In this model system, a cell membrane separates the different paramagnetic susceptibilities. Secondly, the enhancement of transverse relaxation in brain tissue, both in-vitro and in-vivo, was

evaluated to determine the improvement it provided over T_2 alone for the quantification of brain iron, where the iron was sequestered in glia. Thirdly, a preliminary clinical evaluation of the proposed iron-quantification technique was carried out to study iron accumulation in normal aging and in Parkinson's disease.

To have a quantitative theoretical understanding about relaxation enhancement that arises from a cell-membrane-separated susceptibility difference, a numerical relaxation model was developed for a paramagnetic suspension of red blood cells. The numerical simulation reproduced the experimentally-observed enhancement dependencies on the interecho time, on the cellular magnetization difference, and on the changes in cell shape. This simulation is reported in Chapter 2.

To evaluate the enhancement of transverse relaxation as a measure of iron deposition in brain tissue, experiments were carried out on excised brain tissue as well as on age-range-limited living brain to minimize deposition factors other than brain structure differences. In the in-vitro study, it was possible to perform a correlation analysis between the relaxation enhancement and an independent atomic absorption spectrometry measure of tissue iron concentration. This is reported in Chapter 3. In the in-vivo study, it was possible to test statistically the ability of relaxation enhancement to differentiate the iron-rich brain nuclei in living brain. This test is described in Chapter 4.

To evaluate the clinical potential of the proposed iron-quantification technique, pilot studies were carried out on a group of normal volunteers whose age-range spanned five decades (see Chapter 5) and on a group of patients with Parkinson's disease (see Chapter 6). A correlation was found between the regional iron-index derived from relaxation enhancement and the age of the normal volunteers, and between the iron-

index and the clinical scale disease severity score in the group of patients with Parkinson's disease.

The remainder of this chapter introduces background material relevant to NMR; to water proton relaxation properties important to MRI; to brain iron and its influence on MRI contrast; and to Parkinson's disease.

1.2 Water Proton NMR Relaxation in MRI

In clinical MRI, the longitudinal relaxation time and transverse relaxation time of water protons are two of the most important tissue characteristics which determine image contrast. An advantage of MRI is that image contrast, which is largely dependent upon the relaxation time of water protons in soft tissue, can be manipulated through the selection of the imaging pulse sequence and the timing parameters so as to achieve optimal tissue and lesion separation. This section provides the basic concepts and theories about NMR, and particularly about water proton relaxation.

1.2.1 Basics of Nuclear Magnetic Resonance

1.2.1.1 Basics of Macroscopic Nuclear Magnetization

Nuclear magnetic resonance is a quantum mechanical phenomenon (21-24). Any atomic nucleus that possesses a non-zero spin angular momentum in its ground state, $\mathbf{I}\hbar$, also possesses a magnetic moment, $\gamma\hbar\mathbf{I}$, where γ is known as the gyromagnetic ratio and is unique to each nuclear species, $\hbar$ is Planck's constant divided by 2π, and $\mathbf{I}$ is the spin angular moment operator. The quantum number for the spin angular momentum operator, I, can only have an integer or half integer value. When placed in a magnetic field, the possible orientations of the spin are defined by the discrete quantum number $I_z = \ell$, where ℓ = -I, -I+1, ..., I-1, I. Here, I_z is the eigenvalue

of the z-component of the spin angular momentum and the z direction has been assigned along the external magnetic field $\mathbf{B}_o$. Each of these possible orientations corresponds to a different level of magnetic energy, $E_\ell = -\gamma\hbar\ell B_o$, where B_o is the magnitude of $\mathbf{B}_o$.

For a bulk sample containing numerous nuclear spins, the population distribution of the spins at equilibrium follows the Boltzmann law. Thus, at equilibrium the magnetization in the z direction of a sample containing N spins is

$$m_o = N\gamma\hbar \frac{\sum_{\ell=-I}^{I} \ell \exp(\gamma\hbar\ell B_o / kT)}{\sum_{\ell=-I}^{I} \exp(\gamma\hbar\ell B_o / kT)}, \qquad [1.1]$$

where k is the Boltzmann constant and T is the absolute temperature. Because the nuclear magnetic energy ($\gamma\hbar\ell B_o$) is much smaller at room temperature than kT, Eq. [1.1] can be simplified, using the high temperature expansion, as

$$m_o = N\gamma\hbar \frac{\sum_{\ell=-I}^{I} \ell (1 + \gamma\hbar\ell B_o / kT)}{\sum_{\ell=-I}^{I} (1 + \gamma\hbar\ell B_o / kT)} \cong \frac{N\gamma^2\hbar^2 I(I+1)B_o}{3kT}. \qquad [1.2]$$

The magnitude of the macroscopic nuclear magnetization is proportional to $\gamma^2\hbar^2 I(I+1)$, the square of the magnitude of the nuclear spin moment, to N, to B_o, and to 1/T.

1.2.1.2 Bloch Equations and Rotating Frame

Despite the quantum mechanical nature of the nuclear magnetic moment, the behavior of the macroscopic nuclear magnetization may be understood in terms of classical physics. To be consistent with the main body of this work, this introduction

will remain within the scope of classical physics and consult quantum mechanics only when necessary.

The behavior of the nuclear magnetization in a magnetic field follows the Bloch equations

$$\frac{d\mathbf{m}}{dt} = \gamma(\mathbf{m}\times\mathbf{B}) + \frac{m_o - m_z}{T_1}\mathbf{e}_z - \frac{m_x\mathbf{e}_x + m_y\mathbf{e}_y}{T_2}, \qquad [1.3]$$

where **m** is the magnetization which has Cartesian components m_x, m_y, and m_z, **B** is the magnetic induction, T_1 and T_2 are the phenomenologically introduced longitudinal and transverse relaxation times, respectively, m_o was defined before in Eq. [1.1], and $\mathbf{e}_x$, $\mathbf{e}_y$, and $\mathbf{e}_z$ are unit vectors in the x, y, and z directions. In Eq. [1.3], the z direction is assigned to be along the direction of the main external static magnetic field. If the relaxation terms in the Eq. [1.3] can be neglected, i.e., assuming infinitely long T_1 and T_2, then the Bloch equations become,

$$\frac{d\mathbf{m}}{dt} = \gamma(\mathbf{m}\times\mathbf{B}) \ . \qquad [1.4]$$

Recalling that the nuclear magnetic moment equals γ times the angular momentum $\mathbf{J} = \hbar\mathbf{I}$, $\mathbf{m} = \gamma\mathbf{J}$, and since the torque, $\prod$, exerted on a magnetic moment in a magnetic field equals $\prod = (\mathbf{m}\times\mathbf{B})$, Eq. [1.4] becomes

$$\frac{d\mathbf{J}}{dt} = (\mathbf{m}\times\mathbf{B}) = \prod . \qquad [1.5]$$

Equation [1.5] is simply a statement of the second law of Newton.

The reference frame used in Eqs. [1.3–1.5] is a static or laboratory frame of reference. Many properties of the Bloch equations are revealed more easily in a

rotating frame of reference. If we chose a reference frame such that it is identical to the laboratory frame, but rotating with an angular velocity Ω, then

$$\frac{d\mathbf{m}}{dt} = \frac{\delta \mathbf{m}}{\delta t} + \Omega \times \mathbf{m} \ , \qquad [1.6]$$

where $\frac{\delta \mathbf{m}}{\delta t}$ denotes the time rate of change of $\mathbf{m}$ with respect to the rotating frame. Equation [1.4] in the rotating frame becomes

$$\frac{\delta \mathbf{m}}{\delta t} = \mathbf{m} \times (\gamma \mathbf{B} - \Omega) \ . \qquad [1.7]$$

In the case of only a static field, $\mathbf{B} = B_o e_z$. Letting $\Omega = \gamma B_o e_z$, the right side of Eq. [1.7] is zero, i.e.,

$$\frac{\delta \mathbf{m}}{\delta t} = 0 \ . \qquad [1.8]$$

Equation [1.8] states that $\mathbf{m}$ does not change in the rotating frame which rotates with an angular velocity $\Omega = \gamma B_o e_z$. It also means that in the laboratory frame, $\mathbf{m}$ precesses around $\mathbf{B_o}$ with a frequency of $\omega_o = \gamma B_o$, where ω_o is called the Larmor frequency. Only at this frequency can an alternating magnetic field be in "resonance" (effectively exchanging energy) with the nuclear spin system.

In NMR experiments, the externally applied magnetic field ($\mathbf{B}$) is usually composed of two components: a static field ($\mathbf{B_o}$) along the longitudinal (z) direction, and a circularly polarized alternating (sinusoid) field called the radio-frequency (RF) or B_1 field in the transverse (xy) plane. In this case, one can choose $\Omega = \omega e_z$, where ω is the frequency of the B_1 field, so that Eq. [1.8] becomes

$$\frac{\delta \mathbf{m}}{\delta t} = \mathbf{m} \times [(\omega_o - \omega)\mathbf{e}_z + \gamma \mathbf{B}_1] = \gamma(\mathbf{m} \times \mathbf{B}_{eff}) , \qquad [1.9]$$

where $\mathbf{B}_{eff} = \frac{\omega_o - \omega}{\gamma}\mathbf{e}_z + \mathbf{B}_1$ is called the effective field in the rotating frame. At resonance, the so called offset frequency term, $(\omega_o - \omega)$, is zero and $\mathbf{B}_{eff} = \mathbf{B}_1$, and $\mathbf{m}$ precesses around $\mathbf{B}_1$ in the rotating frame with a frequency of γB_1. In modern NMR spectrometers, a pulsed RF field is usually used to manipulate the nuclear magnetization. If δt, the pulse width or time period during which the B_1 field is on, satisfies $\gamma B_1 \delta t = \pi/2$, then the pulse is called a 90° pulse. Likewise, if $\gamma B_1 \delta t = \pi$, the pulse is called a 180° pulse.

Next, we examine, in the rotating frame, the effects of longitudinal and transverse relaxation included in Eq. [1.3]. Because the RF field is only present during very short pulse periods, we examine the relaxation effects in the absence of RF fields. In the rotating frame at resonance, Eq. [1.3] becomes

$$\frac{\delta \mathbf{m}}{\delta t} = \frac{m_o - m_z}{T_1}\mathbf{e}_z - \frac{m_x \mathbf{e}_x + m_y \mathbf{e}_y}{T_2} . \qquad [1.10]$$

A steady state solution to Eq. [1.10] is $m_z = m_o$ and $m_x = m_y = 0$. If the initial longitudinal magnetization m(0) differs from m_o, then the longitudinal magnetization will approach m_o exponentially with a time constant of T_1, i.e.,

$$m_z(t) = m_z(0) + [\, m_o - m_z(0)] \, [\, 1 - e^{-t/T_1}] . \qquad [1.11]$$

Likewise, the transverse magnetization always decays exponentially with a time constant of T_2, i.e.,

$$m_{xy}(t) = m_{xy}(0)e^{-t/T_2} . \qquad [1.12]$$

The introduction of the relaxation terms T_1 and T_2 in the Bloch equations is purely phenomenological. The Bloch equations have been found to be a good model for many NMR studies involving liquid samples. In proton MRI, because a very large portion of the proton signal comes from the tissue water in the aqueous phase, the Bloch equations are also a very good approximation. The mechanisms for relaxation are in general beyond the scope of Bloch equations and requires quantum mechanics. Examples of relaxation mechanisms will be discussed in section 1.2.3. But first, we discuss the apparent transverse magnetization decay caused by the macroscopic magnetic field inhomogeneity that can be readily dealt with using the Bloch equations.

1.2.1.3 Free Induction Decay and Spin Echo

In a single-pulse NMR experiment, after the longitudinal magnetization is flipped into the transverse plane by a 90° excitation pulse, a signal known as the free induction decay (FID) can be observed. In the rotating frame, the recovery of m_z and dying out of m_{xy} are described by Eq. [1.11] and [1.12], respectively. When observed in the laboratory frame, the transverse magnetization, m_{xy}, whose direction does not change in the rotating frame, precesses around the z direction at the Larmor frequency ω_o. The motion of this magnetization then generates, according to Faraday's law, an electromotive force (EMF) in a receiver coil placed around the sample to pick up the induction signal. This FID is proportional to the magnitude of the transverse magnetization m_{xy} as well as to the Larmor frequency ω_o.

In an ideal homogeneous magnetic field B_o, the transverse magnetization decay follows Eq. [1.12]. But in practice the inhomogeneity of the B_o field is often large and causes the transverse magnetization to disappear faster. We denote the local magnetic field strength in the sample as $(B_o + \Delta B)$, where ΔB is the field inhomogeneity which is usually much smaller than B_o and depends upon location. The field inhomogeneity

makes spins at different locations of the sample precess at different frequencies. When observed in the rotating frame, taken to rotate at the average Larmor frequency, the transverse magnetization from the ensemble of isocromats of spins which initially points in one direction tends to disperse: the magnetization of some isocromats rotates faster and moves forward while that of others moves slower and backward because of the slight differences of their frequencies from the average one. The observed FID reflects the combined effect of this dispersing of the average magnetization and the true irreversible transverse relaxation (T_2). The time constant measured from an FID decay is called T_2^*. The true transverse relaxation time T_2 is governed by the molecular structure and dynamics of the sample, but T_2^* additionally contains a line width broadening contribution from the field inhomogeneities. Classically, one often regards T_2^* as the sum of two factors (22, 25),

$$1/T_2^* = 1/T_2 + \gamma \Delta B_{os} \,, \qquad [1.13]$$

where ΔB_{os} is the spread of field variation across the sample of interest.

The transverse decay due to static magnetic field inhomogeneities can (subject to certain constrains on the diffusion of water) be recovered by spin echo pulse sequences (26-28) to allow measurement of the true T_2. Figure 1.1 illustrates a spin echo sequence and the formation of a spin echo. The formation of the spin echo results because the refocusing pulse reverses the phase of the magnetization of each spin isocromat. The phase in Figure 1.1 can be visualized as the angle between the magnetization of an isocromat and the y-axis. The phase reversal makes the phase that continually accumulates in the second half of the echo time (TE) period exactly cancel the phase accumulated in the first half period, so that the dispersion of the magnetization is reversed. In this sense, the transverse decay that is caused by the field inhomogeneities is reversible. The decay of the magnitude of the echo over the echo

time TE is caused by irreversible mechanisms and provides a measure of the true T_2 relaxation time. If, instead of a single $(180°)_y$ pulse, a series of $(180°)_y$ pulses is placed in Figure 1.1 at intervals of TE, then a train of spin echoes will be formed at each TE interval. Such a pulse sequence is called a Carr-Purcell-Meiboom-Gill (CPMG) (28) sequence and is frequently used in the measurement of T_2 to overcome some of the constraints such as that on diffusion.

1.2.2 Basics of Magnetic Resonance Imaging

1.2.2.1 Spatial Encoding

Magnetic resonance imaging is a relatively new branch of NMR (29). As a tomographic imaging protocol, MRI is able to reveal visually the structural heterogeneity of a subject, often a part of a human body. Because water is the most abundant molecule in the body and because the proton has ideal spin properties (i.e., I=1/2 and the largest γ) for NMR study, water proton imaging is the natural choice and so far has dominated clinical MRI.

A unique technical aspect of MRI, compared to conventional spectroscopic NMR, is the requirement for spatial encoding. Spatial magnetic field gradients are commonly used in MRI to provide spatial encoding. The gradient field is superimposed on the main static field along the z direction. However, the direction of the gradient can be in any direction in space. When a linear gradient is applied to a sample, the Larmor frequency of the spins becomes a simple linear function of the spin location in space. This is the basic principle of the spatial encoding. Imaging sequence designing has become an art in the application of this principle. Among many different families of proton imaging techniques, spin warp Fourier transform (FT) imaging (30) is by far the most popular one.

In FT imaging, three methods of spatial encoding are used jointly to produce tomographic images of thin slices. The three methods include slice-selective excitation, frequency encoding, and phase encoding. Spins in a thin section or slice of the sample can be selectively excited without disturbing spins outside of the section by the use of a frequency-selective excitation RF pulse in the presence of a strong linear gradient field. The frequency-selective pulse, or soft RF pulse, is amplitude-modulated and sometimes also frequency-modulated so that its frequency spectrum has the shape of a narrow rectangular band. Because of the presence of a linear field gradient, only the spins in a thin section are excited. That section is perpendicular to the gradient direction and has proton Larmor frequencies that fall in the narrow frequency band of the selective RF pulse. Frequency encoding requires a linear gradient to be on during the acquisition of an FID or an echo signal. Along the gradient direction, the Larmor frequency of the spins is a linear function of the spatial location. Therefore the spatial distribution of the proton spins along this direction can be obtained following Fourier transform. Phase is used to encode the spatial information along the third direction. The phase encoding gradient pulse, whose amplitude is increased in small steps sequentially, is applied in the third direction before the echo formation so that the sequential phase shift contains the spatial information which can be extracted by Fourier transform. Two dimensional Fourier transformation is the most popular and convenient reconstruction method for two dimensional FT imaging.

1.2.2.2 MRI Contrast

Image contrast is another fundamental issue that must be understood in MRI. Image contrast is the variation of signal intensity between different types of tissue. The nuclear magnetic resonance signal depends inherently on the tissue parameters as well as on the parameters of the imaging sequence; so does the image contrast. There are

three major tissue parameters that determine signal intensity in an image. They are the proton spin density and the two relaxation times, T_1, and T_2. Spin density corresponds to N in Eq. [1.2], which determines the maximum signal available. T_1 and T_2 determine the actual signal that is observed using a given pulse sequence according to Eq. [1.11] and Eq. [1.12]. In the following, we will use the most common spin echo pulse sequence as an example to show how the tissue parameters and imaging parameters can affect the signal intensity and image contrast.

In the spin echo imaging sequence, a 90° slice selection pulse initially flips the longitudinal magnetization into the transverse plane at time zero, and a 180° refocusing pulse creates a spin echo at time TE. Spatial encoding gradient pulses are incorporated into the sequence. The sequence is repeated at time interval of TR (repetition time) with stepwise increases of the phase encoding gradient to acquire a complete raw data set. The number of phase encoding steps is determined by the desired spatial resolution, and is typically 128 or 256 as a compromise between spatial resolution and total imaging time. Once the spatial resolution is chosen, the voxel size and tissue spin density determine the total spin number, N, and therefore the maximum possible magnetization m_o in each of the voxels. The repetition time TR and relaxation time T_1 determine how much longitudinal magnetization is recovered and thus available for the repeated excitation. In Eq. [1.11], $m_z(0)$ is zero after the 90° excitation. For spin-echo sequences in which TR >> TE, the longitudinal magnetization at time TR is

$$m_z(TR) = m_o[\, 1 - e^{-TR/T_1}] \,. \qquad [1.14]$$

This $m_z(TR)$ is then flipped by the next 90° pulse to become $m_{xy}(0)$ in Eq. [1.12]. At t = TE, the measured magnetization is

$$m_{xy}(TE) = m_o[\, 1 - e^{-TR/T_1}]\, e^{-TE/T_2} \,. \qquad [1.15]$$

Equation [1.15] shows how the spin-echo signal in a given voxel depends upon m_o, T_1, T_2, TR, and TE.

The inherent variation of the three MRI parameters among different types of brain tissue (grey matter, white matter, cerebrospinal fluid, etc.) are in the range of 30% for the proton spin density, and more than 100% for both T_1 and T_2 (31). Not only does proton relaxation provide large inherent variation among brain tissues, but also relaxation contrast can be enhanced or suppressed by the choice of the two timing parameters, TR and TE, in the spin-echo sequence. For example, if $TE << T_2$ and $TR >> T_1$, the image contrast is primarily dependent upon the proton density of the tissue. If a very short TE is chosen, the T_2 contrast is suppressed and the degree of T_1 weighting can be manipulated by varying TR. Similarly, if a TR is chosen to be much longer than T_1, the T_1 contrast is suppressed and T_2 weighting can be varied by TE selection. In the latter case, Eq. [1.15] becomes

$$m_{xy}(TE) = m_o e^{-TE/T_2}. \qquad [1.16]$$

It requires a minimum of two measurements of m_{xy} using different TEs to give an estimation of the T_2 value. Equation [1.16] is the simple principle of T_2 imaging. In a gradient recalled imaging sequence, T_2^* replaces T_2 in Eq. [1.16]. T_2^*-weighted images are more sensitive to the line broadening produced by the static magnetic field inhomogeneity.

1.2.3 Water Proton Dipole-Dipole Relaxation (21-22)

So far we have treated T_1 and T_2 as parameters associated with a given sample. In this subsection we will explain the fundamentals of water proton relaxation using quantum mechanics to treat the nuclear magnetism. We will also examine the dipole-dipole relaxation mechanism in a two proton system and will discuss the importance of

molecular motion to NMR relaxation. Only the important concepts and some characteristics are addressed.

1.2.3.1 Longitudinal Relaxation

For a spin in a magnetic field, the Hamiltonian is $\mathcal{H} = -\hbar\gamma B_o \hat{I}_z$, where $\hat{I}_z$ is the z component of the spin operator. For a proton whose spin is 1/2, there are two eigenstates corresponding to I_z equals -1/2 and 1/2, and energy levels of $(\hbar\gamma B_o/2)$ and $(-\hbar\gamma B_o/2)$, respectively. The two states are customarily labeled β, for the high spin energy, and α for the low spin energy.

The longitudinal magnetization is proportional to the expectation value of $\hat{I}_z$. If N_α and N_β are the number of spins in the $|\alpha\rangle$ and the $|\beta\rangle$ states, respectively, the longitudinal magnetization is then proportion to

$$n = N_\alpha - N_\beta \, . \qquad [1.17]$$

Any change in N_α and N_β will cause a change in the spin energy of the system as well as a change in the magnetization. Such changes are possible when exchange of energy occurs between the spin system and some other system. In the case of longitudinal relaxation, the other system is referred to as the lattice, which is the thermal molecular kinetic system in dipole-dipole relaxation of water protons. The spins and lattice are said to be coupled when they can exchange energy between each other. There are two important consequences of this coupling.

The first consequence is that a change of the spin state must occur so that the spin system can absorb or emit energy. Let us denote $W_{\alpha\beta}$ as the probability of the spin transition rate from $|\alpha\rangle$ to $|\beta\rangle$ (absorbing energy) due to the coupling, and $W_{\beta\alpha}$ the reverse process. Then, we have a rate equation of

$$\frac{dN_\alpha}{dt} = N_\beta W_{\beta\alpha} - N_\alpha W_{\alpha\beta} , \qquad [1.18]$$

with a similar equation for $\frac{dN_\beta}{dt}$. Since in the steady state $\frac{dN_\alpha}{dt}$ is zero, $W_{\alpha\beta}$ and $W_{\beta\alpha}$ must satisfy the relationship

$$\frac{W_{\alpha\beta}}{W_{\beta\alpha}} = \frac{N_\beta^\circ}{N_\alpha^\circ} , \qquad [1.19]$$

where N_α° and N_β° are the spin numbers in the steady state.

The second consequence is that the two systems, the spins and lattice, reach their common state of thermal equilibrium corresponding to a common temperature, T. The ratio of the final equilibrium populations, N_α° and N_β°, is thus given by

$$\frac{N_\beta^\circ}{N_\alpha^\circ} = e^{-\Delta E/kT} = e^{-\gamma\hbar B_o/kT} . \qquad [1.20]$$

The temperature T at equilibrium is, by any practical means, just the temperature of the lattice because the lattice is like a reservoir of seemingly infinite thermal capacity relative to the small nuclear magnetization system. The nuclear magnetization energy is strikingly small relative to the molecular thermokinetic energy: $\Delta E = \gamma\hbar B_o = 1.05\times10^{-26}$ J for a proton at a magnetic field of 2.35 Tesla, while $kT = 4.14\times10^{-20}$ J at 27 °C. Because $\gamma\hbar B_o/kT << 1$, it is quite accurate to use the high temperature expansion (i.e., $e^{-\gamma\hbar B_o/kT} \cong 1 - \frac{\gamma\hbar B_o}{kT}$, and $\frac{1}{1-\gamma\hbar B_o/kT} \cong 1 + \frac{\gamma\hbar B_o}{kT}$).

From Eqs. [1.19] and Eq. [1.20] we obtain, using the high temperature expansion,

$$\frac{W_{\alpha\beta}}{W_{\beta\alpha}} = \frac{N_\beta^\circ}{N_\alpha^\circ} = e^{-\gamma\hbar B_o/kT} \cong 1 - \frac{\gamma\hbar B_o}{kT} . \qquad [1.21]$$

Clearly, $W_{\alpha\beta} \neq W_{\beta\alpha}$. The reason for the inequality of $W_{\alpha\beta}$ and $W_{\beta\alpha}$ is that in the lattice there are more low energy states available for energy absorption than high energy states for energy emission. If we define W as the mean of $W_{\alpha\beta}$ and $W_{\beta\alpha}$, then from Eq. [1.21] and the high temperature expansion we have

$$W_{\alpha\beta} = W\left(1 - \frac{\gamma\hbar B_o}{2kT}\right)$$

and

$$W_{\beta\alpha} = W\left(1 + \frac{\gamma\hbar B_o}{2kT}\right). \qquad [1.22]$$

From Eqs. [1.18] and Eq. [1.22] the rate of change in the number of net aligned spins, $\frac{dn}{dt}$, can be derived as

$$\frac{dn}{dt} = \frac{dN_\alpha}{dt} - \frac{dN_\beta}{dt}$$

$$= 2[N_\beta W_{\beta\alpha} - N_\alpha W_{\alpha\beta}]$$

$$= 2W\left[(N_\alpha + N_\beta)\frac{\gamma\hbar B_o}{2kT} - (N_\alpha - N_\beta)\right], \qquad [1.23]$$

where n is defined in Eq. [1.17] as $(N_\alpha - N_\beta)$, and obviously $(N_\alpha + N_\beta) = (N_\alpha^\circ + N_\beta^\circ)$. Using the high temperature expansion, one can show that the term $(N_\alpha + N_\beta)\frac{\gamma\hbar B_o}{2kT}$ is equivalent to the number of net aligned spins in the equilibrium state, n_o $[=(N_\alpha^\circ - N_b^\circ)]$. Thus, Eq. [1.23] can be re-written as

$$\frac{dn}{dt} = 2W\,(n_o - n)\,. \qquad [1.24]$$

Recalling that the longitudinal magnetization is proportional to the number of net aligned spins, Eq. [1.24] is therefore equivalent to

$$\frac{dm_z}{dt} = 2W\,[m_o - m_z(t)]\,. \qquad [1.25]$$

We have thus derived the longitudinal relaxation term in the Bloch equations [1.10] if we replace the term 2W such that

$$1/T_1 = 2W = W_{\alpha\beta} + W_{\beta\alpha} \, . \qquad [1.26]$$

Relaxation in general is a process in which the spin system approaches thermal equilibrium with the lattice. Longitudinal relaxation reflects a net change of spin orientation, therefore it must be accompanied by an exchange of energy between the spin system and the lattice. The final equilibrium state is determined solely by the temperature of the thermal reservoir (the lattice), but the rate at which the spin system approaches this state, i.e., $1/T_1$, is determined by how efficiently the spins exchange energy with the lattice.

1.2.3.2 Transverse Relaxation

Transverse relaxation results in loss of transverse magnetization. Transverse relaxation can occur through energy exchange with the lattice, as in longitudinal relaxation. It can also occur, however, without energy exchange with the lattice, but through loss of phase coherence.

Because the transverse spin operators do not commute with the Hamiltonian $\mathcal{H} = -\hbar\gamma B_o \hat{I}_z$, a transverse spin will be in a linear combination of the two eigenstates $|\alpha\rangle$ and $|\beta\rangle$. For example, a spin aligned in the x direction is in a state of $|x\rangle = \frac{1}{\sqrt{2}}(|\alpha\rangle + |\beta\rangle)$. It is easy to check that $\hat{I}_x |x\rangle = \frac{1}{2}|x\rangle$ using $\hat{I}_x = \frac{1}{2}(\hat{I}^+ + \hat{I}^-)$, where $\hat{I}^+$ and $\hat{I}^-$ are the raising and lowering spin operators, respectively, knowing the relationships $\hat{I}^+ |\alpha\rangle = |\beta\rangle$, $\hat{I}^+ |\beta\rangle = 0$, $\hat{I}^- |\alpha\rangle = 0$, and $\hat{I}^- |\beta\rangle = |\alpha\rangle$.

The $|x\rangle$ state can be reached in the whole system at t = 0 following a coherent 90° excitation pulse. At this time the spins are said to be in phase because they are all in the same state. At a later time, t > 0, neglecting the spin interactions, the wave function for the j^{th} spin is

$$|\Psi_j(t)\rangle = \frac{1}{\sqrt{2}}[e^{-iE_j t/\hbar}\,|\alpha\rangle + e^{+iE_j t/\hbar}\,|\beta\rangle]\,, \qquad [1.27]$$

where $-E_j$ and E_j are the energy levels of the $|\alpha\rangle$ and $|\beta\rangle$ states. The average spin in the x-direction is

$$\sum_j \langle I_x\rangle = \sum_j \langle \Psi_j(t)|\hat{I}_x|\Psi_j(t)\rangle\,. \qquad [1.28]$$

It is straight forward from Eq. [1.27] and [1.28] to obtain

$$\begin{aligned}\sum_j \langle I_x\rangle &= \frac{1}{2}\sum_j \cos\left(\frac{2E_j t}{\hbar}\right)\\ &= \frac{1}{2}\sum_j \cos\left(\gamma B_o t + \gamma \Delta B_j t\right)\\ &= \frac{1}{2}\sum_j \cos\left[\omega_o t + \Phi_j(t)\right]\,, \end{aligned} \qquad [1.29]$$

where we have replaced E_j with the nuclear magnetic energy $\gamma\hbar(B_o + \Delta B_j)$, assuming a local field inhomogeneity of ΔB_j, and have introduced a generalization of the phase term $\Phi_j(t)$ which depends on the local field inhomogeneity and changes with time. Again, we have found, using a quantum mechanical approach, that the average transverse spin oscillates at the Larmor frequency. The conclusion is not different from that we derived from the Bloch equations. In the presence of field inhomogeneity, the average transverse spin in Eq. [1.29] eventually disperses because of the increasing spread of the phase term in Eq. [1.29]. In other words, the spins are losing their phase

coherence. This decay of the transverse spin can result from field inhomogeneities and requires no exchange of energy in the spin system. Another type of loss of phase coherence without a net energy exchange happens in coupled and oppositely oriented spin pairs in which a mutual exchange of the spin orientations (flip-flop) is possible. The spin transitions caused by the spin coupling are incoherent in nature and lead to a random phase distribution in the transverse spins. It is obvious that any coupling between the spin system and lattice that causes transitions between states $|\alpha\rangle$and $|\beta\rangle$is accompanied by an energy exchange that induces transverse relaxation, since an $|x\rangle$ state is just made up of $|\alpha\rangle$and $|\beta\rangle$. All those types of transverse relaxation mechanisms are present in the proton dipole-dipole relaxation, so it is instructive to examine this relaxation mechanism. Quite a few interactions involving nuclear spins are capable of inducing nuclear spin relaxation. Those include direct dipole-dipole nuclear spin interactions, indirect nuclear spin interactions (scalar coupling), electron orbital and nuclear spin interactions, electron-nuclear spin interactions, and electrical field gradient and nuclear quadrupole interactions. In essence, any interaction that causes a fluctuating magnetic field at a nucleus is a possible source of relaxation. But for water protons, the proton dipole-dipole relaxation is usually the dominant mechanism in solutions as well as in most aqueous tissues.

1.2.3.3 Dipole-Dipole Relaxation in a Two Proton System

Classically, a magnetic moment $\boldsymbol{\mu}$ produces a local dipole magnetic field

$$\mathbf{B}_{loc} = \frac{\mu_o}{4\pi}\left[\frac{3(\boldsymbol{\mu}\bullet\mathbf{r})\bullet\mathbf{r}}{r^5} - \frac{\boldsymbol{\mu}}{r^3}\right], \qquad [1.30]$$

where $\mathbf{r}$ is the radius vector from $\boldsymbol{\mu}$ to the point of interest and μ_o is the permeability of free space. Between a pair of identical spins the interaction energy, $(-\boldsymbol{\mu}\bullet\mathbf{B}_{loc})$, is thus

$$E = \frac{\mu_o}{4\pi}\,\gamma^2\hbar^2\left[\frac{\mathbf{I}_1 \bullet \mathbf{I}_2}{r^3} - \frac{3(\mathbf{I}_1 \bullet \mathbf{r})(\mathbf{I}_2 \bullet \mathbf{r})}{r^5}\right], \qquad [1.31]$$

where $\mathbf{r}$ is the radius vector from spin "1" to spin "2". The interaction Hamiltonian $\mathcal{H}_d$ is easily obtained from Eq. [1.31] by simply taking $\mathbf{I}_1$ and $\mathbf{I}_2$ as spin operators. Such an $\mathcal{H}_d$ can be put in a new form by expressing the spin operator $\hat{I}$ in terms of $\hat{I}_z$, $\hat{I}^+$, and $\hat{I}^-$, by expressing the Cartesian coordinates in terms of spherical coordinates r, θ, and ϕ, and by regrouping the terms according to their spin operators, as

$$\mathcal{H}_d = \frac{\mu_o}{4\pi}\,\frac{\gamma^2\hbar^2}{r^3}\,(A + B + C + D + E + F), \qquad [1.32]$$

where

$$\begin{aligned}
A &= \hat{I}_{z1}\,\hat{I}_{z2}\,(1 - 3\cos^2\theta),\\
B &= \frac{1}{4}(\hat{I}_1^+\hat{I}_2^- + \hat{I}_1^-\hat{I}_2^+)\,(1 - 3\cos^2\theta),\\
C &= -\frac{3}{2}(\hat{I}_1^+\hat{I}_{z2} + \hat{I}_{z1}\hat{I}_2^+)\,\sin\theta\cos\theta\,e^{-i\phi},\\
D &= -\frac{3}{2}(\hat{I}_1^-\hat{I}_{z2} + \hat{I}_{z1}\hat{I}_2^-)\,\sin\theta\cos\theta\,e^{+i\phi},\\
E &= -\frac{3}{4}(\hat{I}_1^+ + \hat{I}_2^+)\,\sin^2\theta\,e^{-2i\phi},\\
F &= -\frac{3}{4}(\hat{I}_1^- + \hat{I}_2^-)\,\sin^2\theta\,e^{+2i\phi}.
\end{aligned} \qquad [1.33]$$

Clearly, the dipole-dipole interaction depends upon the relative position and orientation of the two spins. A rough estimation for the magnitude of the proton magnetic field is, according to Eq. [1.30], $\frac{\mu_o}{4\pi}\frac{\gamma\hbar I}{r^3}$, or about 3 Gauss for an r value of 1.6 Å which is typical of the interproton separation in a water molecule.

While the distance between the proton pair in a water molecule is nearly a constant, the relative angular coordinates, θ and ϕ, can take on random values. Accordingly, the mutual dipole magnetic field between such a pair can be in the range

of ±3 Gauss. In other word, the spread in the resonance frequency of the protons can be as large as 25 kHz. If the molecular motion of water molecules is restricted so that the relative coordinates (r, θ, ϕ) do not change over a time of $4x10^{-5}$ sec, i.e. the inverse of 25 kHz, the spread in resonance frequency will cause a total loss of phase coherence in the transverse magnetization. Internal molecular motion is characterized by a rotational diffusion correlation time, τ_c, which can be loosely defined as the time taken for the interproton vector to rotate one radian. Water molecules that are in ice or that are bound to the surface of macromolecules experience restricted molecular motions, and the correlation time τ_c of such water molecules may be on the order of 10^{-5} sec or greater (32). When τ_c exceeds 10^{-5} sec, the static local dipole fields cause the disappearance of transverse magnetization in a very short time period, resulting in very short T_2 values of 10^{-4} to 10^{-5} sec. And because significant molecular motion occurs in a period of 10^{-5} sec, spin-echo sequences are useless in refocusing the dephased magnetization. The signal from protons in a solid phase for which T_2 is as short as in ice is not detectable in MRI.

The reason for the longer T_2 values of the water proton in aqueous tissue is the faster molecular motion present in bulk water. Bulk water, also called free water, refers to water molecules in the liquid bulk phase in which molecular motion is determined solely by the characteristics of the water molecule and is not perturbed by the presence of macromolecules. The correlation time of bulk water at room temperature is on the order of 10^{-12} sec. In the presence of such fast molecular rotations, the dependence on θ and ϕ in Eq. [1.33] results in an $\mathcal{H}_d$ of zero when averaged over a time 10^{-5} sec, which is the time required for the local dipole field to dephase the transverse magnetization in the absence of molecular motion. The consequence of this is the disappearing of the static line broadening and the resurgence of a much narrower water peak. The phenomenon is called motional narrowing. The criterion for motional narrowing is (21)

$$\langle \Delta\omega^2 \rangle^{1/2} \tau_c << 1 , \qquad [1.34]$$

where $\langle \Delta\omega^2 \rangle$ is the second moment of the line shape of non-moving spin pairs and is on the order of $(\gamma B_{loc})^2$.

Under the condition of motional narrowing, the dipole-dipole interaction described by $\mathcal{H}_d$ in Eq. [1.32] disappears completely in the first order approximation. The relaxation effect thus should be considered in the second order approximation of the perturbation of $\mathcal{H}_d$ on the undisturbed spin system and the lattice. In doing so, $\mathcal{H}_d$ is rewritten in the form

$$\mathcal{H}_d = \sum_q F^{(q)} G^{(q)} , \qquad [1.35]$$

where the $G^{(q)}$ terms contain only spin operators and are reordered from the expansion of Eq. [1.32] and Eq. [1.33] according to the order of the spin operators, and the $F^{(q)}$ terms contain only the lattice parameters (i.e., r, θ, and ϕ). The $G^{(q)}$ terms determine whether a pair of undisturbed spin eigenstates are joined together by $\mathcal{H}_d$, thereby a transition between them being possible. The $F^{(q)}$ terms determine the rate probability of these transitions at a certain temperature.

The undisturbed spin system under the Hamiltonian $\mathcal{H}_o = -\hbar\gamma B_o (\hat{I}_{z1} + \hat{I}_{z2})$ has four combinations of spin orientations corresponding to three energy levels. These include $|\beta\beta\rangle$, $|\beta\alpha\rangle$, $|\alpha\beta\rangle$, and $|\alpha\alpha\rangle$. The term A in Eq. [1.32] contains the spin operators $\hat{I}_{z1}$ and $\hat{I}_{z2}$ which join only like states, so it represents only static interactions. The term B of Eq. [1.32] contains the spin operators $(\hat{I}_1^+ \hat{I}_2^- + \hat{I}_1^- \hat{I}_2^+)$ which join $|\alpha\beta\rangle$ and $|\beta\alpha\rangle$ states together, so it permits the proton pair to exchange their spin orientations via the so-called flip-flop interactions. Both A and B terms do not permit transitions that lead to a net exchange of spin orientation, so they do not contribute to longitudinal relaxation. The A and B terms together are called the secular term of $\mathcal{H}_d$. The spin

operators in the C and D terms join two degenerate states, $|\alpha\beta\rangle$ and $|\beta\alpha\rangle$, with both $|\beta\beta\rangle$and $|\alpha\alpha\rangle$ states, to permit transitions that lead to a change of spin orientation accompanied by an energy exchange of $\hbar\omega_o$ with the lattice. Similarly, the spin operators in the E and F terms join $|\beta\beta\rangle$with $|\alpha\alpha\rangle$, to permit transitions that lead to a change of the spin orientation accompanied by an energy exchange of $2\hbar\omega_o$ with the lattice. The terms C, D, E, and F contribute to both longitudinal and transverse relaxation. To find the relaxation efficiencies of those spin transitions, one needs to employ the perturbation formulation of quantum mechanics using $\mathcal{H}_d$ as the perturbation. The final expressions for the longitudinal and transverse relaxation rate in the two proton system are (21, 33),

$$R_1 = \frac{1}{T_1} = \frac{9\gamma^4\hbar^2}{8}\left(\frac{\mu_o}{4\pi}\right)^2\left[J_1(\omega_o) + J_2(2\omega_o)\right],$$

$$R_2 = \frac{1}{T_2} = \frac{9\gamma^4\hbar^2}{32}\left(\frac{\mu_o}{4\pi}\right)^2\left[J_0(0) + 10J_1(\omega_o) + J_2(2\omega_o)\right], \qquad [1.36]$$

where J_0, J_1, and J_2 are the spectral density functions which are defined as Fourier transforms of the auto correlation functions of the three spatial parts, i.e., $(1 - 3\cos^2\theta)/r^3$, $(\sin\theta\cos\theta\, e^{-i\phi})/r^3$, and $(\sin^2\theta\, e^{2i\phi})/r^3$, in Eq. [1.32]. Because the variables in the $F^{(q)}$ terms, r, θ, and ϕ, are random functions of time, the magnetic dipole field, or more correctly the magnetic interaction between each of the spin pairs, fluctuates due to fluctuations of the spatial coordinates. The spectral densities in Eq. [1.36] can be interpreted as representative of the energy of the fluctuating magnetic field at the given frequencies (21). Therefore, $J_1(\omega_o)$ and $J_2(2\omega_o)$ represent the energy densities of the microscopic fluctuating magnetic field at the proton resonance frequency, ω_o, and at $2\omega_o$. Recalling that an energy exchange of $\hbar\omega_o$ is required in the transitions permitted by the C and D spin terms, and that an energy exchange of $2\hbar\omega_o$

is required by the E and F terms, the appearance of $J_1(\omega_o)$ and $J_2(2\omega_o)$ in the two equations of [1.36] is not surprising. They simply indicate that, in order to facilitate proton spin relaxation, molecular motion must provide magnetic field fluctuation at the correct proton resonance frequencies. Similarly, $J_0(0)$ represents the density of static energy and corresponds to the transition that is not accompanied by energy exchange between the spins and the lattice. Only transverse relaxation is affected by $J_0(0)$.

For the intra-molecular water proton pairs, the inter-proton distance, r, does not change significantly and relaxation is facilitated mainly by the rotational motion of a water molecule. The spectral density functions have dispersive Lorentzian forms, and Eq. [1.36] becomes

$$R_1 = \frac{1}{T_1} = \frac{6}{20}\frac{\gamma^4\hbar^2}{r^6}\left(\frac{\mu_o}{4\pi}\right)^2\left[\frac{\tau_c}{1+\omega_o^2\tau_c^2} + \frac{4\tau_c}{1+4\omega_o^2\tau_c^2}\right],$$

$$R_2 = \frac{1}{T_2} = \frac{3}{20}\frac{\gamma^4\hbar^2}{r^6}\left(\frac{\mu_o}{4\pi}\right)^2\left[3\tau_c + \frac{5\tau_c}{1+\omega_o^2\tau_c^2} + \frac{2\tau_c}{1+4\omega_o^2\tau_c^2}\right], \quad [1.37]$$

where τ_c is the correlation time as introduced previously. Equations [1.37] are the fundamental equations in determining water proton relaxation rates. They are developed from the BPP relaxation theory (named after Bloembergen, Purcell, and Pound) (32-33). The equations indicate that the correlation time τ_c and the Larmor frequency ω_o are the two parameters that determine the relaxation rates.

In the situation of very fast molecular motion where $\omega_o\tau_c << 1$, which happens in the non viscous liquids such as water, $\frac{1}{T_1} = \frac{1}{T_2} \cong \frac{3}{2}\left(\frac{\mu_o}{4\pi}\right)^2\left(\frac{\gamma^4\hbar^2}{r^6}\right)\tau_c$. This is true under common imaging field strengths where proton resonance frequency ranges from 1 to 100 MHz (ω_o: 10^6 - 10^9 s^{-1}), while τ_c in pure water is around 10^{-12} sec.

Taking r as 1.6 Å and τ_c as $5x10^{-12}$ sec for water molecules, we estimate $T_1 = T_2 \equiv 4$ sec. Under these fast motion conditions, relaxation rates are not affected by the field strength, B_o.

In the situation of very slow molecular motions where $\omega_o\tau_c >> 1$, T_1 and T_2 are very different: $\frac{1}{T_1} \propto \frac{1}{\omega_o^2 \tau_c}$ and $\frac{1}{T_2} \propto \tau_c$. T_1 becomes longer as τ_c and ω_o increase, while T_2 becomes shorter as τ_c increases and does not depend upon ω_o. The extreme case of this is when the molecules are frozen in a solid sample and motional narrowing no longer holds. An intermediate situation, where $\omega_o\tau_c \approx 1$, exists in viscous liquids. T_1 becomes frequency dependent and reaches a maximum at $\omega_o\tau_c \approx 0.6$. Because the frequency independent secular term begins to dominate the transverse relaxation in this situation, T_2 is always shorter than T_1 and is much less dependent on the resonance frequency.

The equations in [1.37] take account only of relaxation contribution from the rotational motion of the paired protons of fixed interproton distance, corresponding to the dipole-dipole relaxation in water. The intermolecular proton dipole-dipole interaction also contributes to the relaxation because of translational molecular motion in which the interproton distance is a random function of time. The intermolecular and intramolecular dipole-dipole relaxation contributions are in proportion and the intramolecular one dominates (21)

1.2.4 Proton Relaxation in Protein Solutions and in Tissue (32)

Water proton relaxation in tissue is much more complicated than in single phase liquid water. The complication is brought about by the presence of macromolecular solutes in the cytosol which may interact with the water molecules both magnetically

and non-magnetically, by the existence of multiple phases of water, by the structural heterogeneity of the tissue, and by the possible presence of paramagnetic species. Although a great deal of knowledge has been accumulated concerning water proton relaxation in tissue, a unified, precise understanding of all the relaxation mechanisms has not yet been achieved due to the complexity and diversity of body tissues. In this subsection we focus on an explanation, using protein solutions as a model, of how a macromolecular solute can greatly affect water proton relaxation.

The solvent water in protein solutions exists in at least two distinct phases, namely the bulk phase and the hydrated phase. In the bulk phase, as mentioned previously in section 1.2.3.3, the molecular motion of water is not affected by the solute and is determined solely by the characteristics of the water molecule. In the hydrated phase, however, the molecular motion of water is perturbed from that of bulk water by either forming hydrogen bonds with a macromolecule or simply being very close to the surface of it. The relaxation characteristics of bulk water are the same as the single phase liquid water (extreme motional narrowing, $\omega_o\tau_c << 1$), but these are different for hydrated water because of a longer correlation time τ_c, anisotropic rotation, and the possible cross relaxation associated with hydrated water.

Hydrated water experiences slower molecular motion than bulk water. For hydrated water which forms double hydrogen bonds with a protein molecule, the correlation time, τ_c, is on the order of 10^{-9} sec (32). From our earlier discussion of Eq. [1.37], it is clear that this longer correlation time enables hydrated water to relax faster than its bulk water counterpart. Because $(\omega_o\tau_c)$ is closer to unity, T_2 is shorter than T_1 in hydrated water.

Hydrated water may experience anisotropic rotation when strongly bonded to macromolecules (32). Anisotropic rotation of water molecules could lead to a non-zero

value of the $(1 - 3\cos^2\theta)$ term that appears in the secular terms of the dipole-dipole interaction between the intramolecular proton pair when averaged over time. The residual static interaction, which is absent in bulk water, causes significant line broadening and very short T_2, as happens in solid samples. As a result, the difference between the values of T_1 and T_2 becomes even larger.

Hydrated water is also in a position to experience intermolecular cross-relaxation with the protein protons. Between the protons at the periphery of the protein molecules and the protons of the tightly bonded hydrated water, transfer of spin energy is possible by the way of mutual spin flips. The macromolecular protons act as relaxation sinks in the solution and hydrated water can then relax very fast.

As discussed above, a change in hydrodynamics (slower molecular motion and anisotropic rotation) and cross-relaxation with protein protons make hydrated water relax faster than bulk water. Values of T_1 and T_2 are different in hydration water and shorter than those in bulk water. But because of the rapid exchange of water molecules between the two phases, water proton relaxation rates in protein solutions are the weighted averages,

$$R_1 = p_a R_{1a} + p_b R_{1b},$$
$$R_2 = p_a R_{2a} + p_b R_{2b}, \qquad [1.38]$$

where we have used "a" to denote the hydrated phase and "b" the bulk phase, and where p_a and p_b are the fractional populations of hydrated water and bulk water in the solution. Because $p_a + p_b = 1$, Eqs. [1.38] can be rewritten as

$$R_1 = R_{1b} + p_a(R_{1b} - R_{1a})$$

and

$$R_2 = R_{2b} + p_a(R_{2b} - R_{2a}). \qquad [1.38]$$

Obviously, p_a is determined by the total available hydrophilic surface area of the protein molecules in the solution, so in solutions of the same protein, the water proton relaxation rates are linearly proportional to the protein concentration. Extending this conclusion to tissue, we can say that the greater the water content of tissue, the less efficient is the relaxation of the water protons and the longer are T_1 and T_2. But this generalization is only qualitatively true in tissue because different types of tissue may have different protein components, lipid components, and paramagnetic species.

In the soft tissues of the body, cellular and subcellular structures create microscopic heterogeneous compartments. Water proton relaxation in each of these microscopic compartments is determined by the local protein content and local water molecular dynamics and is expected to vary considerably among the different compartments. But because of the fast exchange of water molecules between the microscopic compartments thanks to diffusion, the observed water proton relaxation rate in such tissue samples is usually just the population averaged value. In other words, in spite of the great heterogeneity of tissue at the microscopic level, it is often the average behavior of water protons in the soft tissue that is observable in NMR relaxation measurements.

1.2.5 Water Proton Relaxation Enhancement by Paramagnetic Species

Paramagnetic species enhance water proton relaxation rates because they possess electrons with unpaired spins. For most molecules, electrons are paired in their inner shells and in covalent bonding orbitals and the electron spins cancel one another. Substances with no net electron spin are referred to as diamagnetic. Water and most other molecules in the body are diamagnetic. Electrons in diamagnetic substances show no magnetic moments and are incapable of stimulating proton relaxation.

Some elements, e.g., transition elements, however, have one or more orbitals that are unfilled and may thus contain unpaired electrons. The electrons in unfilled shells couple according to one of several rules (34) but give rise to a non-zero net electronic spin. Similar to a nuclear spin, a net electronic spin also has associated with it a magnetic moment. The magnetic moment associated with a single electron spin is approximately 600 times greater than that of the proton. Substances containing atoms that possess a net unpaired electronic spin are referred to as paramagnetic. In the absence of an external magnetic field, no net magnetization of the sample is observable even though the individual paramagnetic molecules or ions possess magnetic moments. This is because the individual magnetic moments, independent of one another, orient randomly and produce no net magnetization. In the presence of an external magnetic field, however, the individual magnetic moments align preferably to the external field according to the laws of statistical quantum mechanics. The resulting net magnetization is proportional to the external magnetic field strength, to the concentration, and to the molar magnetic susceptibility of the paramagnetic substance. The molar susceptibility of a paramagnetic material is proportional to the square of the molecular magnetic moment and is inversely proportional to the absolute temperature (Curie's law). The molar susceptibility of paramagnetic substances is generally about five orders greater than that of diamagnetic substances and is different in the sign. Therefore, even if only a small amount of paramagnetic substance is present in tissue, it can greatly alter the local magnetic susceptibility.

A number of transition metal ions, which have unpaired spins in their 3d orbital (iron group) or in their 4f orbital (rare earths), are important paramagnetic materials and often used in MR studies. For the purpose of increasing MR image contrast, pharmaceutical compounds that contain paramagnetic metal ions have been developed as contrast agents, which upon administration enhance tissue relaxation and hence

change image contrast (5). The most widely used contrast agent in diagnostic imaging is gadolinium-diethylenetriaminepentaacetic acid (GdDTPA), an organic chelate of Gd^{3+}. The ion is chelated to modify its toxicity and other physiological properties. Of the two lanthanide metal ions, Gd^{3+} and dysprosium (Dy^{3+}), the magnetic moment of Dy^{3+} is slightly larger than that of Gd^{3+}, but the electron spin relaxation time of Dy^{3+} is about three to four orders shorter than that of Gd^{3+} (5). As a result, Dy^{3+} is much less effective for directly inducing proton relaxation than Gd^{3+} (5). In practice, Dy^{3+} is better than Gd^{3+} for creating susceptibility contrast, while Gd^{3+} is better for creating direct relaxation contrast. DyDTPA is employed in our model phantoms described in Chapters 2 and 4.

In the human body, the transition metal iron accumulates naturally in the tissue of several vital organs, including the brain (35), the liver (3), and the vascular blood pools, at concentrations large enough to enhance the water proton relaxation significantly. Other paramagnetic metals, which although naturally present in the brain tissue, are present at very low concentrations, and are therefore less important to relaxation enhancement in that tissue.

The mechanism of water proton relaxation enhancement can arise directly from the hyperfine interactions. The strong, fluctuating magnetic fields generated by the individual paramagnetic ions stimulate proton relaxation of the nearby water protons in a manner similar to that of the proton-proton spin dipole interaction. In addition, for those elements that have a finite probability of approaching a nuclear site, there are also Fermi contact contributions. However, relaxation enhancement can also arise from a susceptibility-difference effect. If the paramagnetic ions are compartmentalized they can collectively create a localized heterogeneity in susceptibility, which in turn produces strong field inhomogeneities in the presence of an external magnetic field.

These local inhomogeneities will not only broaden the proton resonance line width but also increase the rate of loss of proton phase coherence. The two types of enhancement, one due to the hyperfine interactions and the other to susceptibility-difference effects, will be discussed separately.

The hyperfine interaction mechanisms were studied in solutions in the early years of NMR development and a theoretical explanation provided by the work of Solomon (8) and Bloembergen (9). The hyperfine interactions are effective in enhancing the solvent water proton relaxation only when water molecules are able to move quite close to the paramagnetic ions. This is because the dipolar terms varies as $1/r^6$ and the contact term requires overlap of the electron wave with the nuclear wave. This happens when subsequent exchange of one or more water molecules bound in the primary coordination sphere of the metal ion with the bulk water molecules spreads the effect of the paramagnetic ion. The relaxivity of a given paramagnetic metal ion decreases dramatically as the number of coordinated water molecules is reduced due to chelation (36). In tissue, the naturally accumulated iron tends to be bound in macromolecules such as hemoglobin, ferritin and hemosiderin, and is not generally accessible to the tissue water. Thus the hyperfine interaction is unlikely to contribute to the solvent water proton relaxation for most of the tissue iron.

Compartmentalized paramagnetic materials can enhance water proton relaxation through susceptibility-difference effects. The relaxation enhancement is brought about by water diffusion through the local field inhomogeneities created by the heterogeneity in magnetic susceptibility. The effect which self-diffusion of liquid molecules through an inhomogeneous field has on the amplitude of an echo was discovered in the early years of NMR by Hahn (26). In the simplified case where the field inhomogeneity can be described by a linear field gradient, G, and the self-diffusion is unrestricted,

incoherently random, and characterizable by a single diffusion coefficient, D, the transverse relaxation decay in a single-echo spin echo experiment can be described by (26, 37)

$$m_{xy}(TE) = m_{xy}(0) \exp[-TE/T_2 - \gamma^2 D G^2 TE^3/12] , \qquad [1.39]$$

showing an enhancement to the transverse decay rate due to the term $\gamma^2 D G^2 TE^3/12$. In tissue containing microscopically-compartmentalized paramagnetic substances, the local field inhomogeneities are globally unlike linear field gradients so that Eq. [1.39] is not an entirely valid description in this case. It is very difficult in the microscopically structured tissue to model accurately the tissue compartmentation, the field inhomogeneities, and the partially restricted water diffusion paths. So it is seemingly impossible to compute accurately the relaxation enhancement in a real tissue sample. Many studies have focused on water proton relaxation properties in simpler heterogeneous systems such as water suspensions of small, water impermeable, magnetic spheres or cylinders (11-12, 38-41). In the study of such model systems, three regimes have been introduced to distinguish the relaxation enhancement (12, 42). The three regimes are defined in terms of the diffusive correlation time of the water molecules, τ_D, in the presence of the magnetic inhomogeneity and the characteristic variation of the field perturbation in units of the proton Larmor frequency, $\Delta\omega$. The three are named (12) the motionally averaged (when $\Delta\omega \cdot \tau_D << 1$), the intermediate ($\Delta\omega \cdot \tau_D \approx 1$), and the static ($\Delta\omega \cdot \tau_D >> 1$) regimes. In the case of a suspension of magnetic spheres of radius λ, $\Delta\omega$ is the equatorial value of the dipole magnetic field at the surface of a sphere (for the reference of dipole field see Eq. [2.2] in Chapter 2), and τ_D is the time required to diffuse a distance of the order of λ, i.e., $\tau_D = \lambda^2/D$, where D is as previously defined, the water diffusion coefficient constant (12, 38).

In the motionally averaged regime, the "diffusion rate", $1/\tau_D$, is much greater than $\Delta\omega$. As a result, the diffusing water molecules in the outer layer of a sphere can quickly and thoroughly sample the dipole field of that magnetic sphere before the effective loss of transverse magnetization occurs. The relaxation rate induced by the spherical magnetic impurity is (38, 43)

$$R_2^* = R_2 = \frac{16}{45} P_{vs}(\Delta\omega)^2\tau_D, \quad \Delta\omega\cdot\tau_D << 1, \qquad [1.40]$$

where P_{vs} is the volume fraction of the water impermeable magnetic spheres in the solution. In this regime, enhancement of R_2 and R_2^* (= $1/T_2^*$) are the same, and both vary quadratically with $\Delta\omega$ and inversely with D.

In the static regime, where $1/\tau_D$ is much smaller than $\Delta\omega$, the transverse relaxation in a spin-echo experiment is described by (12, 39)

$$R_2 = (\gamma\sigma_G TE)^2 D/12, \qquad \Delta\omega\cdot\tau_D >> 1, \qquad [1.41]$$

where σ_G denotes the variance of the internal gradient distribution induced by the perturbation and TE is, as defined before, the spin echo time. The relaxation enhancement increases linearly with the diffusion coefficient and quadratically with the magnetization of the sphere. The transverse relaxation rate is also affected by the value of TE. R_2^* in the static regime is expected to follow Eq. [1.13], with a static contribution $\gamma\Delta B_{os}$ from the susceptibility-difference effect, where ΔB_{os} in this particular case can be regarded as the variance of the internal field inhomogeneity distribution induced by the perturbations (39).

The intermediate regime falls in between the motionally averaged and the static regimes, with $\Delta\omega\cdot\tau_D \approx 1$. The field distribution (reflected in $\Delta\omega$) is the source of dephasing of the proton magnetization, while water diffusion (τ_D) tends to average out the field inhomogeneities felt by the proton spins. The counterbalance of the two

influences in this regime makes the enhancement of R_2 very efficient and echo time dependent. Moreover, because of the significant diffusion in this regime, the enhancement of R_2^* is expected to be less than the static maximum $\gamma\Delta B_\infty$ which appears in Eq. [1.13] (12). In this regime neither the enhancement of R_2 nor R_2^* follows the quadratic relationship with field strength which is predicted by Eq. [1.40] and Eq. [1.41] for the other regimes (12). The complication of the relaxation enhancement in the intermediate regime can be thought to arise from a diffusion which is neither fast enough to allow water molecules to sample the full static field inhomogeneities (in a time period of the order of $1/\Delta\omega$), nor slow enough to allow water molecules to remain in a small enough volume for the field disturbance to be approximated by a linear gradient. As a result, the phase accumulation in this regime does not display Gaussian statistics (42), and so far there has been no analytical formula like Eq. [1.40] or Eq. [1.41] produced to describe the relaxation enhancement. An effective way to study this regime has been provided by computer simulation with Monto Carlo diffusion models (11-12, 40-41). A limitation of a simulation study is that explicit parameter values must be assigned in the simulation program, therefore one must be very cautious in the generalization of any conclusions obtained from simulation experiences. It normally requires the development of a specific simulation model to obtain numerical data for a particular experimental setting. The development of the simulation program in this study started in late 1991 and was aimed at understanding the relaxation behavior in the paramagnetic suspensions of red blood cells (Chapter 2).

1.3 Brain Iron and Its Effects on MRI Relaxation

1.3.1 Brain Iron

Iron is one of the metal ions essential to the biological functioning of the human brain (44). From a chemical point of view, iron in the brain can be divided into two

groups: heme compounds and non-heme compounds. Hemoglobin is normally present in the red blood cells of the vascular bed, however the heme iron in the hemoglobin may be only loosely regarded as brain iron since microscopically the blood-brain barrier effectively separates the true brain tissue from the vascular blood pool. Under the pathological conditions of hemorrhage, blood enters into the brain and forms hematomas. The hemoglobin released as a result of hemolysis is then taken up by the glial cells, and the heme iron converted within weeks to ferritin and hemosiderin (45). Some protein enzymes in the brain also contain heme iron, of which the cytocromes in the mitochondrial electron transfer chain are of primary biological importance. However, if the hemoglobin in the blood is not taken into account then heme iron constitutes only a small fraction of the total brain iron (46).

The non-heme compounds belong to a more heterogeneous group which may contain ferritin and hemosiderin iron, iron in various non-heme enzymes, and probably small amounts of inorganic iron that is loosely attached to lipids (46) and other small substances (47) in the cells. The non-heme brain iron can be found (35) in many types of prepared cell fractions that include the nuclear fraction, mitochondrial fraction, microsomal fraction, and a soluble fraction. About one-third of the non-heme iron consists of ferritin iron (35), making ferritin the major form of brain iron.

The distribution of brain iron is far from homogeneous and exhibits a remarkable variation in regional concentrations and in specific cellular localization (1, 35, 48-50). The most abundant brain iron is in some gray matter nuclei which belong to the so-called extrapyramidal system and include the globus pallidus, red nucleus, substantia nigra, putamen, dentate nucleus, and caudate nucleus. The cortex and white matter tracts of the brain contain less iron. The average concentration of non-heme iron in the adult human brain is reported to be 21 mg per 100 g wet tissue in the globus

pallidus, 18.5 mg per 100 g wet tissue in the substantia nigra, 13 mg per 100 g wet tissue in the putamen, 4.8 mg per 100 g wet tissue in the thalamus, and 4.2 mg per 100 g wet tissue in the frontal white matter (35). Functionally, iron is required in oxidative metabolism at every step of the electron transport chain. However, no known single role explains its geometric distribution or the large concentrations which are seemingly in excess of the tissue requirements in the iron-rich extrapyramidal nuclei. The cellular localization of brain iron is not completely understood either. Using Perl's stain (sensitive to the ferric iron) on microscopic sections of brain to determine the cellular distribution of iron, iron deposition is found to occur predominantly in oligodendrocytes, but fine granular iron deposits are sometimes also found in astrocytes, microglia, neurons, and the inner and outer loops of myelin sheets (48-50).

There are many mechanisms of iron uptake, transport, and storage, but there is no effective pathway for the excretion of excess brain iron. Apoferritin, the protein moiety of ferritin which is devoid of iron, is synthesized in brain tissue in response to the presence of excess iron. There are 24 subunits in an apoferritin molecule, making it a spherical protein shell with an external diameter of 120–130 Å and a central cavity of about 75 Å. When this spherical protein shell fills with iron to form ferritin, it has a capacity of up to 4500 iron atoms in the form of crystalline hydrous ferric oxide within the inner core of ferritin. Ferritin is abundant in the liver and brain, and ferritin iron is believed to be the most readily mobilizable form of iron deposit in the body. In the case of severe excessive iron presence, granules of insoluble hemosiderin may be formed which are considered to be partially degraded ferritin derivatives with a similar but smaller iron crystal core.

The richness of ferritin and iron observable in some glial cells in sections of brain specimens suggests the important role these cells may play in brain iron

metabolism/regulation, but their physiopathologic significance remains to be established (50). The age dependence of iron concentrations suggests that brain iron deposition may be an important factor not only in early brain development, but also in brain aging (51). During the first few months after birth the brain iron concentration is very low, but it gradually increases and reaches the adult level at around 20 years of age. Then, the iron concentration in most parts of the brain stabilizes (35), except in the putamen where the iron concentration continues to increase slowly with age. The increase of iron deposition in the putamen, and probably also in the globus pallidus and caudate nucleus, accelerates after the seventh decade of age (35, 52). The increased iron deposition might be a factor that contributes to the oxidative stress in the aged brain and therefore could be a threat to the neuronal cells. The concentration of brain iron is independent of its body stores (35), indicating that brain iron is an isolated storage pool of iron for the body. Most of our knowledge about brain iron comes from postmortem observations. Until the mid 1980s when high field strength MRI became available, there was almost no diagnostic value in brain iron because of the lack of any technique for measuring brain iron in-vivo.

Brain iron is detectable by MRI because a portion of the iron, though the exact fraction is unknown, is paramagnetic and exerts relaxation effects upon the water protons. The relaxation effect of brain iron depends greatly upon its physical state (paramagnetic or diamagnetic), form (water accessibility), and distribution at the cellular level. We will discuss separately the relaxation effects of hemoglobin iron in the blood and of the true tissue brain iron.

1.3.2 Hemoglobin and Its Relaxation Effects

Hemoglobin is a global protein present in the red blood cells. Its role is in oxygen transportation. The bonding of molecular oxygen in hemoglobin is facilitated

in part by the heme compounds. Heme is a complex of protoporphyrin IX with Fe^{2+}, and there are four heme compounds in each hemoglobin molecule (53). In deoxygenated hemoglobin where no oxygen molecules are bound to the hemoglobin molecule, the ferrous iron is in a paramagnetic state with an electronic spin of S = 2. In oxygenated hemoglobin (four oxygen molecules per hemoglobin molecule), the heme iron becomes diamagnetic with a spin of S = 0, due to a rearrangement of its electronic wave function. Thus, the magnetic state of the heme iron is a direct function of the oxygenation state of the hemoglobin (54). Yet another form of hemoglobin exists: methemoglobin, in which the heme iron is paramagnetic with an electronic spin of S = 5/2 (55-56). Methemoglobin is formed upon chemical oxidization of hemoglobin, but is present in the body only in the pathological condition of hematoma. The heme iron in methemoglobin not only possesses a larger net electron spin than in hemoglobin, but is also accessible to free water (57). This makes methemoglobin a much stronger relaxation agent than hemoglobin, since the iron in the latter is not accessible to the water.

The relaxation characteristics of water protons in deoxygenated blood were systematically studied first by Thulborn *et al.* (10) and subsequently by others (53-60). The important experimental findings can be summarized briefly as, a) the transverse relaxation rate increases dramatically upon deoxygenation of the hemoglobin in a blood sample containing intact RBC, but increases little if the RBC have been lysed, b) the longitudinal relaxation rate changes little upon deoxygenation of hemoglobin regardless of the integrity of the RBC membrane, c) the increase of transverse relaxation rate has a near quadratic relationship with the fraction of deoxygenated hemoglobin in the sample as well as with the magnetic field strength, and d) the observed transverse relaxation rate in the deoxygenated blood of intact RBC increases if the interecho time in the CPMG sequence increases. Thus, the effect of paramagnetic (deoxygenated)

hemoglobin occurs mainly on the transverse relaxation and not on the longitudinal relaxation. Factors other than deoxygenation, which may include cell membrane integrity, magnetic field strength, and interecho time, also play important roles in this relaxation enhancement. Those findings have led to the conclusion (10) that it is the susceptibility-difference effects created by the RBC compartmentalization of the paramagnetic hemoglobin, combined with appropriate water diffusion rates, that are responsible for the water proton transverse relaxation enhancement in deoxygenated blood.

A new study on blood samples is presented in Chapter 2. It aimed to resolve more clearly the relative contributions to the enhancement from the three types of water diffusion present in the sample: the intracellular diffusion, the extracellular diffusion, and the transmembrane diffusion. A concurrent, independent study by Gillis *et al.* (56) also addressed the same question using a similar, but not identical approach, to ours. The results from our study can be found in Chapter 2, together with some comparisons made between our findings and those of Gillis *et al.*

The understanding of the relaxation enhancement in blood samples helps to explain the hypointensity of sub-acute hematomas in T_2-weighted images at high magnetic field strengths (61). In the evolution of a hematoma (61), the fresh blood bleeding into the acute hematoma is largely oxygenated at first. However, the blood soon becomes deoxygenated, as no new source of oxygen is available in the hematoma. A few days later methemoglobin begins to appear, followed by hemolysis, and finally the hemoglobin/methemoglobin which is released from the chronic hematoma is slowly resorbed by the tissue. This evolution is accompanied by changes in relaxation rates as well as in the water content of the hematoma. When hemoglobin starts to deoxygenate, the T_2 value of the hematoma becomes shorter and shorter, which results in

hypointensity in the T_2-weighted images at high field strengths, while the T_1 values remain unchanged. The relaxation properties of a hematoma at this stage can be studied using deoxygenated blood samples as the model (55, 58).

The effect on the water proton transverse relaxation from changes in the oxygenation states of hemoglobin in blood is also a major mechanism underlying recently developed functional brain activity imaging using high field MRI, so called functional MRI (6-7). In functional MRI, a fast T_2^*-weighted sequence is usually used in imaging the brain before, during, and after a certain task/stimulation is undertaken that results in brain activation. The functionally activated brain tissue, usually restricted to a certain region of the cortex, is found to show an increase in signal intensity in T_2^*-weighted images in response to the stimulation. This is, at least in part, due to the change of the oxygenation level of the blood. Physiologically, in the functionally activated brain tissue, the regional blood flow increases in response to the activation. The increased blood flow brings in more oxygen which exceeds the increased local oxygen consumption, and results in a regionally increased oxygenation level in the vascular bed (62). The capillaries, normally containing partially deoxygenated blood, are in general more "paramagnetic" than the brain tissue so they are like paramagnetic centers. The "paramagnetic" capillaries exert T_2^*-enhancement susceptibility effects on the tissue water. When the blood oxygenation level increases in the local capillary bed (and likely also in the immediate draining veins), the T_2^*-enhancement decreases and the signal intensity of the local tissue water increases in the T_2^*-weighted images. What really happens in the brain activation and the overall mechanisms for the signal change in the T_2^*-weighted images during brain activation is likely more complicated than the above and remains the topic of extensive research (63-66).

1.3.3 Relaxation Effect of Brain Iron

The transverse relaxation enhancement of water protons that is brought about by the paramagnetic brain iron is the most important issue in this study. This issue was first brought to MR researchers' attention in the mid 1980s when high field strength (1.5T) proton MRI became available. It was noticed in the heavily T_2-weighted images or calculated T_2 images, that some basal ganglia structures of the human brain, including the globus pallidus, red nucleus, substantia nigra, and dentate nucleus, were consistently delineated by their remarkable hypointensity relative to their surrounding tissue. This structural contrast was not normally observed in T_1-weighted images. Drayer *et al.* (1) first interpreted this MRI observation as due to selective T_2-shortening brought about by the naturally accumulated, highly concentrated brain iron, for which the anatomical locations matched those of the hypointensity. To validate their interpretation, Drayer *et al.* (1) demonstrated that the pattern of hypointensity in T_2-weighted images was a correlate of Perl's iron staining in postmortem brains, and they also demonstrated the absence of T_2 shortening in infant brains, where iron concentration is very low. Later studies further confirmed brain iron as the source of selective T_2-shortening in both normal and diseased brain images (2, 13, 51). The brain iron related hypointensity can also be clearly seen in T_2-weighted gradient echo images which can be acquired faster using a small tip angle and short TR (67). It is even possible to visualize brain iron, but with poorer contrast, in mid-field (0.5T) MRI by prolonging TR and TE (68). At higher field strengths ($\geq$ 2.0 T), increased hypointensity or shorter T_2 values are observed in iron-rich tissue (69, 70). It was postulated that the signal hypointensity or T_2-shortening in these basal ganglia structures is a correlate of the concentration of iron. As concluded by Drayer (71), this hypothesis was based on a few consistent characteristics, for example, a) the unique anatomical distribution of both the hypointensity and the iron in the brain; b) the absence of hypointensity and iron in

young children; c) the progressive prominence of hypointensity and iron concentration as adulthood is approached; d) the accentuation of putamen hypointensity and postmortem iron concentration with aging; e) the close correspondence of MRI and postmortem findings of iron distribution in animal studies; f) the absence of the hypointensity at low field strength and the further accentuation of hypointensity at field strengths greater than 1.5 T; and g) the utility of exaggerated or abnormally distributed hypointensity in diagnosing diseases with known abnormal iron accumulation. However, this correlation was not perfect. Even in a very early study, Rutledge *et al.* (2) emphasized that between MRI signal hypointensity and Perl's iron staining, the correlation was close but not perfect in the basal ganglia. The caudate and putamen are moderately stained but generally show no (caudate) to mild (putamen) signal hypointensity. In the more precise quantitative in-vitro studies using unfixed fresh brain specimens, Chen *et al.* (19-20) found that neither iron nor ferritin concentration showed any consistent correlation with proton T_2 values. This was probably because the iron concentration, even in the brain regions of richest iron content, is still lower than the threshold value that would be required for the iron-related relaxation to become dominant in brain tissue (19-20). Rather, even at 1.5 T, proton relaxation is still largely determined by tissue properties such as water content, water diffusion, and water exchange, which are not related to iron content. The contributions from the paramagnetic iron are only modifiers of the overall tissue relaxation. The biological variations of the other dominant sources of relaxation which are independent of iron and can be large in normal or pathological conditions, may obscure the correlation between the tissue relaxation times and the iron concentration. Therefore, T_2-weighted images, as well as calculated T_2 images, though continuing to be a valuable imaging tool in the detection of iron abnormalities in the brain, are not specific or sensitive enough to be a reliable quantitative measure for iron deposition.

Possible improvements of the specificity of the relaxation technique in measuring brain iron could come through an understanding of the relaxation mechanisms through which brain iron exerts its relaxation enhancement effect on the water proton magnetization. At the molecular level, proton relaxation enhancement due to brain iron was first related to ferritin by Drayer *et al.* (1) who noticed that the remarkable dominance of the T_2 effect was similar to ferritin-enhanced relaxation in liver. Relaxation enhancement in ferritin solutions is often used as a model to understand relaxation enhancement in the brain (2, 69,72-73). Relaxometry study of ferritin solutions revealed the different relaxation effects on T_1 and T_2 due to the iron core of ferritin (74). The T_1 relaxation is only mildly enhanced by a small number of ferric ions bound to the protein shell, through electron-proton spin-spin relaxation, which also enhances T_2 relaxation to a similar magnitude. The iron sequestered in the ferritin core has little effect on T_1, but does affect T_2. The magnitude of this transverse relaxation enhancement is beyond that predicted by outer sphere relaxation theory (38, 74).

Before 1990, theories of the relaxation enhancement of water diffusion through local field inhomogeneities predicted a quadratic field strength dependence of the enhancement (38-39), but this was contradicted by the brain relaxation measurements where the observed relaxation enhancement increased at a rate much less than the square of the applied field strength (69-70, 75). In 1992, an experimental T_2 measurement of ferritin solutions at field strengths from 0.04 to 1.5 T revealed a remarkably linear field strength dependence of the transverse relaxation rate (73), the slope of which correlated with the iron concentration in solution. Based on the experimental results from ferritin solutions, the field strength dependence of the proton relaxation rate has been proposed as a quantitative, iron-specific measure in brain. The results from a few pilot studies have been positive (72, 76).

The relaxation enhancement observed in ferritin solutions may reveal only part of the possible relaxation enhancement that brain iron can exert on water protons. Brain tissue is a much more complicated system than a ferritin solution, and factors such as the physical state, form, and cellular distribution of iron can affect relaxation enhancement significantly. For example, the known heterogeneous cellular localization of iron will have important effects on T_2 relaxation. Because it is sequestered in glia, iron will give rise to a localized heterogeneity on susceptibility, which in turn will produce local field inhomogeneities in the presence of a static magnetic field. Through its susceptibility-difference effect, this heterogeneous cellular distribution of iron can be a significant source of relaxation enhancement, but it is not present in ferritin solutions. An early attempt to exploit the heterogeneous iron distribution proposed the use of combined spin echo and gradient echo imaging to determine the line broadening component as a measure of the microscopic field inhomogeneity (77). However, it failed to show any sensitivity to natural brain iron using a 1.5 T system (78). A similar, but improved, technique has recently demonstrated a significant sensitivity to abnormal iron content in Parkinson's disease using a 3 T system (79).

In this thesis we propose to exploit the interecho time dependence of the transverse relaxation enhancement in brain for the purpose of iron quantification. The interecho time dependence of the transverse relaxation of water protons is not present in ferritin solutions. However, when intact red blood cells were introduced into a ferritin solution, the apparent transverse relaxation rate showed a large increase and a significant interecho time dependence (80). In brain tissue, the iron-rich glial cells are sparsely distributed and occupy only a small fraction of the tissue space. The size of the oligodendrocytes, in which sequestered brain iron is normally seen (50), is about 10 to 20 μm (81). Meaningful relaxation enhancement due to the susceptibility-difference effect can be expected in brain tissue when the iron concentration is high. The

evaluation of the susceptibility-difference hypothesis will be the main topic of this thesis.

1.4 Parkinson's Disease

1.4.1 Parkinson's Disease

Parkinson's disease (PD), sometimes called idiopathic parkinsonism to differentiate it from other parkinsonian syndromes, is a common chronic neurological illness of adult life and is characterized by features of motor movement deficiency (82-85). The name of this disease comes from James Parkinson, a nineteenth century London physician who described the clinical features of the disease and presented it as a distinct human condition. In his famous *Essay on the Shaking Palsy* published in 1817, Parkinson recorded many of the important features of the disease (which he called the shaking palsy or paralysis agitans), including the tremor at rest, flexed posture, festinant gait, dysarthria (difficulty in articulating words), dysphagia (difficulty in swallowing), and constipation.

Parkinson's disease may have affected people long before James Parkinson's time and probably affected individuals having been described earlier by Leonardo Da Vinci and others. It is still with us today, with a seemingly steady prevalence ratio of up to 200 per 100,00 population (86). Parkinson's disease is a disease primarily of late middle age and beyond. The mean age at onset is 58 to 62 years, and the mean age of patients with PD living in the community (i.e., the prevalent cases at a certain time) is 67 to 68 years. Therefore, the age-specific prevalence ratio increases after the age of 50 years. The proportionally highest occurrence of PD is in the age group of 70-79 years, with up to 1.5% of individuals in this age group affected (86).

1.4.1.1 Motor Features of Parkinson's Disease

A motor symptom complex called parkinsonism, of which Parkinson's disease (PD) or idiopathic parkinsonism is the most common cause, consists of rest tremor, bradykinesia (slowness of movement), rigidity, and impaired postural reflexes (87). The above are the four cardinal (primary) signs of parkinsonism. Other motor findings in parkinsonism include hypomimia ("masked faces"), hypokinetic dysarthria (speed disturbance), hypophonia (low voice of speech), dysphagia (difficulty in swallowing), micrographia (handwriting that becomes smaller as it runs across the page), shuffling and short-step gait, festination (hurry and pulsion), freezing, stooped posture, and dystonia (disordered tonicity of muscle).

Bradykinesia (slowness of movement) is part of a spectrum of symptoms including akinesia (absence of movement) and hypokinesia (poverty of movement). It is the most characteristic symptom of basal ganglia dysfunction in PD and may be manifested as a delay in the initiation, and by slowness of execution, of a movement. An extreme degree of bradykinesia is akinesia, a state of complete immobility. In this state a patient may fail to initiate or to continue the movement of his/her will (such as speech, handwriting, or gait) for seconds, minutes, or even hours. Most of the neurophysiological and neurobehavioral studies of PD have concluded that the basal ganglia (and possibly the supplementary motor cortex) plays a critical role in planning and in sequencing voluntary movements. The inability to combine motor programs into complex sequences seems to be a fundamental motor deficit in PD.

Tremor is one of the most recognizable symptoms of PD. However, only half of all patients present with tremor at the initial manifestation of PD, and 15% never develop tremor during the course of the illness. When tremor is present it tends to occur at rest and to disappear with movement. Sometimes it is confined to the hand and

has a characteristic "pill-rolling" quality with a rhythm of 4 to 7 Hz. The severity of tremor can be adversely affected by emotional pressure or anxiety of the patient. The biochemical defect underlying the parkinsonian tremor is unknown.

The second commonly mentioned symptom of Parkinsonism following tremor is rigidity or stiffness. Rigidity may contribute to the subjective stiffness and tightness of which patients often complain. On examination, PD patients tend to display muscular stiffness throughout the range of passive movement in a limb segment. This stiffness has a plastic or "lead pipe" quality and can be of intense severity. This stiffness may be regularly interrupted at a frequency of 5-8 Hz. The neurophysiological mechanisms of rigidity is still poorly understood and there is no single agreed-on explanation for rigidity.

Postural instability, or the loss of balance associated with propulsion and retropulsion, is one of the most disabling of all parkinsonian symptoms. Patients with this problem may experience frequent falls, usually after PD has progressed for many years. The gait and postural problems associated with PD probably result from a combination of bradykinesia, rigidity, and other defects in the related central and spinal neural systems.

1.4.1.2 Pathology and Treatment of Parkinson's Disease (85, 88-89)

The major pathology of PD includes the presence of Lewy bodies in affected neurons, a loss of pigmented neuronal cells from the substantia nigra (SN), and a deficit in the neurotransmitter dopamine in the nigrostriatal system.

The Lewy body, an eosinophilic (staining readily with eosin, a dye) inclusion in affected neurons, is generally regarded as a histological marker of PD. In idiopathic PD, Lewy bodies in the SN and elsewhere are the rule. However, Lewy bodies also

occur in the SN and locus ceruleus in up to 10% of nonparkinsonian individuals coming to autopsy after the age of 60 years. This has led to the idea that there may be a large pool of individuals with "Lewy body disease" and subclinical parkinsonism.

Loss of the pigmented neurons from the zona compacta of the SN is a major pathological feature of PD. The pigment of these neurons comes from neuromelanin and is a marker of dopaminergic and noradrenergic neurons. Neuromelanin are complex heterogeneous polymers resulting from the oxidative polymerization of subunits in catecholamine metabolism. In PD, the affected neurons are dopaminergic whose axons extend to the striatum and form the dopaminergic nigrostriatal pathway. The loss of neurons from the SN correlates well with the severity of parkinsonism, but this loss presently can only be assessed postmortem. In general, it is thought that about 80-85% of nigral neurons must be lost, depleting the striatum of at least 80% of its dopamine content before clinical manifestations of PD appears, although recent studies with positron emission tomography (PET) suggests a slightly lower critical level of this depletion. This gives a sense that the pathology may have progressed for some time before the initial onset of a patient's symptoms.

Parkinson's disease is the first illness established as being due to an abnormality of a neurotransmitter, i.e., dopamine. The nigrostriatal pathway is the major dopaminergic pathway in the brain. Normally, in the presynaptic terminals of the dopaminergic neurons, dopamine is synthesized by first converting tyrosine (a neutral amino acid) to levodihydroxyphenylalanine (levodopa or L-dopa) by the enzyme tyrosine hydroxylase, and subsequently converting L-dopa to dopamine by the enzyme L-dopa decarboxylase (Figure 1.2). The dopamine is subsequently released from the presynaptic terminals and binds with the dopamine receptors on the postsynaptic membrane. The action of dopamine on postsynaptic receptors is terminated primarily

by two processes. About 80% of the released dopamine is taken up by the presynaptic nerve ending, the remaining 20% being degraded by the enzyme catechol-O-methyl transferase. The loss of nigral neurons results in a decreased ability to release dopamine in the striatum and ultimately causes a breakdown of the normal neuronal signal transmission of this pathway. Both presynaptic and postsynaptic compensation (an increase in presynaptic activity and an increase in receptor sensitivity) may occur to overcome the initial cell loss. The compensation probably prevents the appearance of symptoms and signs of PD in the early stages of the illness. The discovery, by Ehringer and Hornykiewig in 1960 that there was a striking deficit of dopamine in the striatum of parkinsonian brains opened the door for an effective therapy.

Because dopamine itself cannot cross the blood-brain barrier, L-dopa as its natural precursor (Figure 1.2) was used in the treatment of the symptoms of PD in 1961. Later, peripheral decarboxylase inhibitors (PDI) were introduced which can block the peripheral decarboxylation of L-dopa in the gut wall, liver, and brain capillary endothelium, therefore allowing more of a given dose of L-dopa to reach the brain. The combination of L-dopa and PDI remains the most effective medication in the treatment of PD symptoms. An alternative approach to compensate for the dopamine deficit in the nigrostriatal pathway is to administer dopamine agonists such as bromocriftine or pergolids. These drugs mimic the action of dopamine on postsynaptic receptors.

Since the introduction of L-dopa treatment the quality of life of patients with PD has improved dramatically, and a majority of patients have a normal life span. However, the treatment does not stop the progression of the disease, and the motor symptoms slowly progress. After several years of treatment a patient may develop motor fluctuations in response to L-dopa. Typical fluctuations include end-dose deterioration (related to the timing of L-dopa intake), random off periods (unrelated to

L-dopa), and dyskinesia. Regular and frequent attention from the physician is required at this stage to monitor the response to medication, and to adjust dose or to prescribe alternative medications when necessary.

1.4.1.3 Etiology of Parkinson's Disease (86, 90)

As the term implies, the causes of the idiopathic Parkinson's disease remain unknown. Analytic epidemiology studies indicate that genetic factors are not important in most patients and that PD is not associate with sex, residence, occupation, or social status (86). No definite risk factors have been identified. Although premature or accelerated aging has been suggested as an important pathogenic mechanism, the observed pattern of incidence (the rate at which new cases occur in a given population) clearly shows a decrease after the age of 80, and the pattern does not support aging as the sole factor underlying the disease. A popular hypothesis is that environmental factors such as toxins (exogenous or endogenous) superimposed on other factors including individual susceptibility and perhaps age may be the major cause of idiopathic PD.

A toxic cause of PD has not been identified. However, we do know a variety of toxins linked to parkinsonism in humans. Encephalitis lethargica, caused by viral infection, leads to the development of severe parkinsonian symptoms among its survivors (post-encephalitic parkinsonism). Toxic chemicals including manganese (Mn), carbon monoxide, carbon disulfide, cyanide, methanol, and 1-methyl-4-phenyl-1,2,3,6-tetrahydropyridine (MPTP) can cause parkinsonism. Among these toxins, MPTP, a chemical used in the synthesis of more complex compounds, can induce symptoms similar, though not identical, to idiopathic PD in terms of clinical, pathologic, and biochemical features. Detailed studies of the mechanism of action of MPTP in animal models have led to a dramatic advance in our knowledge about how a

toxin can selectively damage the nigral cells and have led to the hypothesis that oxidant stress in the SN may be responsible for the development of PD.

1.4.2 Hypothesis of Oxidant Stress in Parkinson's Disease

This hypothesis developed when the mechanism of MPTP selective damaging the nigral cell was elucidated. It postulated (91-92) that oxidant stress could build up in the brain as a result of excess oxygen-based free radical species and of reduced protective capacity against free radical insult. It further postulated that such an oxidant stress in the SN could lead to neuronal degeneration seen in PD. (A supplement to Annals of Neurology, volume 32, 1992, was devoted entirely to the discussion of the role of iron and oxidant stress in the normal and parkinsonian brain.)

MPTP is a lipophilic molecule which rapidly enters the brain. There is an enzyme, monoamine oxidase B (MAO-B), located in glial cells that metabolizes it to the unstable product 1-methyl-4-phenyl-2,3-dihydropyridinium ($MPDP^+$). From $MPDP^+$, the 1-methyl-4-phenylpyridinium species (MPP^+) is formed (Figure 1.3). Because MPP^+ is a substrate for the dopamine uptake system, it accumulates in nigral neurons. MPP^+ accumulates in mitochondria where it inhibits nicotinamide adenine dinucleotide (NAD^+)-linked oxidation in complex I in the electron transfer chain and causes cell death. Complex I is one of the important enzyme complexes found in mitochondrion.

In PD, neuronal degeneration could result from membrane damage induced by oxygen free radicals. Free radicals are atoms or molecules that contain an orbital filled with an unpaired electron. Most free radicals are unstable and highly reactive. Common oxygen-based free radicals include superoxide (O_2^-), hydrogen peroxide

(H_2O_2), and hydroxyl free radical ($HO^{\cdot}$) -- all capable of damaging virtually any biological molecule, including DNA, essential proteins, and membrane lipids.

There are two arguments that support the presence of excessive free radicals in the nigral cells in PD. The first is that H_2O_2 is produced in the nigral neurons as a result of dopamine metabolism, either enzymatically by MAO or by autoxidation. When H_2O_2 is not effectively cleared, it can react with ferrous iron and generate the highly reactive $HO^{\cdot}$ which can initiate lipid peroxidation and cause membrane damage and cell death. Equation [1.42] is the so called Fenton reaction

$$H_2O_2 + Fe^{2+} \longrightarrow HO^{\cdot} + OH^{-} + Fe^{3+} \qquad [1.42]$$

whereby hydrogen peroxide (H_2O_2) can accept an electron from Fe^{2+} to form the hydroxyl radical ($HO^{\cdot}$). There is some supportive evidence for this argument. For example, there is a reduction in the levels of reduced or total glutathione in the SN in PD suggesting that the major pathway of detoxification of H_2O_2 via oxidation of glutathione may be less effective than in normal brains. The SN is one of the few brain regions that contains a high concentration of iron — a transition metal readily exchangeable between its two chemical states: ferrous (Fe^{2+}) and ferric (Fe^{3+}). The abundant availability of iron may promote the formation of $HO^{\cdot}$ from H_2O_2. The iron concentration has been found to be even higher in the SN of PD patients than in normal controls (see 1.4.3.1), which may be an important factor contributing to the oxidant stress. Another possibility is that, as in the MPTP treated case, complex I in the mitochondria of nigral cells may also be inactive, leading to excessive free radicals from the respiration chain. This is supported by the findings that there is a reduction in the level of complex I activity in the SN (and perhaps also in platelets and skeletal muscles) in PD.

1.4.3 Brain Iron in Parkinson's Disease

Brain iron is a potential endogenous toxin that may contribute to the characteristic neuronal changes in PD (93). As is the case for iron in the normal brain, our knowledge about the iron status in PD and about its potential role in PD pathogenesis is limited. Further study of brain iron function and of its relation to parkinsonian symptomatology may help to determine whether iron accumulation directly relates to the etiology of PD, or whether it is a secondary phenomenon of less etiologic significance. Magnetic resonance imaging, via the iron-related relaxation contrast, provides a non-invasive tool for the in-vivo evaluation of PD and other parkinsonian disorders.

1.4.3.1 Brain Iron Increase in Basal Ganglia in Parkinson's Disease

As early as 1968 a study by Earle (94) found an increase in iron content in formalin-fixed sections of the midbrain of PD patients. Evidence from recent postmortem studies (95-99) supports the finding of an excessive level of iron in the SN of PD patients. The reported amount of increase of total iron in the SN ranges from 35% (97) to 76% (95). In contrast, Uitti *et al.* (100) reported no change of the total iron content in the SN. Differences in the technique of iron analysis, in specimen processing, in the degree of disease severity, and perhaps in the biological brain iron variation of the controls may have caused the discrepancy in the quantitative findings. Although most investigators in the field accept that there is a detectable increase of iron in the SN of PD patients, there is controversy regarding the degree of increase, the form of the excess iron, and the relationship between the iron increase and the presence of PD.

In the other regions of the basal ganglia, putamen (PM) and globus pallidus (GP), the iron status in PD is even more controversial. No significant change of iron level was found in these structures by Sofic *et al.* (95). Iron level was found to be normal in the PM and decreased in the GP by Dexter *et al.* (97). In contrast, a recent study of fresh brain samples using atomic absorption spectroscopy analysis showed iron levels both in the PM and in the GP to be significantly increased in PD compared to age-matched controls (average increase ~30% in the PM and the GP) (20). Also, it should be noted that PD is not the only movement disorder associated with elevated iron deposition. Other movement disorders that show increased iron deposition in the basal ganglia may include Shy-Drager syndrome (13-15, 101), progressive supranuclear palsy (13, 101), Huntington's disease (2, 20), and multiple sclerosis (102). The abnormality of iron deposition in these diseases is sometimes larger than in PD. Therefore, the potential application of an MRI quantification to brain iron is not limited to PD.

1.4.3.2 Iron Contrast in the MRI Study of Parkinson's Disease

Magnetic resonance imaging has become one of the major imaging modalities of neuroradiology. At high magnetic field strengths (1.5 T and above), paramagnetic iron-based T_2 contrast provides a clear delineation of some of the midbrain structures (see section 1.3.3). This suggests the suitability of high field MRI for the study of neurodisorders that involve degeneration of the midbrain, including parkinsonian disorders.

Parkinsonian disorders are characterized by their common motor features of parkinsonism, as described in 1.4.1.1. Idiopathic Parkinson's disease is the most common type of the parkinsonian disorders. As discussed in 1.4.1.2, PD pathology involves primarily the SN, and its motor symptoms can be controlled with L-dopa

therapy for a relatively long period of time. Some other parkinsonian disorders share many of the common features of PD, but are pathologically distinguishable from PD. Patients with these disorders usually have symptoms which progress more rapidly and which respond poorly to L-dopa treatment. They are often classified as having parkinsonian (plus) syndromes (PS) (13). Parkinsonian syndromes may account for up to 25% of patients with parkinsonian features and encompass several distinct neurodegenerative disorders which include striatonigral degeneration, Shy-Drager syndrome, olivopontocerebellar atrophy, and progressive supranuclear palsy. Differential diagnosis of PS from PD in the initial stage is sometimes challenging.

In the evaluation of MRI as a potential diagnostic tool for PD and PS, some common features of iron-based contrast have been noticed in heavily T_2-weighted images (2, 13-18). These findings include putamen hypointensity in patients with PS (14-15), a reduction of SN pars compacta width in PD (16), and a restoration of signal in the dorsal lateral aspect of SN in PD patients (2). Stern *et al.* (18) found that moderate to severe putamen hypointensity was more common in PS than in PD and controls. They also confirmed a reduction of the width of SN pars compacta in both PS and PD patients relative to controls. Accurate analysis of the SN with MRI is difficult, however, because of the small size of the SN which makes patient position and partial volume effects complicating factors in the analysis (51). Signal restoration in the SN was not confirmed for either PS or PD in Stern's study (18). The iron-based signal abnormalities in PS and PD, combined with other imaging features such as observable brain stem atrophy in PS, makes MRI useful in differentiating PS from PD. The subtle MRI abnormalities observed in PD patients, however, do not seem of value in PD evaluation. This may reflect a simple fact that conventional T_2-weighted imaging is neither sensitive nor specific enough to reveal the brain iron abnormalities in PD that have been observed in the in-vitro studies.

The recent development of novel relaxation imaging techniques is making MRI more useful in the quantification of brain iron. T_2 and T_2^* measurement at 3.0 T (79) has demonstrated a highly significant increase in the derived line broadening (relaxation) component in the SN of PD patients compared to controls. In Chapter 6 we report our MRI measurement of the regional iron content in a group of patients with PD. That measurement demonstrated its potential value in evaluation of the disease severity. With further improvement and testing of these new techniques, MRI may become a very useful tool in the study and monitoring of the progression of PD.

1.4.4 Parkinson's Disease Rating Scales

In the clinical management of patients as well as in the research study of PD, it is necessary to evaluate the degree of PD affecting a patient (103). The evaluation generally consists of assessment and recording the severity of the disease, its progression, and the response to a therapy. After the effective L-dopa treatment became available, efficacy checking of the new drugs increasingly demanded a reliable clinical evaluation technique. Parkinson's disease rating scales (PDRSs) are currently the most widely used means in the clinical evaluation of PD (A thorough review of PDRSs can be found in reference (103)).

Parkinson's disease rating scales customarily rate symptoms, signs, and functional disability. They are based on direct clinical evaluation that is largely qualitative and often subjective. Some PDRSs include quantitative and objective evaluations using physical measurements on patients performing specific physical testing tasks. Symptoms and signs (such as tremor, rigidity, bradykinesia, gait abnormality, postural instability, facial expression, and speech), and functional disability (such as walking, eating and feeding, dressing, hygiene, bathing, and speech) are the two aspects most widely checked in the PDRSs. Although many PDRSs have

been developed in the past three decades, only a few have reached wide acceptance. The PDRSs we use in Chapter 6 include those of Hoehn and Yahr (104), Schwab and England (105), and the Unified Parkinson's Disease Rating Scale (UPDRS) (106). The Hoehn and Yahr classification includes five stages of disease severity. It has limited value in comparing small differences between patients or in recording subtle progression of an individual patient. The Schwab and England activity of daily life scale measures the patient's functional disability by assessing the degree to which the patient is independent in his/her daily living activities. The UPDRS was developed in 1984 as a comprehensive rating scale. Its motor subscore (section 18-42 of UPDRS) assesses the PD patient's motor symptoms and signs, using a well defined and specific scoring system.

These clinical features may not truly reflect the pathological severity of PD. There are several practical problems in using PDRSs. Parkinson's disease rating scales are subject to inter-observer and intra-observer variability since they are largely based on a subjective assessment of motor functional deficits. The rating obtained with PDRSs are greatly affected by the treatment status of the individual patients because a patient's functional state is not only determined by the severity of the nigral cell loss, but also by the effects of anti-parkinsonian medications. These difficulties can affect the accuracy of clinical trials in evaluating the effects of drugs which may alter the progression of PD pathology. Therefore, an alternative method of objective assessment of PD severity using non-invasive techniques such as MRI is desirable.

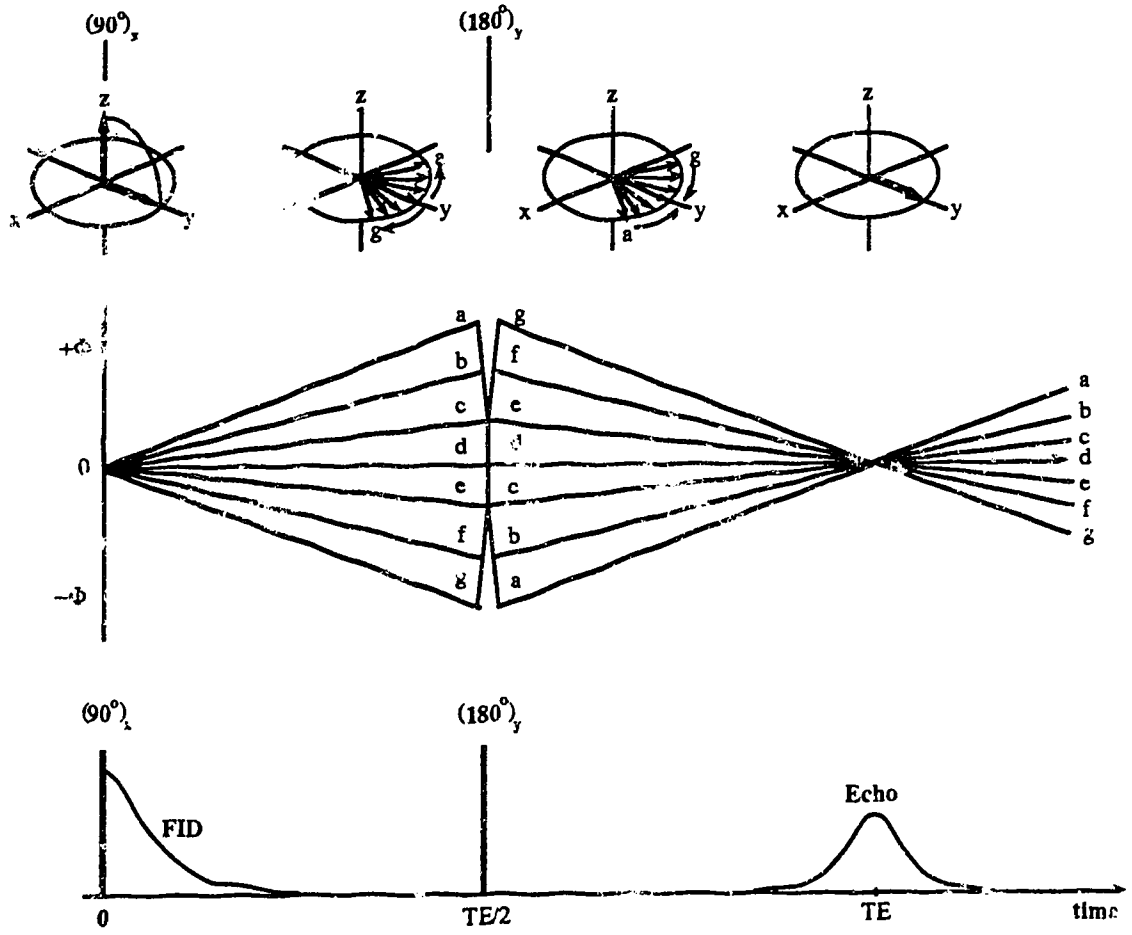

Figure 1.1. An illustration of the formation of a spin echo. The original longitudinal magnetization is rotated around the x-axis by the excitation pulse, $(90°)_x$, into the transverse plane of the rotating frame. The magnetization vectors of all the spin isocromats point in the same y-direction at time zero. At $t > 0$, the isocromatic magnetization vectors start to fan out in the "dephasing" period (first half of the TE period) because of the field inhomogeneity that is experienced by the isocromats, this results in a different phase (Φ) accumulation for each isocromat. The effect of the refocusing pulse, $(180°)_y$, is to flip the magnetization around the y-axis, which results in a phase reversal, i.e. the phase Φ changes the sign. In the "refocusing" period (second half of the TE period), the newly accumulated phase progressively cancels the phase whose sign was changed by the refocussing pulse. As a result, the magnetization vectors refocus and a spin echo forms at the time TE.

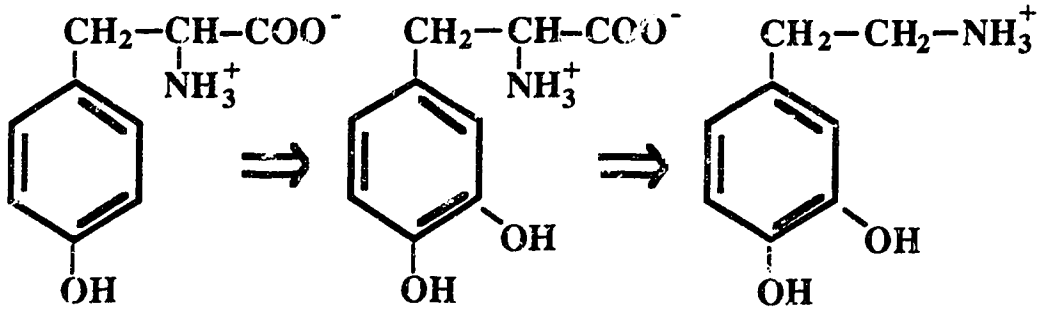

Figure 1.2. Natural synthesis of dopamine in the dopaminergic neurons. In the presynaptic terminals, amino acid tyrosine is converted to L-dopa by the enzyme tyrosine hydroxylase; L-dopa is subsequently converted to dopamine by the enzyme L-dopa decarboxylase.

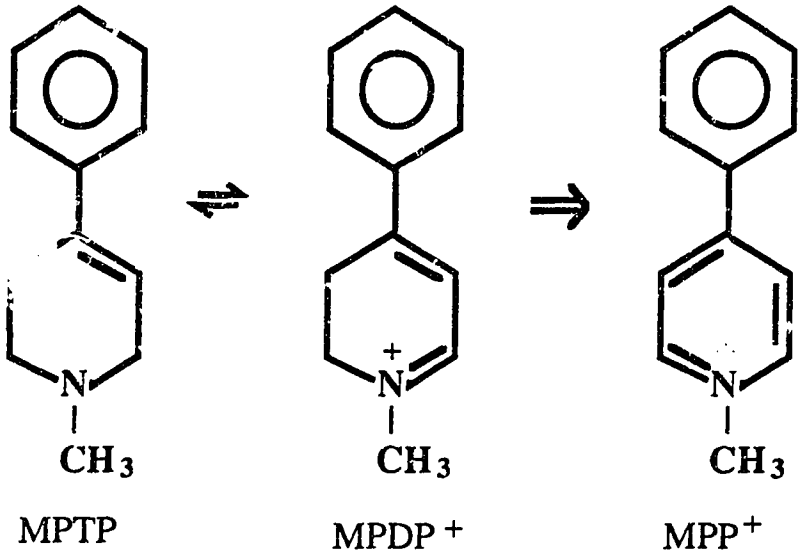

Figure 1.3. MPTP and its conversion to MPP^+.

1.5 References

1. B. Drayer, P. Burger, R. Darwin, S. Riederer, R. Herfkens, G. A. Johnson, MRI of brain iron. *AJR* 147, 103-110 (1986).

2. J. M. Rutledge, S. K. Hilal, A. J. Silver, R. Defendini, S. Fahn, Study of movement disorders and brain iron by MR. *AJNR* 8, 397-411 (1987).

3. D.D. Stark, M.E. Moseley, B.R. Bacon, A.A. Moss, H. I. Goldberg, N. M Bass, T. L. James, Magnetic resonance imaging and spectroscopy of hepatic iron overload, *Radiology* 154, 137-142 (1985).

4. J.C. Gore, R.P. Kennan and J. Zhong, MRI contrast agents–principles and constraints, *in* "The Physics of MRI, Proc. AAPM Summer School, 1992, Banff" (M.J. Bronskill and P. Sprawls, Eds), p478-506, American Institute of Physics, Woodbury, NY, 1993.

5. A.D. Watson, S.M. Rocklage, M.J. Carvlin, Contrast agents, *in* "Magnetic Resonance Imaging" (D.D.Stark, W.G. Bradley, Eds), p372-437, Mosby-Year Book,Inc., St. Louis, 1992.

6. S. Ogawa, D.W. Tank, R. Menon, J.M. Ellerman, S. Kim, H. Merkle, K. Ugurbil, Intrinsic signal change accompanying sensory stimulation: Functional brain mapping with magnetic resonance imaging. *Proc. Natl. Acad. Sci. (USA)* 89, 5951-5955 (1992).

7. K.K. Kwong, J.W. Belliveau, D.A. Chesler, I.E. Goldberg, R.M. Weisskoff, B.P. Poncelet, D.N. Kennedy, B.E. Hoppel, M.S. Cohen, R. Turner, H. Cheng, T.J. Brady, B.R. Rosen, Dynamic magnetic resonance imaging of human brain activity during primary sensory simulation. *Proc. Natl. Acad. Sci. (USA)* 89, 5675-5679 (1992).

8. I. Solomon, Relaxation processes in a system of two spins, *Phys. Rev.* 99, 559 (1955).

9. N. Bloembergen, Proton relaxation times in paramagnetic solutions, *J. Chem. Phys.* 27, 572 (1957).

10. K.R. Thulborn, J.C. Waterton, P.M. Matthews, and G.K. Radda, Oxygenation dependence of the transverse relaxation time of water protons in whole blood at high field. *Biochem. Biophys. Acta* 714, 265-270 (1982).

11. C.R. Fisel, J.L. Ackerman, R.B. Buxton, L. Garrido, J.W. Belliveau, B.R. Rosen, and T. Brady, MR contrast due to microscopically heterogeneous magnetic susceptibility: numerical simulations and applications to cerebral physiology. *Magn. Reson. Med.* 17, 336-347 (1991).

12. R.P. Kennan, J. Zhong, J.C. Gore, Intravascular susceptibility contrast mechanisms in tissue. *Magn Reson Med* 31, 9-21 (1994).

13. B.P. Drayer, Imaging of the aging brain, part II. pathologic conditions. *Radiology* 166, 797-806 (1988).

14. B.P. Drayer, W.Olanow, P. Burger, G.A. Johnson, R. Herfkens, S. Riederer, Parkinson plus syndrome: diagnosis using high field MR imaging of brain iron. *Radiology* 159, 493-498 (1986).

15. B. Pastakia, R. Polinsky, G. DiChiro, J.T. Simmons, R. Brown, L. Wener, Multiple system atrophy (Shy-Drager syndrome): MR imaging. *Radiology* 159, 499-505 (1986).

16. J.R. DuGuid, R. De La Paz, J. DeGrott, Magnetic resonance imaging of the midbrain in Parkinson's disease. *Ann Neurol* 20, 744-747 (1986).

17. J.N. Rutledge, Magnetic resonance of movement disorders, *in* "Parkinson's Disease and Movement Disorders" (J. Jankovic, E. Tolosa, Eds), pp511-530, Williams & Willkins, Baltimore, 1993.

18. M.B. Stern, B.H. Braffman, B.E. Skolnick, H.I. Hurtig, R.I. Grossman, Magnetic resonance imaging in Parkinson's disease and parkinsonian syndromes. *Neurol* 39, 1524-1526 (1989).

19. J.C. Chen, P.A. Hardy, M. Clauberg, G. Joshi, J. Parravano, J.H.N. Deck, R.M Henkelman, L.E. Becker, W. Kucharczyk, T2 values in the human brain: comparison with quantitative assays of iron and ferritin. *Radiology* 173, 521-526 (1989).

20. J.C. Chen, P.A. Hardy, W. Kucharczyk, M. Clauberg, G. Joshi, A. Vourlas, M. Dhar, R.M. Henkelman, MR of human postmortem brain tissue: correlative study between T2 and assays of iron and ferritin in Parkinson and Huntington disease. *AJNR* 14, 275-281 (1993).

21. A. Abragam, "The Principles of Nuclear Magnetism," Oxford University Press, Oxfort, 1961.

22. C.P. Slichter, "Principles of Magnetic Resonance", Springer-Verlag, Heidelberg, 1990.

23. J.K.M. Sanders, B.K. Hunter, "Modern NMR Spectroscopy", Oxford University Press, Oxfort, 1987.

24. D. Shaw, "Fourier Transform NMR Spectroscopy", Elsevier Scientific Publishing Company, Amsterdam, 1976

25. I.R. Young, G.M. Bydder, S. Khenia, A.G. Collins, Assessment of phase and amplitude effects due to susceptibility variation in MR imaging of thr brain, *J Comput Assist Tomogr*13, 490-494 (1989).

26. E.L. Hahn, Spin echoes, *Phys Rev* 80, 580-594 (1950).

27. H.Y. Carr, E.M. Purcell, Effects of diffusion on free precession in nuclear magnetic resonance experiments, *Phys Rev* 94, 630 (1954).

28. S. Meiboom, D. Gill, Modified spin-echo method for measuring nuclear relaxation times. *Rev. Sci. Instum.* 29, 688-693 (1958).

29. D.D. Stark, W.G. Brandley, (Eds), "Magnetic Resonance Imaging", Mosby-Year Book,Inc., St. Louis, 1992.

30. M.L. Wood, Fourier imaging, *in* "Magnetic Resonance Imaging" (D.D.Stark, W.G. Bradley, Eds), p21-66, Mosby-Year Book,Inc., St. Louis, 1992.

31. R.E. Hendrick, U. Raff, Image contrast and noise, *in* "Magnetic Resonance Imaging" (D.D.Stark, W.G. Bradley, Eds), p109-114, Mosby-Year Book,Inc., St. Louis, 1992.

32. G.D. Fullerton, Physiologic basis of magnetic relaxation, *in* "Magnetic Resonance Imaging" (D.D.Stark, W.G. Bradley, Eds), p88-108, Mosby-Year Book,Inc., St. Louis, 1992.

33. N. Bloembergen, E.M. Purcell, R.V. Pound, Relaxation effects in nuclear magnetic resonance absorption, *Phys Rev* 73, 679 (1948).

34. E.A. Boudreaux, L.N. Mulay, "Theory and Application of Molecular Paramagnetism", John Wiley & Sons, Inc., New York, 1976.

35. B. Hallgren, P. Sourande, The effect of age on the non-haemin iron in the human brain. *J Neurochem* 3, 41-51 (1958).

36. R.B. Lauffer, Paramagnetic metal complexes as water proton relaxation agents for NMR imaging: theory and design, *Chem Rev* 87, 901-927 (1987).

37. P. Stilbs, Fourier transform pulsed-gradient spin-echo studies of molecular diffusion, *Progress in NMR spectroscopy* 19, 1-45 (1987).

38. P Gillis and S.H. Koenig, Transverse relaxation of solvent protons induced by magnetized spheres: Application to ferritin erythrocytes and magnetite. *Magn. Reson. Med.* 5, 323-345 (1987).

39. S. Majumdar and J.C. Gore, Studies of diffusion in random fields produced by variations in susceptibility. *J. Magn. Reson.* 78, 41-55 (1988).

40. P. Hardy, R.M. Henkelman, Transverse relaxation rate enhancement caused by magnetic particulates. *Magn. Reson. Imaging* 7, 265-275 (1989).

41. R.M. Weisskoff, C.S. Zuo, J.L. Boxerman, B.R. Rosen, Microscopic susceptibility variation and transverse relaxation: theory and experiment, *Magn Reson Med* 31, 601-610 (1994).

42. C.R. Fisel, J.R. Moore, L. Garrido, J.L. Ackerman, B.R. Rosen,T.J. Brady, A general model for susceptibility-based MR contrast, *in* "Proc., SMRM, 9th Annual Meeting, Amsterdam, 1989," p. 324.

43. F. Moiny, P. Gillis, A. Roch, R. N. Muller, Transverse relaxation of superparamagnetic contrast agents: a numerical analysis, *in* "Works in Progress, SMRM, Berlin, 1992", p1431.

44. M.B.H. Youdim, D. Ben-Schachar, P. Riederer, Iron in brain function and dysfunction with emphasis on Parkinson's disease, *Eur. Neuroi.* 31(suppl), 34-40 (1991).

45. K.R. Thulborn, A.G. Sorensen, N.W. Kowall, A. Mckee, A. Lai, R. C. McKinstry, J. Moore, B. R. Rosen, T. J. Brady, The role of ferritin and hemosiderin in the MR appearence of cerebral hemorrhage: A histopathologic biochemical study in rats, *AJNR* 11, 291-297 (1990).

46. O.J. Rafaelsen, B. Kofod, Iron, *in* "Handbook of Neurochemisty" (A. Lajtha Eds.), vol 1, pp261-271, Plenum Press, New York, 1969.

47. M. Mulligan, M. C. Linder, The size of small molecular weight iron pools in rat tissues, *in* "The Biochemstry and Physiology of Iron" (P. Saltman, J. Hegenauer, Eds.), pp313-314, Elsevier North Holland, Inc. 1982.

48. C. Francois, J. Nguyen-Legros, G. Percheron, Topographical and cytological localization of iron in rat and monkey brains. *Brain Res* 215, 317-322 (1981).

49. J.M. Hill, R.C. Switzer, The regional distribution and cellular localization of iron in the rat brain. *Neuroscience* 11, 595-603 (1984).

50. J.R. Connor, S.L. Menzies, S.M. St. Martin, E.J. Mufson, Celluar distribution of transferrin, ferritin and iron in normal and aged human brains. *J Neurosci Res* 27, 595-611 (1990).

51. B.P. Drayer, Imaging of the aging brain, part I. normal findings. Radiology 166, 785-796 (1988).

52. G.K. Klintworth, Huntington's chorea–morphologic contribution of a century, *in* "Huntington's Chorea: 1872–1972" (A. Barbeau, T.N. Chase, G.W. Paulson, Eds.), pp360-361, Raven Press, New York, 1973.

53. C.K. Mathews, K.E. van Holde, "Biochemistry", The Benjamin/Cummings Publishing Company, Redwood City, 1990.

54. C. Gasparovic, N. A. Matwiyoff, The magnetic properties and water dynamics of the red blood cell: a study by proton-NMR lineshape analysis. *Magn. Reson. Med.* 26, 274-299 (1992).

55. J.M. Gomori, R.I. Grossman, C. Yu-Ip, and T. Asakura, NMR relaxation times of blood: dependence on field strength, oxidation state, and cell integrity. *J. Comput. Assist. Tomogr.* 11, 684-690 (1987).

56. P. Gillis, S. Peto, F. Moiny, J. Mispelter, C.A. Cuenod, Proton transverse nuclear magnetic relaxation in oxidized blood: a numerical approach. *Magn. Reson. Med.* 33, 93-100 (1995).

57. R.K. Gupta, A.S. Mildvan, Nuclear relaxation studies on human methemoglobin, *J Bio Chem* 250, 246-253 (1975).

58. R.G. Bryant, K. Marill, C. Blackmore, and C. Francis, Magnetic relaxation in blood and blood clots. *Magn. Reson. Med.* 13, 133-138 (1990).

59. N.A. Matwiyoff, C. Gasparovic, R. Mazurchuk, and G. Matwiyoff, The line shapes of the water proton resonances of red blood cells containing carbonyl hemoglobin, deoxyhemoglobin, and methemoglobin: implications for the interpretation of proton NMR at fields of 1.5 T and bellow. *Magn. Reson. Imaging* 8, 295-301 (1990).

60. N.A. Matwiyoff, C. Gasparovic, R. Mazurchuk, and G. Matwiyoff, On the origin of paramagnetic inhomogeneity effects in whole blood. *Magn. Reson. Med.* 20, 144-150 (1991).

61. R.A. Brooks, G.D. Chiro, and N. Patronas, MR imaging of cerebral hematomas at different field strengths: theory and applications. *J. Comput. Assist. Tomogr.* 13, 194-206 (1989).

62. P.T. Fox, M.E. Raichle, Focal physiological uncoupling of cerebral blood flow and oxidative metabolism during somatosensory stimulation in human subjects, *Proc Natl Acad Sci (USA)* 83, 1140-1144 (1986).

63. J. Frahm, K.D. Merboldt, W. Hanicke, A. Kleinschmidt, H. Boecker, Brai or vein oxygenation or flow? On signal physiology in functional MRI of human brain activation. *NMR Biomed* 7, 12-20 (1994).

64. E.M. Haacke, A. Hopkins, S. Lai, P. Buckely, L. Friedman, H.J. Meltzer, P. Hedera, R. Friedland, S. Klein, L. Thompson, D. Detterman, J. Tkach, J.S. Lewi, 2D and 3D high resolution gradient echo functional imaging of the brain: venous contributions to signal in motor cortex studies, *NMR Biomed* 7, 54-62 (1994).

65. J.H. Duyn, C.T. Moonen, G.H. Van Yperen, R.W. De Boer, P.R. Luyten, Inflow versus deoxyhemoglobin effects in BOLD functional MRI using gradient echoes at 1.5T, *NMR Biomed* 7, 83-88, (1994).

66. R.S. Menon, S. Ogawa, X. Hu, J.P. Strupp, P. Anderson, K. Ugurbil, BOLD based functional MRI at 4 Tesla includes a capillary bed contribution: echo-planar imaging correlates with previous optical imaging using intrinsic signals, *Magn Reson Med* 33, 453-459 (1995).

67. B.P. Drayer, C.R. Bird, J.A. Hodak, R... Flom, P.J. Keller, Limited flip angle MR imaging: Nonhemorrhagic applications (abstr). *Radiology* 165p, 39 (1987).

68. J.F. Norfray, J.R. Couch, R.J. Elbie, D.C. Good, B.V. Manyam, J.L. Patrick, Visualization of brain iron by mid-field MR. *AJNR* 9, 77-82 (1988).

69. A. Bizzi, R.A. Brooks, A. Brunetti, J.M. Hill, J.R. Alger, R.S. Miletich, T.L. Francavilla, G. Di Chiro, Role of iron and ferritin in MR imaging of the brain: a study in primates at different field strengths. *Radiology* 177, 59-65 (1990).

70. J.F. Schenck, O.M. Mueller, S.P. Souza, C.I. Dumoulin, M.A. Hussain, Iron-dependent contrast in NMR imaging of the human brain at 4.0 tesla, *in* "Proc., SMRM, 8th annual meeting, Amsterdan, 1989," p. 9.

71. B.P. Drayer, Basal ganglia: significance of signal hypointensity on T2-weighted MR images. *Radiology* 173, 311-312 (1989).

72. G. Bartzokis, M. Aravagiri, W.H. Oldendorf, J. Mintz, S.R. Marder, Field dependent transverse relaxation rate increase may be a specific measure of the tissue iron stores. *Magn Reson Med* 29, 459-464 (1993).

73. J. Vymazal, R.A. Brooks, O. Zak, C. McRill, C. Shen, G. Di Chiro, T1 and T2 of ferritin at different field strengths: effect on MRI. *Magn Reson Med* 27, 368-374 (1992).

74. S.H. Koenig, R.D. Brown III, J. F. Gibson, R. J. Ward and T. J. Peters, Relaxometry of ferritin solutions and the influence of the Fe^{3+} core ions. *Magn Reson Med* 3, 755-767 (1986).

75. D.J. Brooks, P. Luthert, D. Gadian, C.D. Marsden, Does signal attenuation on high-field T_2-weighted MRI of the brain reflect regional cerebral iron deposition? Observation on the relationship between regional cerebral water proton T_2 values and iron levels. *J Neurol Neurosurg Psychiatry* 52, 108-111 (1989).

76. J. Vymazal, R.A. Brooks, C. Baumgarner, V. Tran, D. Katz, J.W.M. Bulte, D. Urgosik, G. Di Chiro, Is there a quantitative relation between T2-shortening and brain iron concentration? in "Proc., SMRM, 12th annual meeting, New York, 1993," p. 1276.

77. N.J. Pelc, A. Ahimakawa, O. Boyko, A method for mapping of T2 prime and for improved T2 measurement, in "Proc. 7th SMRM, 1988", p746.

78. O.B. Boyko, N.J. Pelc, R.J. Herfkens, A. Shimakawa, P.C. Burger, Neuropathologic correlation of T2 prime mapping of normal brain iron, in "Proc. 8th SMRM, 1989", p739.

79. R.J. Ordidge, J.M. Gorell, J.C. Deniau, R.A. Knight, J.A. Helpern, Assessment of relative brain iron concentration using T_2-weighted and T_2*-weighted MRI at 3 T. *Magn Reson Med* 32, 335-341 (1994)

80. F.Q. Ye, P.S. Allen, Ferritin as a Susceptibility Agent, *in* "Proc., SMRM, 12th Annual Meeting, New York, 1993," p. 800.

81. C.S. Raine, Neurocellular anatomy, *in* "Basic Neurochemistry" (G.J. Siegel, R.W. Albers, B.W. Agranoff, R. Katzman, Eds.), p38, Little Brown, Boston, 1981.

82. G. Jankovic, E. Tolosa, (Eds.), "Parkinson's Disease and Movement Disorders," Williams & Wilkins, Baltimore, 1993.

83. W. C. Koller (Eds.), "Handbook of Parkinson's Disease", Marcel Dekker, Inc., New York, 1987.

84. D. Carroll, "Living with Parkinson's", HarperCollins Publishers, New York, 1992.

85. O. Sacks, "Awakenings", HarperPerennial, New York, 1990.

86. R.J. Marttila, Epidemiology, *in* "Handbook of Parkinson's Disease" (W. C. Koller, Eds.), p.35-50, Marcel Dekker, Inc., New York, 1987.

87. J. Jankovic, Pathophysiology and clinical assessment of motor symptoms in Parkinson's disease, *in* "Handbook of Parkinson's Disease" (W. C. Koller, Eds.), p.99-126, Marcel Dekker, Inc., New York, 1987.

88. E.C. Alvord, Jr, L.S. Forno, Pathology, *in* "Handbook of Parkinson's Disease" (W. C. Koller, Eds.), p.209-236, Marcel Dekker, Inc., New York, 1987.

89. G.F. Wooten, Neurochemistry, *in* "Handbook of Parkinson's Disease" (W. C. Koller, Eds.), p.237-251, Marcel Dekker, Inc., New York, 1987.

90. W.C. Koller, Classification of parkinsonism, *in* "Handbook of Parkinson's Disease" (W. C. Koller, Eds.), p.51-80, Marcel Dekker, Inc., New York, 1987.

91. C.W. Olanow, An introduction to the free radical hypotesis in Parkinson's disease. *Ann Neurol* 32, s2-s9 (1992).

92. P. Jenner, C.D. Marsden, MPTP-induced parkinsonism: a model of Parkinson's disease and its relevance to the disease process, *in* "Parkinson's Disease and Movement Disorders" (G. Jankovic, E. Tolosa, Eds.), p55-75, Williams & Wilkins, Baltimore, 1993.

93. D. Ben-Shachar, G. Eshel, P. Riederer, M. B. H. Youdim, Role of iron and iron chelation in dopaminergc-induced neurodegeneration: implication for Parkinson's disease. *Ann Neurol* 32, s105-s110 (1992).

94. K.M. Earle, Studies on Parkinson's disease including x-ray fluorescent spectroscopy of formalin fixed brain tissue. *J Neuropathol Exp Neurol* 27, 1-14 (1968).

95. E. Sofic, P. Riederer, H. Heinsen, H. Beckmann, G P. Reynolds, G. Hebenstreit, M.B.H. Youdim, Increased iron (III) and total iron content in post mortem substantia nigra of parkinsonian brain. *J Neural Transm.* 74, 199-205 (1988)

96. E. Sofic, W. Paulus, K. Jellinger, P. Riederer, M.B.H. Youdim, Selective increase of iron in substantia nifra zona compacta of parkinsonian brains. *J Neurochem* 56, 978-982 (1991).

97. D.T. Dexter, F.R. Wells, A. J. Lees, F. Agid, P. Jenner, C.D. Marsden, Increased nigral iron content and alterations in other metal ions occurring in brain in Parkinson's disease. *J Neurochem* 52, 1830-1836 (1989).

98. D.T. Dexter, A. Carayon, F. Javoy-Agid, Y. Agid, R.R. Wells, S.E. Daniel, A. J. Lees, P. Jenner, C. D. Marsden, Alterations in the levels of iron, ferritin, and other trace metals in Parkinson's disease and other neurodegenerative diseases affecting the basal ganglia. *Brain* 114, 1953-1975 (1991).

99. E.C. Hirsch, J.P. Brandel, P. Galle, F. Javoy-Agid, Y. Agid, Iron and aluminum increase in the substantia nigra of patients with Parkinson's disease: an x-ray microanalysis. *J Neurochem* 56, 446-451 (1991).

100. R.J. Uitti, A.H. Rajput, B. Rozdilsky, M. Bickis, T. Wollin, W.K. Yuen, Regional metal concentrations in Parkinson's disease, other chronic neurological diseases, and control brains. *Can J Neurol Sci* 16, 310-314 (1989).

101. M. Savoiardo, L. Strada, F. Girotti, L. D'Incerti, M. Sberna, P. Soliveri, L. Balzarini, MR imaging in progressive supranuclear palsy and Shy-Drager syndrome, *J Comput Assis Tomogr* 13, 555-560 (1989).

102. B. Drayer, P. Burger, B. Hurwitz, D. Dawson, J. Cain, Reduced signal intensity on MR images of thalamus and putamen in multiple sclerosis: increased iron content? *AJNR* 8, 413-419 (1987).

103. P. Martinez-Martin, Rating scales in Parkinson's disease, *in* "Parkinson's Disease and Movement Disorders" (G. Jankovic, E. Tolosa, Eds.), p281-292, Williams & Wilkins, Baltimore, 1993.

104. M. M. Hoehn, M. D. Yahr, Parkinsonism: onset, progression and mortality. *Neurology* 17, 427-442 (1967).

105. R.S. Schwab, A.C. England, Projection technique for evaluating surgery in Parkinon's disease, *in* "Third Symposium on Parkinson's Disease" (F. J. Gillingham, I. M. L. Donaldson, eds.), pp152-157, Livingstone, Edinburgh, 1969.

106 S. Fahn, R.L. Elton, Unified Parkison's disease rating scale, *in* "Recent Developments in Parkinson's Disease" (S. Fahn, R. L. Elton, eds.), vol 2, pp153-163, Macmillan, Florham Park, 1987.

CHAPTER 2[1]

Relaxation Enhancement of the Transverse Magnetization of Water Protons in Paramagnetic Suspensions of Red Blood Cells

2.1 Introduction

The enhancement of water proton relaxation that is brought about by the influence of paramagnetic centres has affected several aspects of magnetic resonance imaging (MRI). In addition to the power of exogenous contrast agents (1), the relaxational influence of naturally occurring paramagnetic centres (primarily iron in either deoxygenated hemoglobin or in structures such as ferritin) can also provide important biomedical information, e.g., functional MRI (2,3). The characteristics of the relaxation enhancement are sensitive to, amongst other things, the relative mobility and the closeness of approach of the paramagnetic centres and the water molecules. As a result, the enhancement cannot be represented by the same detailed model in all situations. In some situations, e.g., the heme iron in sub-acute hematoma, the paramagnetic centres are sequestered within a cellular membrane whose mobility is highly restricted. When paramagnetic centres are so confined the decay of the transverse magnetization of neighbouring water protons is, in principle, influenced by three field gradient sampling processes, namely, by their diffusional sampling of the local field gradients in the extracellular space, by their sampling of local gradients in the intracellular space and by transmembrane diffusion between "sites" of very different intra and extracellular local fields. A quantitative understanding of the relative significance of each of these three field sampling processes does not seem to have been fully resolved by previous work, and the emphasis has varied between favouring diffusion in either intracellular (4), extracellular

---

[1] A version of this chapter has been accepted for publication. F.Q. Ye, P.S. Allen, Relaxation enhancement of the transverse magnetization of water protons in paramagnetic suspensions of red blood cells. *Magn Reson Med* (1995).

(5,6), or both (7,8) gradient fields, through favouring transmembrane diffusion (9,10), to favouring a combination of all three under conditions of slow to intermediate exchange (11,12,13).

The purpose of the work reported in the present communication was to evaluate quantitatively, by means of a model experimental system and its theoretical analogue, (a) to what extent the relaxation enhancement arises from either single compartment diffusion in local field gradients or from passage between these compartments, and (b) to what extent the cell shape affects their relative significance. These goals are essentially the same as those of the very recent independent work of Gillis *et al.* (8), which we had the benefit of seeing prior to the revision of this manuscript. Notwithstanding the similarity of the salient features of the methodology differ significantly. For example, the present work models the experimental data using a simulation over many (~ 10^3) randomly distributed cells, whereas the results of Gillis *et al.* (8) are modelled using the intra and extracellular field maps produced for a single cell. To represent a complete suspension, Gillis *et al.* (8) evaluate the population average of the simulation results from independently modelled intra and extracellular spaces. We have attempted to incorporate transmembrane diffusion naturally into the water dynamics. In spite of these differences of approach, the ability of the models to predict the dependence of the transverse relaxation on the interecho time (or refocussing pulse interval), Δ_{180}, is remarkably similar and reasons for this are postulated. Where the outcome of present work differs from that of reference 8 is in its choice of experimental variable and, through that choice, in its perspective on the role of transmembrane diffusion.

As with much of the previous work in this area, the experimental model comprised magnetized, aqueous suspensions of red blood cells (RBC). Suspensions of red blood cells were chosen as an experimental model, first because they provide a close

representation of the situation which occurs in sub-acute hematoma, a condition of marked clinical interest (14,15,16), and secondly because they provide a simple, controllable model with which to test the mechanisms of the relaxation enhancement. The control in our case was exercised through both the cell shape (similar to reference 8) and the intra/extracellular susceptibility difference (different from reference 8). For the theoretical modelling, computer simulation was adopted rather than an analytical approach (17). This was done in order to deal more appropriately with the random and closely overlapping local field gradients in a sample of high hematocrit and also with the incorporation of transmembrane diffusion. As such, the modelling goes beyond earlier work (18,19) which confined its attention to samples containing only a small volume fraction of paramagnetic centres and which, by confining its attention to diffusion in extracellular field gradients, excluded transmembrane diffusion. A preliminary account of this work has already appeared (20).

2.2 Theory and Simulation

The decay of the transverse magnetization observed during a Carr-Purcell-Meiboom-Gill (CPMG) pulse sequence (21) can be quantitatively characterized by means of an apparent relaxation rate, R_{2app} ($=1/T_{2app}$). For water protons in an aqueous suspension of RBCs, R_{2app} is governed by a number of different mechanisms and, depending on the relative importance of these various mechanisms, the apparent relaxation rate is sometimes found to be a function of the sequence interecho time. For simplicity, the mechanisms can be broadly divided into those which arise from the diffusion of water molecules in short range, local field inhomogeneities (i.e., those which modulate the field over the scale of cellular dimensions), and those which do not. Assuming additive component rates, R_{2app} can be written as,

$$R_{2app} = R_2^o + \Delta R_2 \qquad [2.1]$$

where R_2^o represents the relaxation components which are independent of the short range local field inhomogeneities and where ΔR_2 characterizes the enhancement of this relaxation originating from diffusion in those local inhomogeneous fields. Since a close estimate of R_2^o is measurable in the cell lysate (7,9,10), ΔR_2 can be determined experimentally from R_2^o, R_{2app} and Eq. [2.1].

To develop a model for the transverse relaxation enhancement resulting from the diffusion of spins in the local field inhomogeneities and hence to calculate ΔR_2, certain assumptions need to be made about that field distribution and about the diffusion dynamics. First of all, the cells in the suspension are assumed to be distributed randomly in space and stationary on the time scale of the NMR experiment, although the fractional volume occupied by them is well defined by the hematocrit. Secondly, a magnetization difference, ΔM, is assumed between the cells and the extracellular fluid in the suspension. ΔM is a consequence both of the confinement of the paramagnetic centres by the cellular membrane and of the externally applied magnetic field, B_o. Thirdly, the water molecules are assumed to diffuse freely in either the extracellular or the intracellular spaces, with relative spin populations p_e and p_i, and with diffusion coefficients D_e and D_i, respectively. Finally, the water molecules are also assumed to diffuse across the RBC membrane, the transmembrane passage being characterized by a correlation time, τ, which is in turn, determined by the average life time, τ_i, of the spins in the intracellular space and by the relative spin populations (p_e and p_i).

Because we have chosen to consider a hematocrit of ~ 45 (similar to the physiological values for male and female, i.e., (47.0±5) and (42.0±5), respectively), there will be a large concentration of cells in solution and the local magnetic field at any point will be the sum of strongly overlapping fields from many of the randomly distributed cells. Because of this complexity, computer simulation of the field distribution and water

diffusion problems becomes the appropriate approach rather than pursuing an analytical solution. The actual simulation method used in this study, while similar in some respects to that used by Hardy (18) and by Fisel (19), is different in that because of the high hematocrit it incorporates a modelling of many overlapping dipolar fields and it also addresses the issue of transmembrane diffusion.

For example, for the simplest construct comprising a random environment of spherical cells of radius λ, the random environment was generated using a method similar to that of Metropolis (22). By means of this method, a face centered cubic lattice of $\sim 10^3$ cells, whose lattice constants were determined by the hematocrit and by λ, and which served as the starting point for the randomization process, ultimately gave rise to a random distribution of the cells which bore no relationship to the face centered cubic starting point. At any location within this randomized environment the local magnetic field could be calculated, as explained in section 2.5 (Appendix of Field Calculation), by summing the dipole fields, B_d, from each of the individual cells inside a large sphere (the first sphere of Lorentz) centered on the point in question and whose radius was $\sim(6\lambda)$ or greater. The contribution to the relaxation enhancement, ΔR_2, from cells outside this first sphere of Lorentz is negligibly small. To be able to accommodate proton spins diffusing near the edge of this randomized cellular distribution, the distribution itself was assumed to repeat on a much larger primitive cubic lattice. In this way the diffusion of a proton out of one face of the local environment is equivalent to its reappearance in the opposite face. The magnitude of the z component of the individual-cell dipole field, $B_d(\mathbf{r})$, at a distance, r, from the cell centre ($r>\lambda$) is given by

$$B_d(\mathbf{r}) = \mu_o \Delta M \cdot \left(\lambda^3 / r^3\right) \cdot \left(3\cos^2\theta - 1\right)/3, \qquad [2.2]$$

where θ is the polar angle between the displacement vector $\mathbf{r}$ and the magnetic field, $\mathbf{B_0}$. In general, for any shape of cell the effective (i.e., z component) local field experienced by

the j^{th} spin, $B^{(j)}(\mathbf{r}_k)$, at the time of its k^{th} diffusive jump to location $\mathbf{r}_k$ in the suspension, can be written as (see section 2.5)

$$B^{(j)}(\mathbf{r}_k) = \begin{cases} \sum_{Cells} B_d(\mathbf{r}_k) & \text{if } \mathbf{r}_k \text{ is extracellular} \quad [2.3a] \\ \sum_{Cells} B_d(\mathbf{r}_k) + \left(\tfrac{1}{3} - \alpha_c\right)\mu_o \Delta M & \text{if } \mathbf{r}_k \text{ is intracellular} \quad [2.3b] \end{cases}$$

where $\sum_{Cells} B_d(\mathbf{r}_k)$ represents the summation at location $\mathbf{r}_k$ of the dipole or dipole-like fields from the randomly distributed cells inside the first sphere of Lorentz. In Eq. [2.3b], α_c is a demagnetizing factor which is determined by the shape of the cell surface, and μ_o is the permeability of free space. When the cells are spherical Eq. [2.3b] reduces to the form of Eq. [2.3a] regardless of the location of $\mathbf{r}_k$, because the demagnetizing factor is 1/3 for a sphere.

To evaluate ΔR_2, the decay of the water proton CPMG echo amplitude was obtained by numerical integration of the total net transverse magnetization from a representative number of water proton spins, $N_s \sim 10^4$. The initial coordinates of these spins were randomly generated and distributed amongst the local environment of $\sim 10^3$ cells in such a way as to maintain a uniform density in each of the intra and extracellular spaces. The spins were then allowed to proceed along their Monte-Carlo-generated, random-walk paths through that heterogeneous local field environment. The incorporation of transmembrane diffusion into the model was undertaken in such a way as to maintain not only the population balance between intra and extra cellular spaces but also the mean life times of the water proton spins inside and outside the cell. To bring about the appropriate lifetimes, only a certain proportion of transmembrane diffusion paths were allowed. This allowance was implemented by adjusting the exit probability of a water molecule from a cell, P_{exit}, from that which would be calculated from the actual

membrane permeability values (24). The magnitude of these adjustments was determined by actively monitoring the lifetimes of the intracellular spins in the simulation model. Then, in order to maintain the extracellular lifetime and the population balance as well, the entrance probability, P_{enter}, was set by equating input and output fluxes according to,

$$P_{enter}\, D_e^{1/2}\, w_e = P_{exit}\, D_i^{1/2}\, w_i \qquad [2.4]$$

where w_e and w_i are the local water concentrations. (N.B. the local water concentrations, w_e and w_i, are not the same as the relative spin populations, p_e and p_i, introduced earlier and used in Eq. [2.8].)

The initial phase of each of the spins in the resonant rotating frame was set to zero at t = 0, immediately after the first 90° pulse of the CPMG sequence. The phase evolution of the j^{th} spin was approximated by assuming that incremental amounts, $\Delta\Phi_{jk}$, were accumulated over periods, δt, and under magnetic fields $B^{(0)}(\mathbf{r}_k)$ at successive locations $\mathbf{r}_k$, where

$$\Delta\Phi_{jk} = \gamma B^{(0)}(\mathbf{r}_k)\, \delta t \qquad [2.5]$$

and γ is the proton gyromagnetic ratio. Infinitely fast jumps between successive locations were also assumed. The time δt between jumps was chosen to be very much less than the smallest interecho time Δ_{180}, i.e. $\Delta_{180}/\delta t > 20$, and as such, gave rise to an r.m.s. step size, $(6D\delta t)^{1/2}$ which was, as with previous studies (19), <10% of the cell radius. The incremental random-walk steps were generated by a three dimensional gaussian-weighted random function of zero mean and a variance of $2D\delta t$.

If the 180° pulses in the CPMG sequence are assumed to produce an instantaneous phase reversal of the spins (the phases of the 180° pulses are shifted by $\pi/2$

from the excitation pulse), then the phase of the j^{th} spin at the time of the n^{th} echo may be obtained from the recursive relationship,

$$\Phi_j\left(n\Delta_{180}\right) = (-1)\Phi_j\left([n-1]\Delta_{180}\right) - \sum_{k=2(n-1)\xi}^{k=(2n-1)\xi}\gamma\cdot B^{(j)}(\mathbf{r}_k)\delta t + \sum_{k=(2n-1)\xi}^{k=2n\xi}\gamma\cdot B^{(j)}(\mathbf{r}_k)\delta t \qquad [2.6]$$

where $2\xi = \Delta_{180}/\delta t$. The negative signs for the first two terms reflect the fact that the n^{th} 180° pulse will reverse the phase already accumulated up to the time of the $(n-1)^{th}$ echo as well as that accumulated between the $(n-1)^{th}$ echo and itself. The total nuclear magnetization, m, at each echo could therefore be determined from

$$m = \left(1/N_s\right)\cdot\left[\left(\sum_{j=1}^{N_s}\cos\Phi_j\right)^2 + \left(\sum_{j=1}^{N_s}\sin\Phi_j\right)^2\right]^{1/2} \qquad [2.7]$$

Because the value of α_c for any but a spherical surface is either difficult to control experimentally or difficult to calculate, or both, we chose to test the simulation model of ΔR_2 for spherical cells, by means of both its interecho time dependence and its ΔM dependence. In this limit, the local field is everywhere governed by Eq. [2.3a], but the motional dynamics change at the cell boundary.

Using the following parameters, $D_e = 2\text{x}10^{-9}$ m^2/sec, $D_i = 5\text{x}10^{-10}$ m^2/sec (23), τ_i = 10 msec (24), and λ = 2.7 μm, the interecho time and ΔM dependence of the relaxation enhancement was obtained from Eqs. [2.2] to [2.7] by varying Δ_{180} in Eq. [2.6] and ΔM in Eq. [2.2]. The simulation was generally carried out for a total echo envelope of about 200 msec. The normalized decay curves were truncated at the echo amplitudes smaller than e^{-3} and fitted to a single exponential to determine the relaxation rate enhancement ΔR_2. To check if the decay of echo amplitude displayed any multi-exponential behaviour, a non-negative linear least square routine (25) was also employed. ΔM was incremented between 1 A/m and 10 A/m to span a range that encompassed the

value found for RBC containing deoxygenated hemoglobin in native plasma (~ 5 A/m) at 2.35 T (11).

When the cells are not spherical and the demagnetizing factor is not known, the additional relaxation enhancement can be alternatively modelled (26) by representing transmembrane diffusion as two-site exchange between intra and extracellular sites differing significantly in resonance frequency, provided the fast exchange conditions is approximated. Evidence for this situation has been reported from work at higher B_0 (11,13). An expression for the additional relaxation rate enhancement, ΔR_2^{ex}, as measured by means of a CPMG sequence, is given by (26,27),

$$\Delta R_2^{ex} = p_i\, p_e\, (\delta\omega)^2\, \tau\, [1 - (2\tau/\Delta_{180})\cdot\tanh(\Delta_{180}/2\tau)\,] \qquad [2.8]$$

where $\delta\omega$ represents the average resonance frequency difference between the intra and extracellular spins and p_i, p_e and τ are as previously defined. To verify the credibility of Eq. [2.8] in this situation, it was fitted to the interecho time dependence of an experimental ΔR_2^{ex}, determined from the ΔR_2 difference between spherical and biconcave RBC in suspensions having the same ΔM and hematocrit.

2.3 Experimental Methods

Samples of fresh canine blood containing a standard citrate-phosphate-dextrose anticoagulant (0.15%) were centrifuged to provide the RBCs. Two types of RBC suspensions were prepared in order to have samples with two shapes of RBC, each at a hematocrit of 45. For one type the RBC's were re-suspended directly in the original canine plasma. For the other, the RBC were first washed and then re-suspended in a hypotonic phosphate buffered saline (PBS) solution to provide quasi-spherical cell shape (28). The PBS was freshly made with 87 mM NaCl, 3 mM NaH_2PO_4 and its pH was adjusted to 7.3. The osmolarity of the PBS preparation was ~ 60% of that of

physiological isotonic saline. Small amounts of bovine serum albumin (1%) and dextrose (0.1%) were also added to the PBS. No evidence of RBC lysis appeared in any of the suspensions.

Because the relaxation enhancement depends on the magnitude of ΔM and is independent of whether the paramagnetic centres are located internally or externally to the cells, an alternative to deoxygenated intracellular hemoglobin (7,9,10) was used to bring about the magnetization difference, namely, fully oxygenated intracellular hemoglobin and extracellular DyDTPA. There were two reasons for this alternative. First, the stability of ΔM was greater, because it is much easier to maintain the hemoglobin in its fully oxygenated state than it is to control its deoxygenation level, and secondly, DyDTPA is similar to deoxygenated hemoglobin in that it is a strong susceptibility agent and has only a relatively small direct relaxation enhancement effect on the water proton. Accordingly aqueous solutions of various concentrations of DyDTPA were introduced to the extracellular fluid of samples of both types of suspension in such a way as to maintain both their hematocrit and osmolarity but to bring their extracellular DyDTPA concentration to a predefined value in the range 1-10 mM. In this way magnetization differences between the intra and extracellular environments were produced that spanned the range of 1-10 A/m at 2.35 T. A similar magnetization difference of ~ 5 A/m would arise between deoxygenated hemoglobin and native plasma at 2.35 T (11). To oxygenate the hemoglobin, air was bubbled through each sample before any relaxation measurements took place. The tendency of the RBC either to settle or to float depends on the composition of the extracellular fluid (29). No significant sedimentation in the suspension samples was observed over the measurement period of ~ 20 min.

Proton transverse relaxation decays were measured using CPMG sequences at a field strength of 2.35 T and at a room temperature of 21 ± 1 °C. To be sensitive to any

compartmentalization in the proton populations, relaxation rate determinations were made not from a single exponential fitting procedure but from a non-negative least squares routine (25,29). This gave rise to a smooth T_2 spectrum, from which the peak of the principal component (> 90% of the intensity) was designated as $T_{2app}(=1/R_{2app})$. Minor changes in the shape of this spectrum occurred either as Δ_{180} was varied or as the cells were lysed. For example, at very short Δ_{180} a weak, short T_2 component arose at <9 ms. Nevertheless such details and their changes were always very small compared to the principal component. Relaxation rate determinations were made first of the protons in a suspension to give R_{2app} of Eq. [2.1] and secondly, after 5 µl of Triton x-100 had been added to the suspension to lyse the RBC, to give R_2^o of Eq. [2.1]. Values of the relaxation enhancement, ΔR_2, were then determined from their difference. Measurements of ΔR_2 were taken at a series of Δ_{180} values between 1 and 32msec, incremented in ten steps, and for a series of values of ΔM for each type of suspension.

2.4 Results and Discussion

The dependence of the relaxation enhancement, ΔR_2, on the interecho time of a CPMG sequence, on the shape of the RBC, and on the value of ΔM are all clearly demonstrated in Figure 2.1. While the dependence of R_{2app} itself on the first two of these parameters (interecho time and RBC shape) has been previously reported for a similar system by Gillis *et al.* (8), those workers did not isolate experimentally and focus theoretically on the relaxation enhancement, ΔR_2, arising from the sequestration of paramagnetic centres by the cellular membranes. Curve A of Figure 2.1, from a sample devoid of paramagnetic centres, demonstrates the absence of this enhancement in samples where integral cellular membranes do not give rise to a magnetization difference between intra and extracellular environments. However, when the intact membranes do separate regions of different magnetization, an interecho time dependent enhancement is

clearly demonstrated by curve B for quasi-spherical RBC and by curve D for RBC of the natural, biconcave shape.

The enhancement arising from sequestration by spherical cell membranes was modelled by the simulation method described above and gives rise to curve C of Figure 2.1, using the physical parameters listed in the Theory Section and no other adjustable parameters. Curve C clearly reproduces the principal features of curve B, but the goodness of fit changes from one extreme (Δ_{180}= 1 ms) to the other (Δ_{180}=32 ms). One possible reason for any mismatch between the shapes of curves B and C, particularly at the longer interecho times, may well arise from a less than perfect spherical shape for the RBC in the hypotonic solution used (c.f. shape of curve D). The parameters of the model which affect the fit (for constant ΔM and hematocrit) are the diffusion constants. For example, in the limit that transmembrane diffusion is discarded and extracellular diffusion amongst point dipoles is assumed, then ΔR_2 increases by ~ 33% at Δ_{180}=32 ms to give an apparently better fit. However, the rise in ΔR_2 at short interecho time is also accelerated (30% greater at Δ_{180}=2 ms) thereby worsening the short time fit. Taking a population average of independent intra and extracellular results gives similar results to the complete simulation at long interecho times, but gives an enhancement that is ~ 10% less at short times.

A further test of the model in the spherical RBC case is its ability to reproduce the ΔM dependence. Figure 2.2 shows both the experimental data and the simulation results for the ΔM dependence at two interecho times, the agreement being better at the longer interecho time when the enhancement mechanism produces a proportionately greater effect. The relationship shown in Figure 2.2 is clearly non-linear and suggestions have been made (7,9) that the enhancement should be quadratic in ΔM. Figure 2.3 shows the results of a power law evaluation of the data, which gives rise to an exponent of 1.91 for

both of the simulated curves, but to exponents of 1.61 (Δ_{180}=2 ms) and 1.71 (Δ_{180}=12 ms) for the two experimental data sets. An exact quadratic dependence as previously suggested (7,9) cannot therefore be confirmed.

The impact of the surface shape, demonstrated by the difference between curves B and D in Figure 2.1, is thought to arise from its effect on the demagnetizing factor in Eq. [2.3b]. Although a simulation of the field within a non-spherical RBC was not performed here (as it was in reference 8), we found that the increase in ΔR_2 brought about by the change in shape could be very well modelled by Eq. [2.8] (26,27), applied to a spatially averaged transmembrane frequency shift (11,13) between the RBC and isotonic plasma. Figure 2.4 shows, as its data points, the difference between the data points of curves B and D of Figure 2.1, and as its fitted curve, Eq. [2.8] with two independent adjustable parameters, one (τ) to fit the shape and the other ($p_i p_e [\delta\omega]^2\tau$) to set the amplitude. The fit shown in Figure 2.4 arises from a transmembrane correlation time of 5.5 msec and a coefficient ($p_i p_e [\delta\omega]^2\tau$) = 22.1 s^{-1}. At a hematocrit of 45, the independent estimate of τ_i = 10 ms (24) would give rise to the very similar transmembrane correlation time of 6.4 ms, by means of the simple addition of inverse lifetimes for the extra and intracellular water (26). The amplitude coefficient produces a value of $(\delta\omega)^2$ which when written in a field independent form gives rise to $\delta\omega/\gamma B_0$ = 0.21 x 10^{-6}. Comparison with a similar experimental parameter of reference 8 would not be appropriate because in that reference, although a very similar relationship is used (27), the fit is not made to the isotonic to hypotonic changes in ΔR_2, but to R_{2app} itself. Retrospective processing of the reference 8 data would not be appropriate either because the hematocrit was not held constant in that work. Bearing in mind that Gillis *et al.* (8) also used a different paramagnetic agent, the only common factor between this work and that of Gillis *et al.* (8) appears to be the cell shape in isotonic solution. Using a susceptibility difference of 1.6 x 10^{-6} between oxygenated hemoglobin and 3 mM

DyDTPA, the present work suggests a change in demagnetizing factor of 0.13, if it is assumed that the difference between curves B and D of Figure 2.1 is indeed due solely to the difference between biconcave and truly spherical RBC. By comparison, the theoretical calculation presented in reference 8 provides a value of 0.121 for the difference in demagnetizing factor between native and spherical RBC. The agreement is therefore quite good and taken together with the very plausible fit prediction for τ, provides a case for an alternative interpretation of $\delta\omega$ to that presented in reference 8.

A notable feature of any comparison between the work presented here and that published by Gillis *et al.* (8) is the similarity in their respective abilities to fit the interecho time dependence of the transverse relaxation, in spite of the very different modelling, first of the field distribution and secondly of the water dynamics. That field mapping by means of Eq. [2.3] applied to a randomized array of ~ 10^3 RBC should give rise to a similar agreement with experimental data as does that obtained using the internal and external fields of a single isolated cell, probably reflects the fact that when the hematocrit is ~ 45 the two sources of field contribute similar amounts to the inhomogeneities through which the diffusing water molecules pass. That a weighted average of compartmentalized simulation results for the intracellular and extracellular spaces (8), provides a similar agreement to the Δ_{180} dependence as the unified approach to intra and extracellular probabilities presented here, probably reflects a fundamental similarity in the numerical phase summations into which the respective methods can be broken down. The differences between the Δ_{180} dependence predictions of these two numerical models are clearly insufficient to be resolved by the exactness of the currently available experimental data.

Notwithstanding the similarities outlined above and in contrast to several statements made in reference 8, we do however find that the shape dependent difference

in the interecho time dependent enhancement of the transverse relaxation does give rise to a transmembrane correlation time that is consistent with independent measurements (24) of the intracellular lifetime, τ_i. What is more, this same fit produces an estimate of the change in demagnetizing factor resulting from the change of shape that is in agreement with the theoretical estimates made in reference 8.

In conclusion, the data shown in Figure 2.1 confirm the significance in governing the enhancement of the relaxation efficiency, not only of the sequestration of paramagnetic centres, but also of the shape of the sequestering envelope. The degree of consistency between the experimental data and the predictions of the numerical model, for example in regard to the interecho time dependence, the ΔM dependence and the cell shape dependence, would normally give confidence in the validity of the model. However, the ability of a very different model (8) to provide a similar consistency with one aspect of the data, namely, the interecho time dependence, means that further experiments will be required to discriminate between the two.

2.5 Appendix of Field Calculation

To determine the effective (i.e., z component) magnetic field in a cell suspension we let χ_i and χ_e be the local volume magnetic susceptibilities of the intra and extracellular spaces in a suspension of identical cells. In an external magnetic field B_o, the average magnetization of the sample is then given by

$$M = [\, P_{vi}\, \chi_i + P_{ve}\, \chi_e \,]\, B_o/\mu_o, \qquad [A1]$$

where P_{vi} and P_{ve} are the fractional volumes of the two spaces (N.B. P_{vi} provides the same information as hematocrit does in the case of blood sample). If a sphere of Lorentz is drawn around a particular proton site, p, such that its radius is so large that the local field contributions at p from sources outside the sphere vary smoothly and can be

represented by fields resulting from magnetization currents on the boundary surface, then the magnetic field at p, B_p, can be written as

$$B_p = B_0 + (1/3 - \alpha_s)\,\mu_0 M + B_{L1}, \qquad [A2]$$

where the demagnetization factor α_s is determined by the surface shape of the sample (30,31) and where B_{L1} represents all sources of magnetism inside the sphere. Within this first sphere of Lorentz, the magnetization of each cell differs from that in the extracellular fluid by an amount ΔM,

$$\Delta M \approx [\,\chi_i - \chi_e\,]\, B_0/\mu_0. \qquad [A3]$$

A cell with excess magnetization, ΔM, relative to its extracellular fluid environment gives rise to a magnetic field $(1/3-\alpha_c)\mu_0\Delta M$ within the cell and to the dipole or dipole-like field, B_d, outside it, where α_c is again a geometric factor but now it is one determined by the shape of the cell. To evaluate B_{L1} a second, smaller, sphere of Lorentz is drawn around p, which is smaller than a cell but much larger than the paramagnetic particles. The field contributions to B_{L1} are then given by,

$$B_{L1} = \begin{cases} \sum_{Cells} B_d + B_{L2} & \text{if p is extracellular} \qquad [A4a] \\ \sum_{Cells} B_d + \left(\frac{1}{3}-\alpha_c\right)\mu_o\Delta M + B_{L2} & \text{if p is intracellular} \qquad [A4b] \end{cases}$$

where the summation $\sum_{Cells} B_d$ adds contributions at p from all cells within the first sphere of Lorentz, and B_{L2} is the field from paramagnetic ions inside the second sphere. Since water molecules are in constant thermal motion, the second sphere of Lorentz can be regarded as a sphere small enough that, on average, a water proton can diffuse through it many times on the NMR time scale. The advantage of this is that only the average field over the sphere $\langle B_{L2} \rangle$ is important for the resonant frequency shift calculation. Although microscopic fluctuations of fields within this sphere are capable of inducing both

longitudinal and transverse relaxation, their contribution to transverse relaxation is already included in the intrinsic relaxation rate, R_2^o, of Eq. [2.1] and is not regarded as part of the relaxation enhancement, ΔR_2. The local effective field at a water proton site, p, is then,

$$B_p = \begin{cases} B_o + \left(\frac{1}{3} - \alpha_s\right)\mu_o M + \sum_{Cells} B_d + \langle B_{L2}\rangle_e & \text{if p is extracellular} \quad [A5a] \\ B_o + \left(\frac{1}{3} - \alpha_s\right)\mu_o M + \sum_{Cells} B_d + \left(\frac{1}{3} - \alpha_c\right)\mu_o \Delta M + \langle B_{L2}\rangle_i & \text{if p is intracellular} \quad [A5a] \end{cases}$$

The first two terms in Eq. [A5a] and [A5b], which are dependent on the macroscopic aspects of the experiment, are not affected by lysing the cells and can therefore be dropped from the modelling of Δk_2. The contribution of the last term, $\langle B_{L2}\rangle$, to the water proton resonant frequency shift is likely to be small in comparison with $\sum_{Cells} B_d$ for hemoglobin and DyDTPA solutions because of the limited direct interaction that a typical water molecules will have with a paramagnetic ion in the smaller second sphere of Lorentz. In the approximate forms of Eq. [A5a] and [A5b] which are presented as Eq. [2.3a] and [2.3b] in the text the contribution of $\langle B_{L2}\rangle$ is neglected.

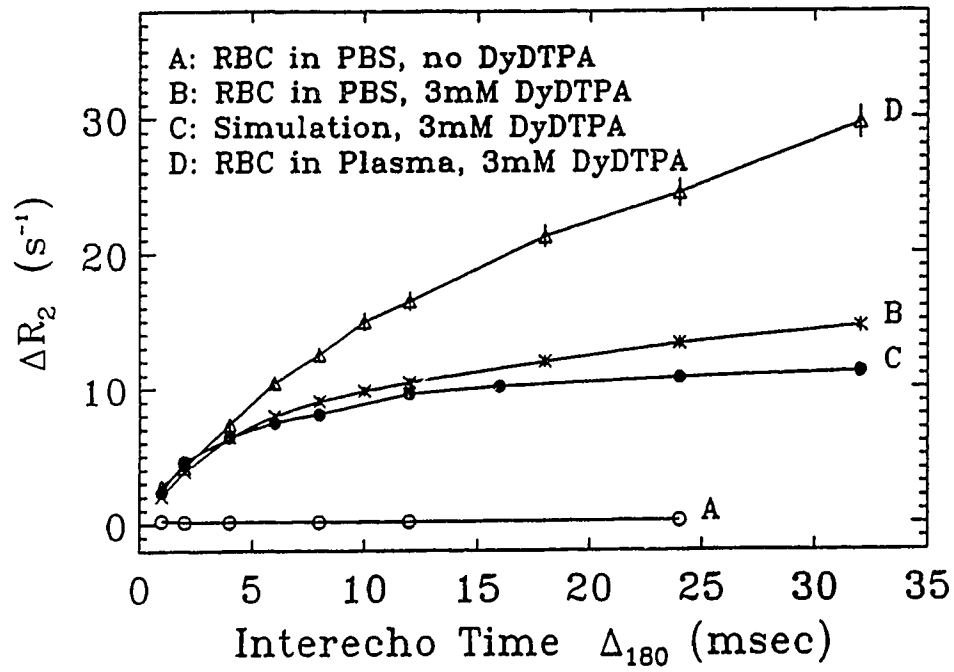

Figure 2.1. The relaxation enhancement, ΔR_2, plotted as a function of interecho time, Δ_{180}, for three types of red blood cell suspension and for one computer simulation. Curve **A** represents measurements from a suspension of RBC in hypotonic PBS containing no paramagnetic agent. Curve **B** illustrates measurements from suspensions of RBC in hypotonic PBC containing 3 mM of extracellular DyDTPA. Curve **C** is a computer simulation for suspensions of spherical cells containing 3 mM of extracellular DyDTPA. Curve **D** represents measurements from suspensions of RBC in plasma containing 3 mM of extracellular DyDTPA. The hematocrit of all the samples was 45 and the hemoglobin was fully oxygenated so as not to be paramagnetic. The error bars on the curves B and D represent one standard deviation (N=6 for each curve).

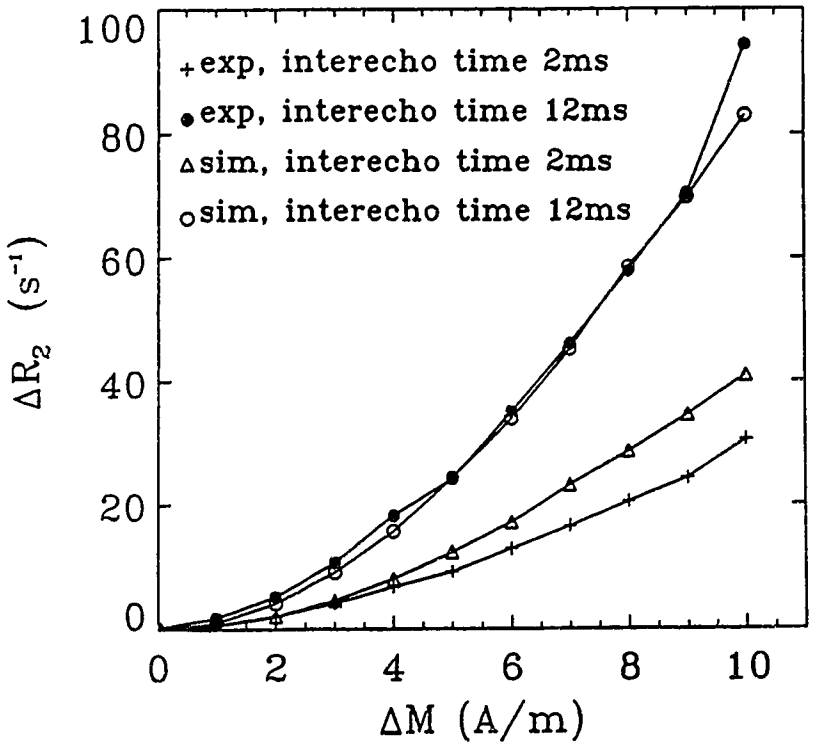

Figure 2.2. A diagram illustrating the change in relaxation enhancement, ΔR_2, as a function of the magnetization difference, ΔM, between intra and extracellular spaces. All four curves represent data on suspensions of RBC in hypotonic PBS into which DyDTPA has been introduced. The curves can be grouped into two pairs, each pair corresponding to a different value of Δ_{180} (2 ms and 12 ms respectively). Within a pair one curve corresponds to the computer simulation and the other to experimental data.

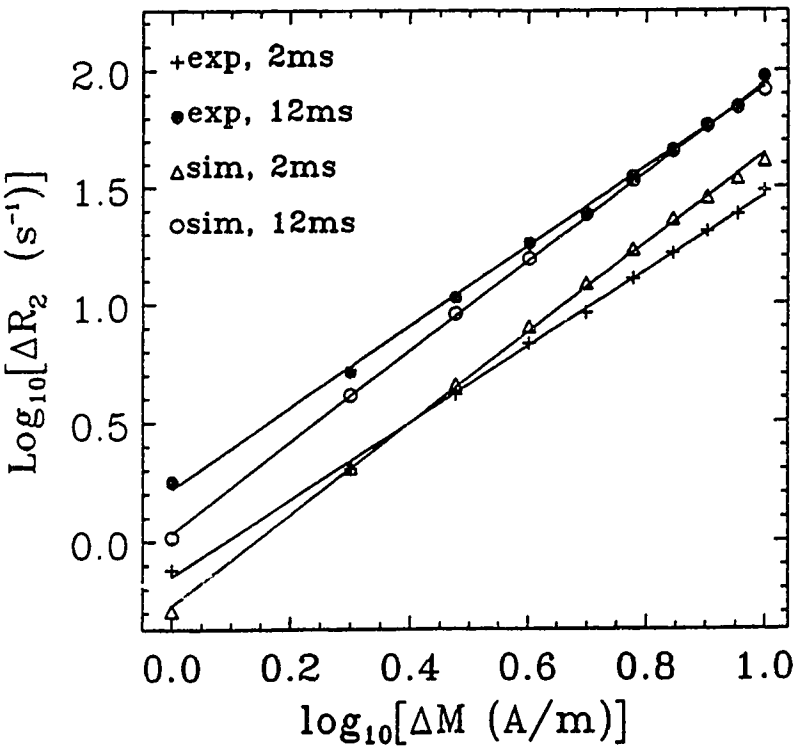

Figure 2.3. The power law representation of the data of Figure 2.2. These data give rise to an exponent of 1.9 for both of the simulation curves, but to exponent values of 1.6 and 1.7, respectively, for the two experimental data sets with interecho times of 2 ms and 12 ms.

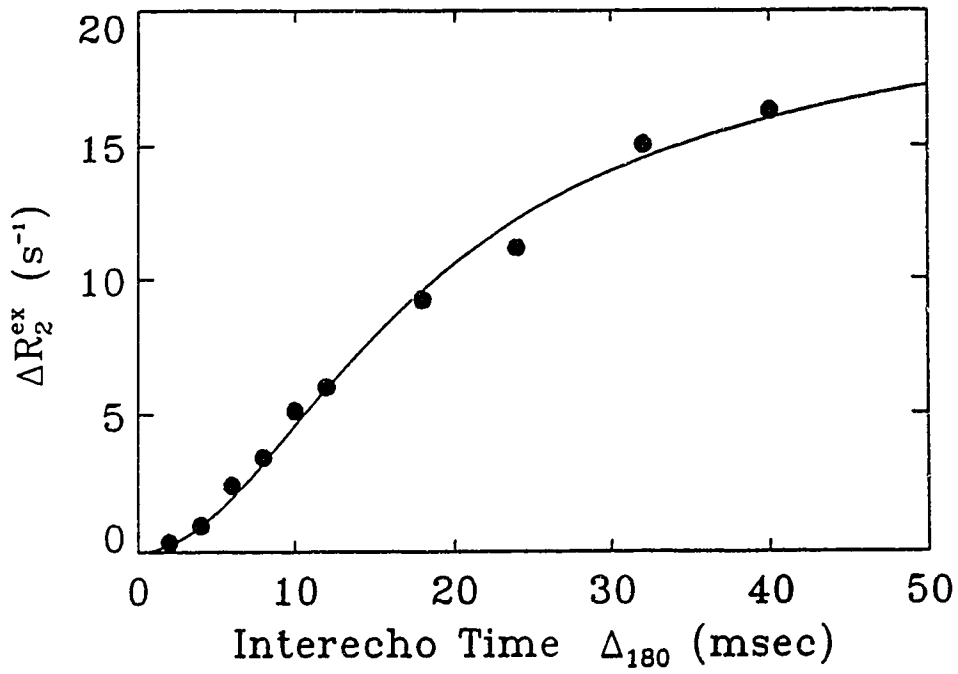

Figure 2.4. An illustration of the effect of a change in cell shape on the relaxation enhancement, ΔR_2^{ex}, brought about by transmembrane diffusion, as a function of interecho time, Δ_{180}. The experimental data points were obtained by subtracting the data of curve B from that of curve D in Figure 2.1. The solid curve is a fit of these data to Eq. [2.8]. The curve fitting gives rise to a correlation time, τ, for the transmembrane diffusion of 5.5 ms, which is in good agreement with the estimate of 6.4 ms obtained from the independent measurements (24) of average intracellular lifetimes.

2.6 References

1. J.C. Gore, R.P. Kennan and J. Zhong, *in* "The Physics of MRI, Proc. AAPM Summer School, 1992, Banff," (M.J. Bronskill and P. Sprawls, Eds.), p478-506, American Institute of Physics, Woodbury, NY, 1993.

2. S. Ogawa, D.W. Tank, R.S. Menon, J.M. Ellerman, S. Kim, H. Merkle, K. Ugurbil, Intrinsic signal change accompanying sensory stimulation: Functional brain mapping with magnetic resonance imaging, *Proc. Natl. Acad. Sci. USA* **89**, 5951-5955 (1992).

3. K.K. Kwong, J.W. Belliveau, D.A. Chesler, I.E. Goldberg, R.M. Weisskoff, B.P. Poncelet, D.N. Kennedy, B.E. Hoppel, M.S. Cohen, R. Turner, H. Cheng, T.J. Brady, B.R. Rosen, Dynamic magnetic resonance imaging of human brain activity during primary sensory simulation, *Proc. Natl. Acad. Sci. USA* **89**, 5675-5679 (1992).

4. P. Gillis and S.H. Koenig, Transverse relaxation of solvent protons induced by magnetized spheres: Application to ferritin erythrocytes and magnetite, *Magn. Reson. Med.* **5**, 323-345 (1987).

5. R.A. Brooks, A. Brunetti, J.R. Alger, and G.D. Chiro, On the origin of paramagnetic inhomogeneity effects in blood, *Magn. Reson. Med.* **12**, 241-248 (1989).

6. S. Peto, F. Moiny, P. Gillis, Intra- and extracellular contributions to the transverse relaxation of water protons in deoxygenated blood, in "Proc., SMRM, 11th Annual Meeting, Berlin, 1992," p. 1342.

7. K.R. Thulborn, J.C. Waterton, P.M. Matthews, and G.K. Radda, Oxygenation dependence of the transvers relaxation time of water protons in whole blood at high field, *Biochem. Biophys. Acta* **714**, 265-270 (1982).

8. P. Gillis, S. Peto, F. Moiny, J. Mispelter, C.A. Cuenod, Proton transverse nuclear magnetic relaxation in oxidized blood: a numerical approach, *Magn. Reson. Med.* **33**, 93-100 (1995).

9. J.M. Gomori, R.I. Grossman, C. Yu-Ip, and T. Asakura, NMR relaxation times of blood: dependence on field strength, oxidation state, and cell integrity, *J. Comput. Assist. Tomogr.* **11**, 684-690 (1987).

10. R.G. Bryant, K. Marill, C. Blackmore, and C. Francis, Magnetic relaxation in blood and blood clots, *Magn. Reson. Med.* **13**, 133-138 (1990).

11. N.A. Matwiyoff, C. Gasparovic, R. Mazurchuk, and G. Matwiyoff, The line shapes of the water proton resonances of red blood cells containing carbonyl hemoglobin, deoxyhemoglobin, and methemoglobin: implications for the interpretation of proton MRI at fields of 1.5 T and bellow, *Magn. Reson. Imaging* **8**, 295-301 (1990).

12. N.A. Matwiyoff, C. Gasparovic, R. Mazurchuk, and G. Matwiyoff, On the origin of paramagnetic inhomogeneity effects in whole blood, *Magn. Reson. Med.* **20**, 144-150 (1991).

13. C. Gasparovic, N.A. Matwiyoff, The magnetic properties and water dynamics of the red blood cell: a study by proton-NMR lineshape analysis, *Magn. Reson. Med.* **26**, 274-299 (1992).

14. R.A. Brooks, G.D. Chiro, and N. Patronas, MR imaging of cerebral hematomas at different field strengths: theory and applications, *J. Comput. Assist. Tomogr.* **13**, 194-206 (1989).

15. K. Weingarten, R.D. Zimmerman, P.T. Cahill, and M.D.F. Deck, Detection of acute intracerebral hemorrhage on MR imaging: ineffectiveness of prolonged interecho interval pulse sequences, *AJNR* **12**, 475-479 (1991).

16. K.M. Jones, R.V. Mulkern, M.T. Mantello, P.S. Melki, S.S. Ahn, P.D. Barnes, and F.A. Jolesz, Brain hemorrhage: ev luation with fast spin-echo and conventional dual spin-echo images, *Radiology* **182**, 53-58 (1992).

17. S. Majumdar and J.C. Gore, Studies of diffusion in random fields produced by variations in susceptibility, *J. Magn. Reson.* **78**, 41-55 (1988).

18. P. Hardy and R.M. Henkelman, Transverse relaxation rate enhancement caused by magnetic particulates, *Magn. Reson. Imaging* **7**, 265-275 (1989).

19. C.R. Fisel, J.L. Ackerman, R.B. Buxton, L. Garrido, J.W. Belliveau, B.R. Rosen, and T. Brady, MR contrast due to microscopically heterogeneous magnetic susceptibility: numerical simulations and applications to cerebral physiology, *Magn. Reson. Med.* **17**, 336-347 (1991).

20. F.Q. Ye and P.S. Allen, The paramagnetic-susceptibility-enhanced water proton transverse relaxation in cell suspensions, in "Proc. SMRM, 12th Annual Meeting, New York, 1993," p. 802.

21. S. Meiboom, D. Gill, Modified spin-echo method for measuring nuclear relaxation times, *Rev. Sci. Instum.* **29**, 688-693 (1958).

22. N. Metropolis, A.W. Rosenbluth, M.N. Rosenbluth, and A.H. Teller, Equation of state calculations by fast computing machines, *J. Chem. Phys.* **21**, 1087-1092 (1953).

23. R.L. Cooper, D.B. Chang, A.C. Young, C.J. Martin, B. Ancker-Johnson, Restricted diffusion in biophysical systems, *Biophys. J.* **14**, 161-177 (1974).

24. M.D. Herbst and J.H. Goldstein, A review of water diffusion measurement by NMR in human RBC, *Am. J. Physiol.* **256**, c1097-1104 (1989).

25. K.P. Whitall, A.L. MacKay, Quantitative interpretation of NMR relaxation data, *J. Magn. Reson.* **86**, 134-139 (1989).

26. A. Allerhand, H.S. Gutowsky, Spin-echo NMR studies of chemical exchange. I. Some general aspects, *J. Chem. Phys.* **41**, 2115-2126 (1964).

27. Z. Luz and S. Meiboom, NMR study of the protolysis of trimethylammonium ion in aqueous solution--order of the reaction with respect to solvent, *J. Chem. Phys.* **39**, 366-370 (1963).

28. E. Ponder, "Hemolysis and related phenomena," J. & A. Churchill Ltd., London, 1948.

29. R.S. Menon, M. Rusinko and P.S. Allen, Multiexponential proton relaxation in model cellular systems, *Magn. Reson. Med.* **20**, 196-213 (1991).

30. E.M. Pugh, "Principles of Electricity and Magnetism", P304, Addison-Wesley Publisher Co., Reading, Mass., 1970.

31. R.J. Elliott, A.F. Gibson, "An Introduction to Solid State Physics and its Applications", pp439-440, The Macmillan Press Ltd., London, 1974.

CHAPTER 3[1]

Estimation of the Iron Concentration in Excised Grey Matter by Means of Proton Relaxation Measurements

3.1 Introduction

Enhanced, but localized brain iron deposition is associated with several neuro-degenerative disorders, e.g., Parkinson's disease (1-3), Huntington's disease (4), progressive supranuclear palsy (5) and multi-system atrophy (5). Its role in the etiology of these disorders is unclear, in part because experimental techniques to measure brain iron in-vivo and so establish definitive correlations have not been available. The NMR relaxation of water protons in the neighbourhood of iron deposits may have the potential to provide such a means of brain iron quantification, even though the T_2-weighted contrast in magnetic resonance imaging (MRI), that has been known for a considerable time (6-9) to follow the tomographic pattern of natural accumulations of iron, has not led to quantitative measurements. A major drawback has been the difficulty in demonstrating the experimental variable that is most closely correlated with brain iron, which has in turn been hindered by uncertainty about the relative importance of the various mechanisms giving rise to the enhanced relaxation phenomenon (4,10-17).

The largest single fraction of brain iron is stored in ferritin (18), and the strong transverse relaxation effect of the iron-core of ferritin in aqueous solution was demonstrated some time ago by Koenig *et al.* (19). However, subsequent measurements of the relaxation time of water protons in excised brain tissue (4,10) showed no significant correlation with either iron or ferritin concentration, thereby suggesting that

---

[1] A version of this chapter has been submitted for publication. F.Q. Ye, W.R.W. Martin, P.S. Allen, Estimation of the iron concentration in excised grey matter by means of proton relaxation measurements. *Magn Reson Med* (1995).

factors other than iron and/or ferritin played a significant role in determining the water proton transverse relaxation time and its structural variations.

Notwithstanding this lack of success with the observable relaxation time itself as the experimental variable, recent studies have proposed three other measurable characteristics of water proton transverse relaxation that could act as specific quantifiers of the iron concentration. The first of these is the field strength dependence (14-16) of the relaxation rate. It was found that the transverse relaxation rate increased linearly with increasing applied magnetic field in ferritin solutions (14). The slope of the experimental curve of this field strength dependence also correlated fairly well in excised brain tissue with the iron concentration (15). In the second technique (20), in order to expose that part of the transverse signal decay due to the local iron alone, the signal loss due to global field inhomogeneities was removed by means of a protocol involving precisely controlled slice refocussing gradients and the recombination of a series of images. Although this technique involves an increase in experimental duration, it does enable the generation of images from which an iron related relaxation rate may be obtained. The third potential quantifier is the interecho time dependence of the apparent proton transverse relaxation rate, R_{2app} (= $1/T_{2app}$), which has been shown to increase with increasing interecho time in samples where ferritin is heterogeneously distributed in cell suspensions (21). This interecho time dependence has also been used to monitor age related variations in brain iron in-vivo (17). Of the three techniques, the first one undoubtedly requires a significant additional investment in hardware together with the time commitment of two examinations. The fastest method is that tested here, namely the third technique. However, the sensitivity of this method relative to that of Ordidge *et al.* (20) has not been determined. While the data presented in reference 20 benefited from a field strength of 3 T, those presented here were obtained at 2.35 T. Moreover, the viability of the third technique has only been tested in-vivo at 1.5 T (17). Despite the application of these

techniques, the quantitative validation of neither has been reported in tissue. The purpose of this communication is to demonstrate with excised grey matter tissue, the empirical relationship between the interecho time dependence of R_{2app} and the tissue iron concentration obtained independently from atomic absorption spectrometry.

3.2 Methodology

Twenty five frozen, unfixed samples of brain tissue were transferred to the University of Alberta on dry ice from the National Neurological Research Specimen Bank, VAMC, Los Angeles. The samples were obtained postmortem from five male donors aged 53, 55, 58, 64, and 68 years. Four donors were classified as normal controls and the fifth had lung cancer. The twenty-five samples included five from the globus pallidus (GP), five from the putamen (PM), six from the caudate nucleus (CD), five from the thalamus (TH), two from the frontal cortex (fCX), and two from the occipital cortex (oCX). The samples were maintained at -78° C until the day of their NMR measurement when, on ice, each was sectioned in order to fit into a 5 mm diameter NMR tube which was sealed airtight until the final atomic absorption spectrometry took place. During this sectioning care was taken to minimize damage to the tissue integrity and both visible white matter and blood spots were removed. The NMR samples averaged a wet weight of ~ 71 mg each. Samples were thawed to room temperature prior to the NMR measurements, but refrozen and maintained at -18° C until submitted for iron analysis, at which time they were wet weighed, dried, reweighed and analyzed for iron using a Perkin Elmer Zeeman 5000 automated flame atomic absorption spectrophotometer.

The proton transverse relaxation decay was measured at a room temperature of 21 ± 1 °C for each of the samples at 2.35 T using a Curr-Purcell-Meiboom-Gill (CPMG) sequence (22). The interecho time interval, Δ_{180}, was incremented from 2 to 60 msec in

the same seven steps for all of the samples, but for eight of the twenty-five samples seven additional interleaving steps were also employed. The number of echoes at each value of interecho time, e.g., 1536 echoes for Δ_{180} = 2 ms, was adjusted to maintain a total acquisition time of ~ 3 s. Because white matter water proton transverse relaxation

has been shown to have more than one exponential component (23), a non-negative linear least squares (NNLS) analysis (24) was adopted to safeguard against any multiple component artifact affecting the transverse decay time measurements. Magnetization decay curves were truncated at exp(-5) times the first echo amplitude prior to application of the NNLS routine. From the smooth T_2 spectrum that was provided by the NNLS routine, the mean T_2 of the principal component (>90% of the intensity) was obtained to represent T_{2app} for tissue water protons. Minor changes in the shape of this T_2 spectrum occurred in some of the samples as Δ_{180} was changed. For example, a very short T_2 component (a few msec, probably from lipid protons) appeared in some samples at very short Δ_{180}. Nevertheless such details and their changes were always very small compared to the principal component and were excluded from the analysis.

3.3 Results and Data Analysis

Empirically, the increase in R_{2app} with increasing interecho time, Δ_{180}, was found to be similar in form to a $y = log\ x$ dependence. It is therefore illustrated in Figure 3.1 as a semi-logarithmic relationship. By means of the dimensionless variables (R_{2app}/ρ) and (Δ_{180}/τ), where ρ and τ are rate and time constants, respectively, $(R_{2app}/\rho) = \log_{10}(\Delta_{180}/\tau)$ can be written as

$$R_{2app} = \varepsilon + \rho \log_{10} \Delta_{180}, \qquad [3.1]$$

where $\varepsilon = \rho \log_{10} (1/\tau)$, and where ε and ρ can be used as empirical fitting parameters in a regression analysis. The linear regression curves in the illustrative semi-log plot of

Figure 3.1 are for four samples from a single normal control. Repeating the procedure for all donors, the regression coefficient, ρ, was determined to be significantly non-zero ($p < 0.01$) in data from 23 out of the total 25 samples, with a coefficient of determination, r^2, ranging from 0.74 to 0.99. The two exceptions were both cortical samples of low iron concentration.

The strength of the linear association between the iron concentration and the enhancement of the transverse relaxation of the water protons was evaluated for several measures of that enhancement, using correlation tests in which those measures were respectively, (a) the fitting parameter ρ, (b) the rate difference δR_{2app}, over the interecho time decade 6 ms to 60 ms, (N.B. according to Eq. [3.1], this particular rate difference, δR_{2app}, is equivalent to a two-point-fitting estimation of ρ.) and (c) R_{2app} itself at the limiting interecho times of 2 ms and 60 ms. The relaxation measures were also tested with regard to their correlation with the percentage of dry material in the tissue. The results are summarized in Table 3.1. From the values of ρ and ε determined for each of the grey matter samples, two structure-group parameters were calculated, namely, the mean values of ρ and a value of R_{2app} at $\Delta_{180} = 2$ ms, for each of the five brain structures. These group mean values together with that of iron concentration are listed in Table 3.2. A graphic presentation of part of the data is shown in Figure 3.2. It illustrates first, the separability of various grey matter structures on the basis of the interecho time dependence, ρ, of their water proton transverse relaxation, and, secondly, the correlation between ρ and the atomic absorption spectrometer measurement of tissue iron.

3.4 Discussion

The measurement of a single water proton transverse relaxation rate has been shown previously to correlate rather poorly with the iron content of the tissue in brain (4,10). The principal reason for this seems to be the dominating influence of relaxation

mechanisms that do not exploit the iron, but depend instead on the motional modulation of the various dipole-dipole interactions between water protons and the protons of the tissue matrix or on compartment-boundary susceptibility differences. The efficiency of such non-paramagnetic mechanisms is often found to correlate with the relative proportion of dry material in the tissue. The additive effect of naturally occurring iron may well be masked by the biological variability of the dominating mechanisms in correlations involving a single relaxation rate measurement. Separating the iron contributions to relaxation from those due to other mechanisms is therefore, not only the goal addressed by the method proposed here, but also those proposed by others (15,16,20).

The influence of iron on the transverse relaxation of water protons depends quite critically on the nature of the magnetic interaction between them, which in turn is governed by the form in which the iron appears. For example, the accumulation and sequestration of iron, largely in the form of ferritin, in glial cells (25) gives rise to susceptibility hot spots, which, in the presence of a large magnetic field, produce a heterogeneous field distribution over distances of the order of a few tens of microns. This heterogeneity is of such a scale as to be sampled by diffusing water molecules ($D \sim 10^{-9}$ m^2 s^{-1}) on the time scale of a CPMG interecho time (from ms to several tens of ms), thereby producing an irreversible dephasing that is Δ_{180} dependent. Such a Δ_{180} dependence is not normally observed in tissue where the mechanisms of transverse decay are nuclear dipole-dipole or diamagnetic susceptibility differences. That dependence is however, clearly demonstrated by the results presented here from brain structures in which iron is known to accumulate. The variation in the Δ_{180} dependence between different brain structures is also demonstrated in these data. In contrast, the iron core of an individual ferritin molecule, which has itself been shown to be an effective relaxation enhancer of water in regions containing soluble ferritin (14,19), is three orders of

magnitude less in scale than a glial cell and one would not therefore expect such enhancement to be Δ_{180} dependent. The glial accumulation of iron could, in addition, also be a potential source of the magnetic field strength dependence of transverse relaxation observed by others (16) because the local field inhomogeneity will be field dependent.

Although ferritin is likely the largest single component of brain iron (about one-third over the whole brain) (18), it is not the exclusive component and, moreover, the mechanisms described above are not thought to be the only iron contributions to water proton relaxation even in those structures where ferritin accumulates. Some iron is undoubtedly accessible to water, possibly including the surface iron of ferritin (15,19), and may interact with water through the hyperfine spin-dipole interaction. Although such a mechanism could be very effective for relaxing neighbouring water protons, it is not expected that this mechanism would be either field dependent or dependent on Δ_{180}. Neither is it expected that the proportion of affected water molecules would be very high and so direct interaction with water accessible iron can be considered as part of the Δ_{180} independent background.

From the statistical analysis (Table 3.1), it is seen that both the fitting parameter, ρ, and the relaxation rate difference, δR_{2app}, each of which measures the enhancement of relaxation as the diffusion length is extended, correlate well with iron concentration but poorly with the proportion of dry matter in the tissue. These measures are therefore thought to be the most selectively sensitive to the tissue iron. The single long interecho time measurement, R_{2app} (60 ms) also correlates well with iron concentration. However, it shows a stronger correlation with the proportion of dry matter than either ρ or δR_{2app}, and as a result appears more prone to the influence of mechanisms other than iron. Nevertheless, in contrast to the suggestions of Chen *et al.* (4), a long interecho time certainly seems to be the preferred choice to optimize iron sensitivity in those MRI

sequences that serve only to make regions of high iron concentration visible through their hypointensity. The single short interecho time measurement, R_{2app} (2 ms), shows the poorest correlation with iron concentration, but strongest (though not impressively so) with the proportion of dry matter, and as such is thought to provide the least reliable measure of tissue iron. This trend was not unexpected since in 2 ms the ability of water molecules to sample field inhomogeneities due to iron centres is quite restricted.

Because of biological variability, the clinical value of ρ, or δR_{2app}, will possibly be marginal at 1.5 T. Nevertheless, since the magnitude of the pathologic increase in iron (4) can be comparable to, or even a factor of two or three in excess, of the structure-dependent differences of normal brain shown in Figure 2, the interecho time dependence of R_{2app} should provide a discrimination that is clinically valuable at higher field strengths (e.g. 3 T) where the magnitude of the effect is that much greater.

Table 3.1.

The correlation (n= 25) between the various experimental measures of the transverse relaxation of water protons and (i) the iron concentration and (ii) the proportion of dry matter in the tissue .

	ρ	δR_{2app}	R_{2app} (60 ms)	R_{2app} (2 ms)
Iron concentration in μmol per gram wet tissue	r = 0.78 p = 0.0001*	r = 0.81 p = 0.0001*	r = 0.81 p = 0.0001*	r = 0.66 p = 0.0003*
Percentage of dry matter	r = 0.25 p = 0.23ns	r = 0.34 p = 0.098ns	r = 0.52 p = 0.007*	r = 0.56 p = 0.004*

*: significant at 99% confidence level.

ns: not significant at 99% confidence level.

Table 3.2.

The structure-group mean values for the iron concentration, the fitting parameter ρ, and the shortest interecho time R_{2app} calculated from the fitting parameters ρ and ε. All values are (mean ± std. dev.).

Tissue	Iron Concentration (μmol Fe/g wet weight)	ρ (s^{-1})	Calculated R_{2app} at Δ_{180} = 2 ms (s^{-1})
Globus Pallidus (n=5)	3.5 ± 1.2	3.0 ± 1.5	18.5 ± 2.2
Putamen (n=5)	2.0 ± 1.2	2.2 ± 0.8	14.2 ± 2.3
Caudate (n=6)	1.0 ± 0.6	1.6 ± 0.7	10.8 ± 1.4
Thalamus (n=5)	1.0 ± 0.8	1.3 ± 1.1	15.7 ± 1.5
Cortex# (n=4)	0.6 ± 0.3	0.8 ± 0.4	10.2 ± 0.9

includes two frontal cortex and two occipital cortex samples.

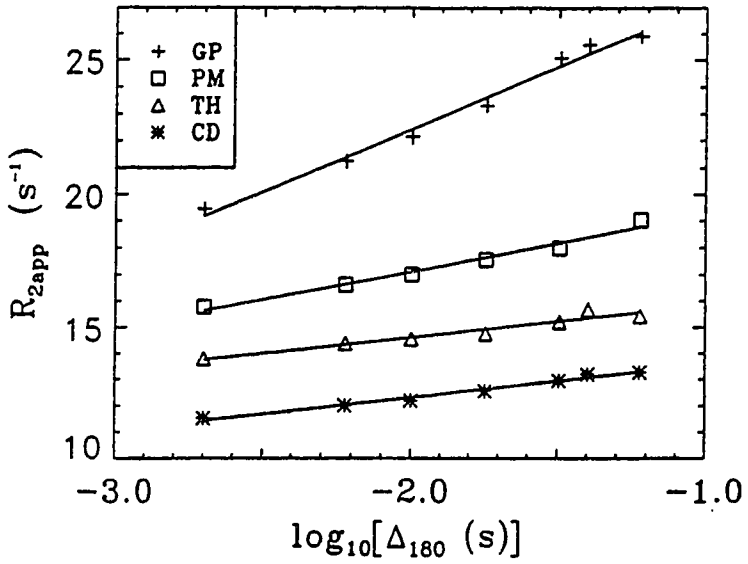

Figure 3.1. Typical regression curves for the interecho time (Δ_{180}) dependence of the apparent transverse relaxation rate, R_{2app}, determined in four excised brain samples from a 58 year old normal donor. The coefficients of determination for the four samples are equal or greater than 0.96.

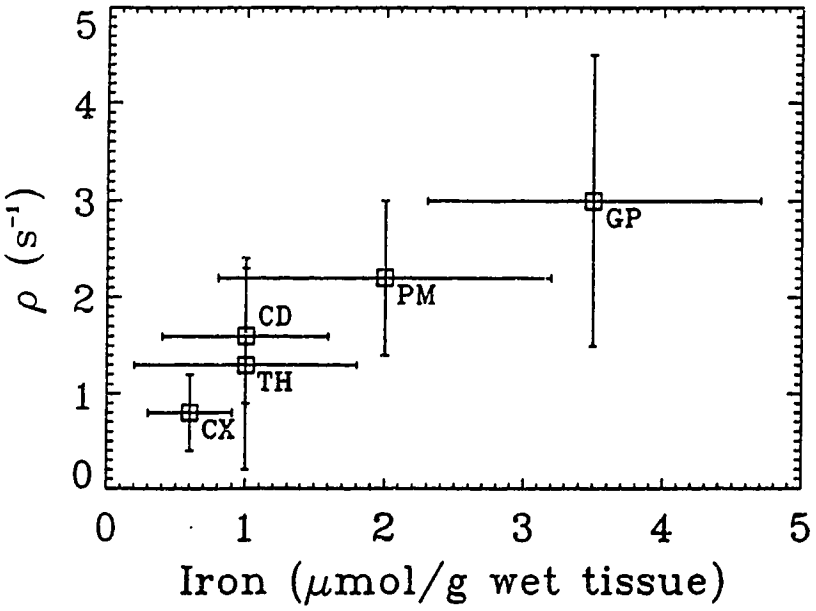

Figure 3.2. An illustration of first, the separability of various grey matter structures on the basis of the interecho time dependence, ρ, of their water proton transverse relaxation, and, secondly, the correlation between 'ρ' and the atomic absorption spectrometer measurement of tissue iron. The data are taken from Table 3.2, all values are (mean ± std. dev.).

3.5 References

1. D.T. Dexter, F.R. Wells, A.J. Lees, F. Agid, P. Jenner, C.D. Marsden, Increased nigral iron content and alterations in other metal ions occurring in brain in Parkinson disease. J. Neurochem. 52, 1830-1836 (1989).

2. D.T. Dexter, P. Jenner, A.H.V. Schapira, C.D. Marsden, Alterations in levels of iron, ferritin and other trace metals in neurodegenerative diseases affecting the basal ganglia. Ann. Neurol. 32, S94-S100 (1992).

3. P. Riederer, A. Dirr, M. Goetz, E. Sofic, K. Jellinger, M.B.H. Youdim, Distribution of iron in different brain regions and subcellular compartments in Parkinson's disease. Ann. Neurol. 32, S101-S104 (1992).

4. C. Chen, P.A. Hardy, W. Kucharczyk, M. Clauberg, G. Joshi, A. Vourlas, M. Dhar, R.M. Henkelman, MR of human postmortem brain tissue: correlative study between T2 and assays of iron and ferritin in Parkinson and Huntington disease. AJNR 14, 275-281 (1993).

5. D.T. Dexter, A. Carayon, F. Javoy-Agid, Y. Agid, F.R. Wells, S.E. Daniel, A.J. Lees, P. Jenner, C.D. Marsden, Alterations in the levels of iron, ferritin, and other trace metals in Parkinson's disease and other neurodegenerative diseases affecting the basal ganglia. Brain 114, 1953-1975 (1991).

6. P. Drayer, P. Burger, S. Riederer, R. Darwin, S. Bobman, A. Yeates, R. Herfkens, High resolution magnetic resonance imaging for mapping brain iron deposition (abstr). AJNR 6, 466 (1985).

7. P. Drayer, P. Burger, R. Darwin, S. Riederer, R. Herfkens, G.A. Johnson, Magnetic resonance imaging of brain iron. AJR 147, 103-110 (1986).

8. N. Rutledge, S.K. Hilal, A.J. Silver, R. Defendini, S. Fahn, Study of movement disorders and brain iron by MR. AJNR 8, 397-411 (1987).

9. W.J. Milton, S.W. Atlas, F.J. Lexa, P.D. Mozley, and R.E. Gur, Deep gray matter hypointensity patterns with aging in healthy adults: MR imaging at 1.5 T. Radiology 181, 715-719 (1991).

10. C. Chen, P.A. Hardy, M. Clauberg, G. Joshi, J. Parravano, J.H.N. Deck, R.M. Henkelman, L.E. Becker, W. Kucharczyk, T_2 values in the human brain: comparison with quantitative assays of iron and ferritin. Radiology 173, 521-526 (1989).

11. P. Drayer, Basal ganglia: significance of signal hypointensity on T_2-weighted MR images. Radiology 173, 311-312 (1989).

12. J. Brooks, P. Luthert, D. Gadian, C.D. Marsden, Does signal attenuation on high-field T_2-weighted MRI of the brain reflect regional cerebral iron deposition? Observation on the relationship between regional cerebral water proton T_2 values and iron levels. J Neurol Neurosurg Psychiatry 52, 108-111 (1989).

13. A. Bizzi, R.A. Brooks, A. Brunetti, J.M. Hill, J.R. Alger, R.S. Miletich, T.L. Francavilla, G. Di Chiro, Role of iron and ferritin in MR imaging of the brain: a study in primates at different field strengths. Radiology 177, 59-65 (1990).

14. J. Vymazal, R.A. Brooks, O. Zak, C. McRill, C. Shen, G. Di Chiro, T_1 and T_2 of ferritin at different field strengths: effect on MRI. Magn Reson Med 27, 368-374 (1992).

15. J. Vymazal, R.A. Brooks, C. Baumgarner, V. Tran, D. Katz, J.W.M. Bulte, D. Urgosik, G. Di Chiro, Is there a quantitative relation between T2-shortening and brain iron concentration? in "Proc., SMRM, 12th annual meeting, New York, 1993," p. 1276.

16. G. Bartzokis, M. Aravagiri, W.H. Oldendorf, J. Mintz, S.R. Marder, Field dependent transverse relaxation rate increase may be a specific measure of the tissue iron stores. Magn. Reson. Med. 29, 459-464 (1993).

17. F.Q. Ye, W.R.W. Martin, J. Hodder, P.S. Allen, Brain iron imaging exploiting heterogenous-susceptibility-enhanced proton relaxation, in "Proc., SMR 2nd meeting, San Francisco, California, 1994," P. 5.

18. B. Hallgren, P. Sourande, The effect of age on the non-haemin iron in the human brain. J Neurochem 3, 41-51 (1958).

19. H. Koenig, R.D. Brown III, J.F. Gibson, R.J. Ward and T.J. Peters,.Relaxometry of ferritin solutions and the influence of the Fe^{3+} core ions. Magn Reson Med 3, 755-767 (1986).

20. R.J. Ordidge, J.M. Gorell, J.C. Deniau, R.A. Knight, J.A. Helpern, Assessment of relative brain iron concentrations using T_2-weighted and T_2*-weighted MRI at 3.0T. Magn. Reson. Med. 32,335-341 (1994).

21. F.Q. Ye, P.S. Allen, Ferritin as a Susceptibility Agent, in "Proc., SMRM, 12th Annual Meeting, New York, 1993," p. 800.

22. S. Meiboom, D. Gill, Modified spin encho method for measuring nuclear relaxation times. Rev. Sci. Instrum. 29, 688-695 (1958).

23. R.S. Menon, P.S. Allen, Application of continuous relaxation time distributions to the fitting of data from model systems and excised tissue. Magn. Reson. Med. 20, 214-227 (1991).

24. K.P. Whitall, A.L. MacKay, Quantitative interpretation of NMR relaxation data. J. Magn. Reson., 86, 134-142 (1989).

25. R. Connor, S.L. Menzies, S.M. St. Martin, E.J. Mufson, Celluar distribution of transferrin, ferritin and iron in normal and aged human brains. J Neurosci Res 27, 595-611 (1990).

CHAPTER 4[1]

Quantification of Brain Iron In Vivo by Means of the Interecho Time Dependence of Image Contrast

4.1 Introduction

The clinical potential of a non-invasive quantification of brain iron, in, for example, the evaluation of Parkinson's disease (PD) or Huntington's disease (HD), has encouraged several efforts to find an iron-specific measure related to brain iron-based relaxation in MRI. The grey matter hypointensity which delineates the globus pallidus (GP), the red nucleus, and the substantia nigra in T_2-weighted images has been attributed for some considerable time to the anatomic localization of brain iron (1,2). Despite the supportive nature of the evidence for iron involvement in the hypointensity (3), the correlation between brain iron concentration and the actual water proton transverse relaxation rate has not been good (4,5). The reason for this appears to be the significant role played by mechanisms of relaxation that are independent of iron and by the biological variability of the iron-dependent relative to the iron-independent relaxation. T_2-weighted and T_2 calculated images, therefore, provide only a coarse measure of the brain iron concentration, though they continue to be a valuable tool for the visualization of regions of iron accumulation in the brain. To quantify brain iron, a technique must be able to separate iron-dependent relaxation from that of iron-independent mechanisms. One such technique has been implemented by Ordidge *et al.* (6) in which a multiecho sequence enables concurrent measurements of T_2 and T_2^* to be made so that T_2', a measure of the local line broadening could be extracted. An alternative method is proposed in this paper. It follows directly from a model of the mechanism (to be

---

[1] A version of this chapter has been submitted for publication. F.Q. Ye, W.R.W. Martin, P.S. Allen, Quantification of brain iron in vivo by means of the interecho time dependence of image contrast. *Magn Reson Med* (1995).

described below) by means of which accumulated iron acts on mobile water protons, which in turn follows from the form in which iron accumulates in brain .

The most abundant accumulations of brain iron occur in the grey matter nuclei which belong to the so-called extrapyramidal system, which includes not only the GP, the red nucleus, and the substantia nigra, but also the putamen (PM), dentate nucleus, and caudate nucleus. Although various macromolecules, including many iron-enzymes, can bind iron in the brain, by far the most abundant form of brain iron is as ferritin iron, which accounts for about one-third of the iron in the whole brain (7). Moreover, the cellular distribution of brain iron is not uniform, it being found predominantly in glial cells (1, 8-10). Based on our previous work (11-12), in which it was shown that cellular compartmentalization of large paramagnetic susceptibility differences can promote large increases in relaxation rates that are in turn highly sensitive to the interecho time (Δ_{180}) of CPMG sequences (13), this paper proposes and evaluates a quantitative brain iron imaging method that takes advantage of the regional interecho time dependence of the tissue relaxation. The hypothesis is that the glial accumulation of iron gives rise to local, highly non-uniform, concentrations of paramagnetic susceptibility which, in the presence of a large static magnetic field, produce field gradients over dimensions of the order of tens of microns. Diffusing water molecules ($D \sim 10^{-9}$ m^2s^{-1}) sample such a field heterogeneity over the same time scale as is typical for interecho times of CPMG sequences and the apparent relaxation rate becomes interecho time dependent. In an in-vitro study, such an interecho time dependence has been shown to correlate with independent atomic absorption measurements of brain iron in excised normal human grey matter samples (Chapter 3). In this paper, we report an imaging sequence from which the interecho time dependence of the transverse relaxation rate, first, of various phantoms and, secondly, brain structures in a group of healthy volunteers, were subsequently obtained.

4.2 Methods

4.2.1 Quantitative Imaging Sequences

A composite of three imaging sequences is illustrated in Figure 4.1, the objective of which is to provide a spatial map of the interecho-time-dependent relaxation rate enhancement, δR_{2app}, due to the diffusion of water through field gradients close to glial localized brain iron. Each of the sequences combines two functional parts, namely, a relaxation preparation and a spatial encoding. However, the relaxation preparation, shown as a, b, and c in Figure 4.1 is unique to each sequence. In a, the preparation is simply a 90° excitation without relaxation delay. In b and c, composite 180° pulses follow the 90° excitation and are used to distinguish the interecho time dependence from two well separated interecho time preparations, namely, Δ_{180} = 60 ms for b and Δ_{180} = 6 ms for c. The δR_{2app} information is derived from combinations of the images from this group of three uniquely prepared sequences. All the 180° refocussing pulses are phase shifted by $\pi/2$ from the excitation pulse. The composite pulses used here are in the form of $(90°)_x(180°)_y(90°)_x$, to give an equivalent refocussing pulse of $(180°)_y$ whose phase is $\pi/2$-shifted from the $(90°)_x$ excitation pulse (14). Use of composite pulses can compensate experimental imperfections such as RF field inhomogeneities, and hence increase the reliability of transverse relaxation measurements (15). For sequences b and c a spoiler gradient, whose purpose is to diminish the imaging artifacts from unwanted stimulated echoes, is turned on during the refocussing intervals.

Two R_{2app} images are obtained (at interecho times 6 ms and 60 ms) by combining on a pixel by pixel basis, sequences a and b, and a and c respectively, and by using simple two-point fitting. The δR_{2app} image matrix is then obtained from the difference between the two R_{2app} images. The choice of interecho times was made to maximize δR_{2app}, while at the same time maintaining a measurable signal from regions

richest in iron, e.g. GP with $T_2 \sim 60$ ms.

All the imaging was performed on a Philips GYROSCAN 1.5 T system using a standard head coil. The slice thickness was 5 mm with 128 phase-encoding steps. The repetition time, TR, was 2200 ms and the constant echo time in the imaging part of the sequence was 25 ms.

4.2.2 Model Phantom Demonstration

Although a similar interecho time dependence of R_{2app} has been previously demonstrated in-vitro using red blood cell suspensions (see Chapter 2), and in excised tissues (Chapter 3), and the postulated mechanism successfully simulated from a computer model (Chapter 2), the efficacy of the imaging protocol was nevertheless first established using the model phantom shown in Figure 4.2 and a series of interecho times between 6 ms and 80 ms. The phantom was a 1% agarose gel into which were interspersed seven other 1% gel compartments, each containing 5% by volume 15 μm (in diameter) styrene micro-spheres (Bangs Laboratory, Carmel, IN). The microspheres were introduced into the gel to provide a matrix of surfaces that could produce inhomogeneities in magnetic field by separating regions of different susceptibility. A paramagnetic susceptibility difference between the microspheres and the gel was brought about by introducing DyDTPA into the gel. The concentration of DyDTPA was incremented between 0 and 10 mM over the seven phantoms, thus giving rise to a magnetization difference, ΔM, between gel and microspheres that ranged between 0 and 6.4 A/m at 1.5 T. The size of the microspheres and their density in the sample were chosen so that they would be representative of the iron-rich glia in the brain tissue.

4.2.3 In-Vivo Demonstration

A group of healthy volunteers was evaluated, whose age range was limited to 24

to 44 years (n = 11, mean age = 33 ± 7 yr), in order to minimize variations in brain iron accumulation due to aging or to pathology. For each individual, a single slice containing the basal ganglia was imaged using the sequences shown in Figure 4.1. Region of interest (ROI) data for R_{2app} and δR_{2app} were obtained for the four brain structures GP, PM, thalamus (TH), and the frontal white matter tract (fWM). Delineation of those structures was facilitated by T_1-weighted and T_2-weighted images of the same slice, an example of which is shown in Figure 4.3. No ROI had less than 14 pixels.

4.3 Results and Discussion

4.3.1 Model Phantom Demonstration

A δR_{2app} image of the gel-microsphere phantom is shown in Figure 4.4, demonstrating the δR_{2app} differences between the phantom compartments. The image quantification of the interecho time dependence of δR_{2app} of the gel-microsphere phantom is shown in Figure 4.5, and the corresponding quantification of the δR_{2app} dependence on the magnetization difference ΔM, that was brought about by the DyDTPA inside gel matrix, is shown in Figure 4.6. Although several relaxation mechanisms are undoubtedly active in the phantom, those that are not interecho time dependent will be absent from the δR_{2app} image. Data from the compartment containing both the microsphere and gel but devoid of DyDTPA and ΔM, see Figure 4.5, show that the mechanisms active in the agar gel will not affect the δR_{2app} image, and it also reflects the fluctuations in R_{2app} meaurements from the images. The increasing interecho time enhancement of the relaxation with increasing ΔM, shown in Figures. 4.5 and 4.6, demonstrates the ability of the δR_{2app} image to detect changes in ΔM. In the phantom, magnetization differences are measurable to within about ±0.5 A/m from a graph such as that shown in Figure 4.6. Any direct DyDTPA relaxation effects that are not interecho time dependent, and which may be apparent in the baseline Δ_{180} = 6 ms data of the

imaging protocol, will also be removed by taking the δR_{2app} difference image. The dependence of δR_{2app} on ΔM illustrated in Figure 4.6 indicates that one might anticipate changes of a factor of ~ 2.5 in δR_{2app} from PM between the normal early adult brain and a more severe case of HD (5).

4.3.2 In-Vivo Demonstration

Typical images from one of the volunteers are shown in Figure 4.7. The degree of hypointensity of the iron-rich GP seen in the T_2-weighted images clearly depends on the choice of interecho time in the preparation period. When these images form the basis of the calculated δR_{2app} image, the difference in hypointensity translates into a greater δR_{2app} for the GP.

The numerical results of Student's 't' tests of the data from the eleven normal volunteers are shown in Tables 4.1 and 4.2. δR_{2app} was detectable from all four brain regions (GP, PM, TH and fWM). The paired t test in Table 4.2 shows that GP and PM could be significantly differentiated from the other two regions and from each other by their δR_{2app} values ($p < 0.01$), whereas TH and fWM were not significantly different from each other ($p = 0.17$). This result for TH and fWM is not altogether unexpected. Accepted measurements of the typical iron concentrations in adult brain (7) indicate that any accumulation of iron in TH or fWM, over that which is typical in the cortex or in white matter, is a factor of two or more less than the accumulation in GP and PM. Also, bearing in mind that these measurements were made on brain not subject to either disease related or appreciable age related accumulations of iron (accumulations that can increase iron content several fold, (5)), these measurements indicate that this imaging method could very well provide at 1.5 T a means to monitor iron accumulation in disease, at least from the GP and PM. At higher field strengths of 3 T for example, where the work of Ordidge *et al.* (6) has been carried out, expectations will be correspondingly higher

because the heterogeneous susceptibility effects will increase linearly with field strength and give a potential factor of two increase in sensitivity.

The hypothesis which we are making by linking δR_{2app} and the glial accumulation of iron is itself based on several component assumptions. It is instructive to review this chain of assumptions to see if it holds together quantitatively. By making a rough assumption that one-third of the 21 mg Fe/100 g wet wt brain iron is in ferritin (7), and that the ferritin iron is the overwhelmingly dominant source of paramagnetism, we only need to consider 7 mg Fe/100 g wet wt as the pool of brain iron. If we further assume that only half of this ferritin is "stored" in iron-rich glial cells which are assumed to be evenly distributed and to occupy 5% relative volume, then ~ 12.5 mM ferritin iron can be considered to actively produce the ΔM for relaxation enhancement. The other half is evenly distributed in the tissue at 0.66 mM and will slightly inhibit the microscopic susceptibility difference. Assuming a susceptibility ratio $\chi_m^{DyDTPA}/\chi_m^{Ferritin\ Fe} = (10.6/3.8)^2 = 7.8$ (11), the concentration difference of ~ 12 mM ferritin-iron can give rise to a ΔM due to iron-rich glial cells of 1 A/m in the GP at 1.5 T. Such an estimate is in accord with the measured δR_{2app} for GP and the relationship between δR_{2app} and ΔM for the gel-microsphere phantom.

4.4 Conclusion

An imaging protocol that provides a quantitative assessment of the regional variations in brain iron has been proposed and evaluated on both a phantom and a group of normal volunteers. This protocol is based on a model of transverse relaxation enhancement brought about by water diffusion in the field gradients produced by a heterogeneous distribution of cellular susceptibility. A model similar to this has previously been evaluated in vitro on a RBC preparation (12) and the identical model has been used to explain δR_{2app} data from excised human brain tissue (Chapter 3). In vivo,

the imaging protocol not only enables one to delineate the iron bearing structures from normal brain, but also to quantify the difference in iron content between GP, PM and the other iron bearing structures in a manner that is significant at the 99% level. This sensitivity to sequestered iron is sufficient, in diseases such as HD and PD, to provide a scale of regional iron content, that, by correlation with established clinical scales, could provide an alternative measure of disease progression.

Table 4.1.

Apparent transverse relaxation rate, R_{2app}, and a measure of its interecho time dependence, δR_{2app}, in various brain structures in age-range-limited healthy volunteers (n = 11).

Regions	Δ_{180} (ms)	R_{2app} values (s^{-1}) mean (std. dev.)	δR_{2app} (s^{-1})	p value (paired t test)
GP	60	17.2 (1.1)	2.4	0.0001
	6	14.8 (1.1)		
PM	60	14.4 (1.1)	1.3	0.0001
	6	13.1 (1.1)		
TH	60	13.7 (0.6)	0.6	0.0048
	6	13.0 (0.7)		
fWM	60	14.9 (0.7)	0.82	0.0014
	6	14.1 (0.8)		

Table 4.2.

A comparison of the interecho-time-dependent relaxation enhancement, δR_{2app}, between various brain structures in age-range-limited healthy volunteers (n = 11).

Brain Structure	Compared with	Mean δR_{2app} difference (s^{-1})	Paired t value	p value
GP				
	PM	1.2	13.8	0.0001
	TH	1.8	18.4	0.0001
	fWM	1.6	11.6	0.0001
PM				
	TH	0.6	5.6	0.0002
	fWM	0.4	4.2	0.0019
TH				
	fWM	-0.2	-1.5	0.17

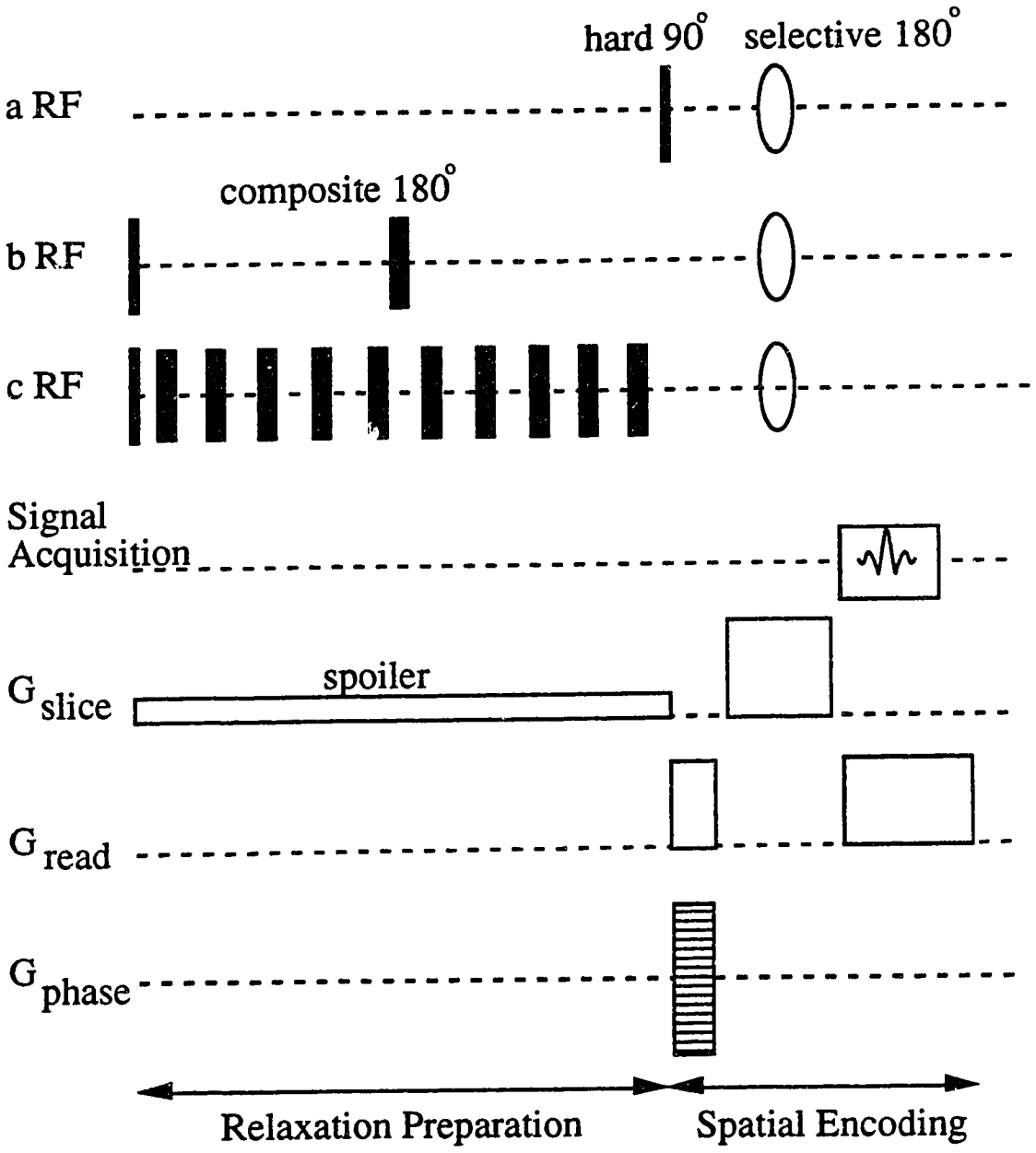

Figure 4.1. An illustration of the imaging sequences used in measuring the interecho time dependent transverse relaxation enhancement.

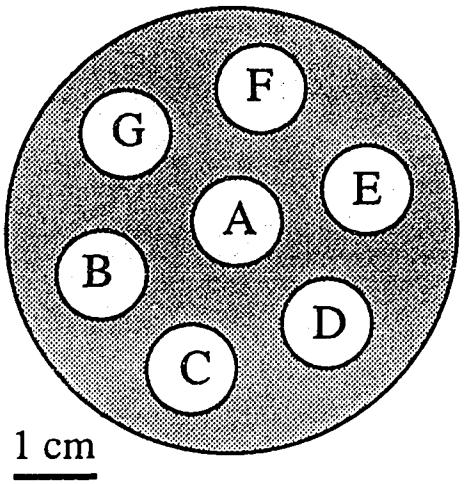

Figure 4.2. An illustration of the gel-microsphere model phantom. All of the compartments are made of a 1% agarose gel, with 5% (by volume) microspheres suspended in the cylinders A to G before gelation. The concentrations of DyDTPA in the cylinders are respectively, A: 0 mM; B: 1 mM; C: 6 mM; D: 4 mM; E: 8 mM; F: 2 mM, and G: 10 mM. The gel in the background compartment contains neither microspheres nor DyDTPA.

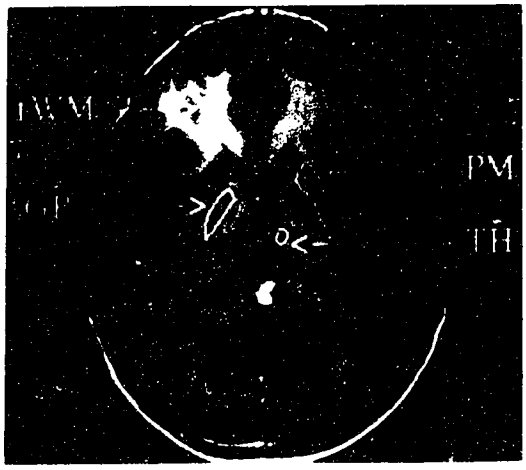

Figure 4.3. A T_1-weighted brain image illustrating the slice of interest. The four brain structures studied, namely, the globus pallidus (GP), the putamen (PM), the thalamus (TH), and a frontal white matter tract (fWM) are delineated.

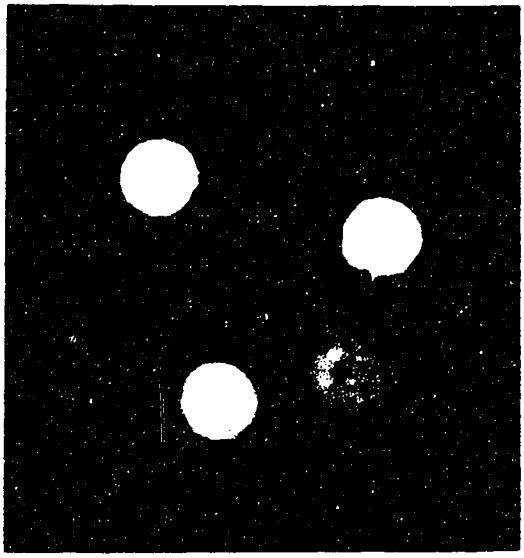

Figure 4.4. A typical δR_{2app} image of the gel-microsphere model phantom.

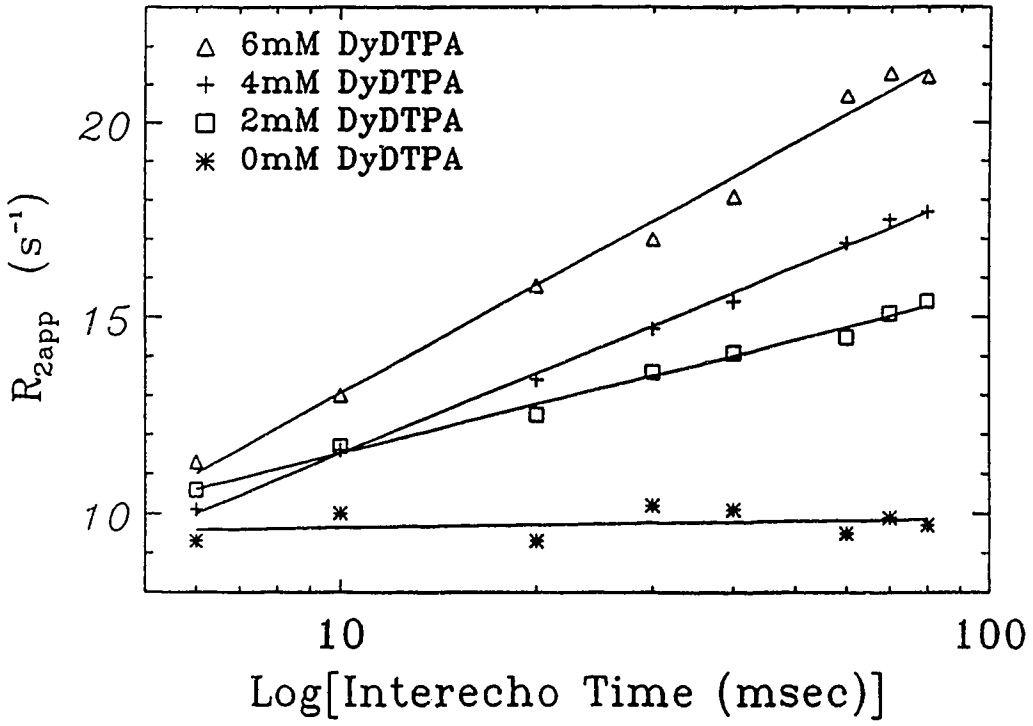

Figure 4.5. The dependence of the relaxation rate R_{2app} on the CPMG interecho time, Δ_{180}, in the gel-microsphere phantoms.

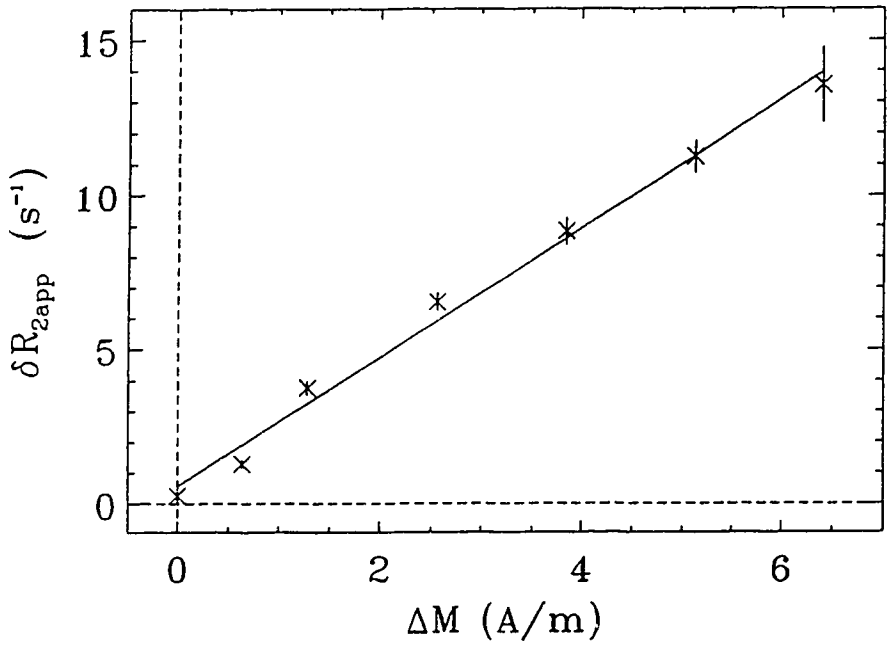

Figure 4.6. The dependence of δR_{2app} on the internal magnetization difference, ΔM, in the gel-microsphere phantom. The values of δR_{2app} (mean ± std. dev.) were determined in three repeated measurements.

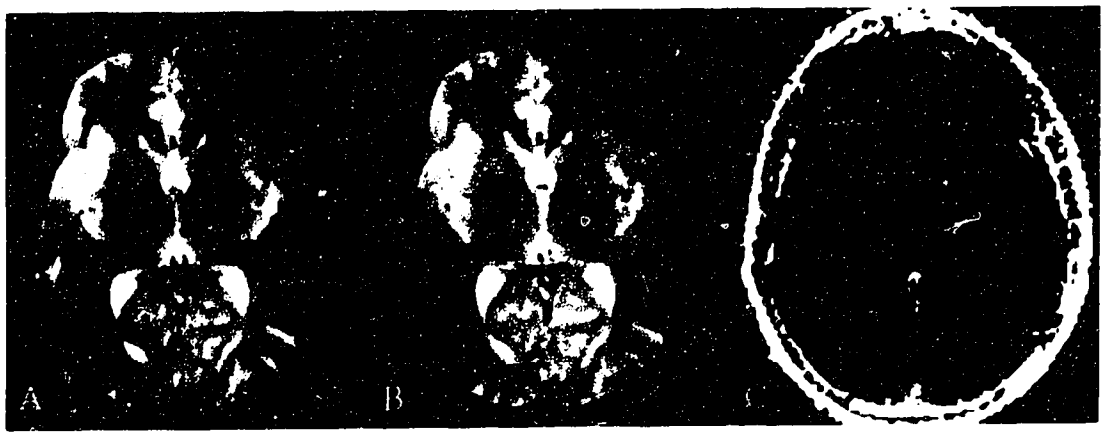

Figure 4.7. Two typical T_2-weighted brain images acquired using the different interecho time values in their preparatory sub-sequence plus the corresponding calculated δR_{2app} image, where **A**, is a T_2-weighted image acquired with Δ_{180} = 60 ms, and one refocussing pulse in the preparatory period; **B**, is a T_2-weighted image acquired with Δ_{180} = 6 ms, and ten refocussing pulses in the preparatory period; and **C**, is the δR_{2app} image derived from the difference between the two images in A and B.

4.5 References

1. B. P. Drayer, P. Burger, R. Darwin, S. Riederer, R. Herfkens, G.A. Johnson, MRI of brain iron. AJR 147, 103-110 (1986).

2 J. N. Rutledge, S. K. Hilal, A. J. Silver, R. Defendini, S. Fahn, Study of movement disorders and brain iron by MR. AJNR 8, 397-411 (1987).

3 B. P. Drayer, Basal ganglia: significance of signal hypointensity on T2-weighted MR images. Radiology 173, 311-312 (1989).

4 J. C. Chen, P. A. Hardy, M. Clauberg, G. Joshi, J. Parravano, J. H. N. Deck, R. M. Henkelman, L. E. Becker, W. Kucharczyk, T_2 values in the human brain: comparison with quantitative assays of iron and ferritin. Radiology 173, 521-526 (1989).

5. J. C. Chen, P. A. Hardy, W. Kucharczyk, M. Clauberg, G. Joshi, A. Vourlas, M. Dhar, R. M. Henkelman, MR of human postmortem brain tissue: correlative study between T_2 and assays of iron and ferritin in Parkinson and Huntington disease. AJNR 14, 275-281 (1993).

6 R.J. Ordidge, J.M. Gorell, J.C. Deniau, R.A. Knight, J.A. Helpern, Assessment of relative brain iron concentrations using T_2-weighted and T_2*-weighted MRI at 3.0 T. Magn. Reson. Med. 32,335-341 (1994).

7 B. Hallgren, P. Sourande, The effect of age on the non-haemin iron in the human brain. J Neurochem 3, 41-51 (1958).

8 C. Francois, J. Nguyen-Legros, G. Percheron, Topographical and cytological localization of iron in rat and monkey brains. Brain Research 215, 317-322 (1981).

9 J. M. Hill, R. C. Switzer, The regional distribution and cellular localization of iron in the rat brain. Neuroscience 11, 595-603 (1984).

10 J. R. Connor, S. L. Menzies, S. M. St. Martin, E. J. Mufson, Celluar distribution of transferrin, ferritin and iron in normal and aged human brains. J Neurosci Res 27, 595-611 (1990).

11 F. Q. Ye, P. S. Allen, Ferritin as a Susceptibility Agent, in "Proc., SMRM, 12th Annual Meeting, New York, 1993," p. 800.

12. F. Q. Ye, P. S. Allen, The Paramagnetic-Susceptibility-Enhanced Water Proton Transverse Relaxation in Cell Suspensions, in "Proc., SMRM, 12th Annual Meeting, New York, 1993," p. 802.

13 S. Meiboom, D. Gill, Modified spin-echo method for measuring nuclear relaxation times. Rev. Sci. Instum. 29, 688-693 (1958).

14 R.R. Ernst, "Principles of Nuclear Magnetic Resonance in One and Two Dimensions". Oxford University Press, New York, 1987.

15 S. Majumdar, S.C. Orphanoudakis, A. Gmitro, M. O'Donnell, J.C. Gore, Errors in the measurement of T2 using multiple-echo MRI techniques. I. Effects of radiofrequency pulse imperfection. *Magn Reson Med* 3, 397-417 (1986).

CHAPTER 5[1]

Increasing Striatal Iron Content With Aging: A Risk Factor for Free Radical Mediated Neuronal Damage

5.1 Introduction

Free radical mediated mechanisms have been postulated as one of the factors which may contribute to neuronal damage in Parkinson's disease (PD) and other neurodegenerative conditions associated with aging, as well as in the aging process itself. Cytotoxic free radicals can be generated in the brain by the oxidation/reduction reactions which produce the high-energy compounds required by cellular metabolic processes. These reactions are catalyzed by transition metals and are more likely to occur in brain regions which contain a high concentration of these elements. Hence, any regional increase in brain iron concentration may increase the potential for local free radical formation and for free radical-mediated lipid peroxidation.

The brain is known to have an extremely high iron content. Cerebral iron distribution is heterogeneous with concentrations as high as 200 μg/g wet weight in regions of highest iron content (1) in contrast to the normal liver concentration of about 150 μg/g. It was established initially by Spatz in 1924 and subsequently confirmed by others (2-4) that brain iron concentration is highest primarily in the basal ganglia. The relationship between aging and basal ganglia iron content, however, has not received major attention. With direct post-mortem measurements, Hallgren and Sourander (2) observed brain iron in general to be very low at birth, but to gradually increase during the first two decades of life. They observed, in addition, that pallidal iron content did

---

[1] A version of this chapter has been submitted for publication. W.R.W. Martin, F.Q. Ye, P.S. Allen, Increasing striatal iron content with aging: a risk factor for free radical mediated neuronal damage. *Neurology* (1995).

not change after 30 years of age, whereas putamen and caudate iron content continued to increase very gradually. Little is known about the functional importance of iron in the basal ganglia except that its concentration exceeds by about 90% the requirements of iron-dependent enzymes, membrane structural proteins, iron-sulfur proteins, etc. (5).

A number of studies have suggested increased iron accumulation in the basal ganglia in various neurodegenerative disorders, including Parkinson's disease. Although the role played by excess iron in these conditions is unknown, one possibility relates to the ability of iron to promote the formation of toxic oxygen free radicals, particularly in parts of the brain which contain a high dopamine concentration. If basal ganglia iron content increases as part of the normal aging process, it could represent a risk factor for the development of progressive neurodegenerative disorders affecting these structures in the elderly population via the mechanism of increased oxidant stress. The purpose of the present study was to determine the relationship between age and an in vivo measurement of basal ganglia iron content in normal subjects by using a magnetic resonance (MR) method developed in our laboratory. Our methodology quantifies the effects of paramagnetic centres sequestered inside cellular membranes thereby enabling the determination of a quantitative index of local brain iron content (6).

5.2 Methods

5.2.1 Patients

A series of normal, healthy individuals (n = 20) was recruited by advertising within the local university community and through the Edmonton General Hospital/University of Alberta Movement Disorder Clinic. Subjects ranged in age from 24 to 79 yr (mean ± SD = 46.3 ± 16.7 yr). All subjects were neurologically normal and

without significant medical illnesses. The protocol was approved by the University of Alberta Research Ethics Board, and all subjects gave informed consent.

5.2.2 Magnetic Resonance Studies

MR studies were performed on a Philips GYROSCAN 1.5 T imaging system. To quantify the enhanced transverse relaxation of water protons due to the presence of iron, a spin echo based pulse sequence was used that permitted the initial imaging magnetization to be sensitized to the interecho time dependence of the apparent transverse magnetization decay rate R_{2app} (= $1/T_{2app}$) by means of a preparatory sub-sequence (A detailed description of the image sequence is presented in Chapter 4). This sub-sequence consisted of a variable train of hard (non-selective) 180° refocussing pulses that provided a partially decayed transverse magnetization prior to the image acquisition part of the overall sequence. The image acquisition part employed a slice-selective refocussing pulse (slice thickness 5 mm) and a fixed echo time of 25 ms. A standard head coil and 128 phase-encoding steps were used. Image field of view was 16 cm. T_1 effects were minimized by using a repetition time (TR) of 2200 ms. The phases of all 180° refocussing pulses were $\pi/2$ shifted from the excitation pulse.

Three variants of the preparatory sub-sequence were used in combination to derive the refocussing interval dependence. The first variant provided the full transverse magnetization by means of a single 90° excitation pulse and no relaxation delay prior to the image acquisition sub-sequence. In the second variant, a single 180° pulse in a delay period of 60 ms followed the excitation pulse to provide a refocused, but partially decayed transverse magnetization. The third variant employed a train of ten 180° pulses, separated by an interecho time of 6 ms, to replace that single 180° pulse in the second variant but maintained the total decay time of 60 ms. From the data sets obtained with these three sequence variants, two separate R_{2app} images were derived,

each one reflecting a two point fit to R_{2app} at every pixel and using the first variant to provide the initial point in each case. By subtracting the two R_{2app} images, a δR_{2app} difference image was obtained.

Initially, a sagittal T_1-weighted image was employed to facilitate the selection of a single transverse slice parallel to and 5 mm above the line drawn from the anterior to the posterior commissure (the AC-PC line). Data was then acquired from this single slice using the methodology described above. The entire patient procedure took between 50 and 90 min.

5.2.3 Data Analysis

Numerical values were obtained from regions-of-interest (ROIs) which were initially located manually by means of T_2-weighted images. Irregular ROIs were fitted to the structures in question to maximize the number of pixels (pixel size 1.25 mm x 1.25 mm) for each ROI. The average ROI sizes ± 1 SD were 36 ± 10 pixels for globus pallidus (GP), 61 ± 13 for putamen (PM), and 12 ± 4 for the caudate head (CD). A circular ROI (18 ± 5 pixels) was placed near the center of the thalamus (TH). These ROIs were then automatically transposed to the δR_{2app} difference images. A large ROI (~ 2000 pixels) was defined that encompassed most of the slice but excluded the ventricles and basal ganglia to provide a reference in each individual studied. From this ROI, an average background δR_{2app} value was obtained. This background reflects any interecho time dependence of the magnetization decay due to mechanisms other than accumulated iron. (It should be noted that the effects of accumulated iron are an order of magnitude greater than those of other mechanisms which show an interecho time dependence.) The background average also allows for standardization against interscan variability. The numerical values of a regional ΔR_{2app} which are quoted below are the difference of the regional δR_{2app} from the average background value. Regional ΔR_{2app}

provides an index of local tissue iron content. The relationship between age and ΔR_{2app} was assessed by a correlation analysis. Calculations from regions with very low iron content occasionally yielded small negative values for ΔR_{2app}. For purposes of correlation analysis, these were equated to zero.

5.3 Results

In this group of normal subjects, we observed the following regional ΔR_{2app} means and standard deviations: globus pallidus, 2.00 ± 0.37 s^{-1}; putamen, 0.99 ± 0.44 s^{-1}; caudate, 0.42 ± 0.32 s^{-1}; and thalamus, 0.25 ± 0.20 s^{-1}. There was a strong direct relationship between age and our measurements of regional iron content (ΔR_{2app}) in both the putamen ($r = 0.76$, $p < 0.001$) and the caudate ($r = 0.69$, $p < 0.001$, Figures 5.1 and 5.2). Although pallidal ΔR_{2app} values were higher than striatal values, there was no significant relationship between pallidal ΔR_{2app} and age ($r = 0.32$, $p = 0.17$, Figure 5.3). The lowest values observed were in the thalamus and were unrelated to age ($r = 0.13$, $p = 0.58$, Figure 5.4).

5.4 Discussion

Our results indicate that the normal aging process is associated with a progressive increase of iron content in the striatum, particularly in the putamen, but not in the pallidum or thalamus. This increase in local brain iron content may increase the probability of the formation of neurotoxic free radicals in the striatum therefore representing a risk factor for the development of progressive neurodegenerative disorders associated with aging, such as Parkinson's disease, which may affect nigrostriatal nerve endings by the mechanism of increased oxidant stress.

Iron is not present in the brain at birth, but becomes detectable during the first decade of life, reaching adult levels by about 20 years of age (2,7). Iron is thought to

enter the brain bound to transferrin by way of transferrin receptors (8). Once in the brain, it is stored primarily in glial cells (oligodendrocytes and microglia) where it is bound to the storage protein ferritin (3,9). In adults, changes in the peripheral pharmacokinetics of iron have little influence on brain iron concentrations. It is not clear how much of the iron increase associated with aging is in a reactive form. If bound to a protein such as ferritin so that it is unable to participate in oxidation/reduction reactions, its accumulation may not be associated with increased free radical production or oxidant stress.

A free radical is any species which is capable of independent existence that contains an orbital with one or more unpaired electrons. Most free radicals are unstable and highly reactive by virtue of their tendency to extract an electron from neighbouring molecules to complete their own orbital. Oxygen-based free radicals, particularly the hydroxyl radical ($OH^{\cdot}$), are of particular interest in neurological disorders because of their high reactivity with virtually all biological molecules and their tendency to initiate destructive chain reactions (10,11). In the brain, hydroxyl radicals can react with lipids contained in cellular membranes and start the chain reaction of lipid peroxidation resulting in extensive membrane damage and ultimately in cell degeneration. The hydroxyl radical is continuously produced in the human body in large part by the reaction of transition metal ions with H_2O_2. The superoxide radical ($O_2^{\cdot-}$), although much less reactive than $OH^{\cdot}$, is also of biological significance, in part because of its capability of inactivating Complex I of the mitochondrial electron transport chain (12). $O_2^{\cdot-}$ is produced by the autooxidation of catecholamines, by leakage of electrons from the electron transport chains, and by various cell types including activated phagocytes (13), fibroblasts (14,15) endothelial cells (16) and lymphocytes (17). A major defense mechanism against excess $O_2^{\cdot-}$ production is the enzyme superoxide dismutase (SOD).

However, SOD accelerates the conversion of O_2^- to H_2O_2 and can therefore potentially increase production of the highly reactive $OH^\cdot$ species.

Transition metals, such as iron, copper, and manganese, have a loosely bound electron and are therefore able to either accept or donate an electron thereby promoting oxidation/reduction reactions and the formation of reactive oxygen species. An increase in local free iron concentration is associated with an increased probability that oxidation reactions will occur and that free radicals will be formed (18,19).

The brain is thought to be particularly vulnerable to the effects of cytotoxic free radicals generated as a result of oxidant stress for several reasons (20). First, the brain is responsible for approximately 20% of total body oxygen consumption while comprising less than 2% of total body weight, thereby providing the potential for production of significant quantities of oxygen free radicals by way of the electron transport chain. Second, the brain contains large amounts of polyunsaturated fatty acids which are components of cell membrane and substrates for free radical induced lipid peroxidation. Third, the brain is relatively deficient in mechanisms which are thought to be protective against the toxic effects of free radicals. Lastly, as discussed above, the accumulation of iron in specific brain regions increases the potential of local free radical production. The latter potential is accentuated by a possible relative deficiency in the brain of iron binding proteins which can trap iron in a non-reactive form (21).

Within the brain, there are several factors which suggest that the striatum may be particularly vulnerable to oxidative stress in association with aging. First, as suggested by the present study and supported by previous data (2), there is an age-related increase in striatal iron content. Second, dopaminergic neurons may be particularly susceptible to oxidative stress by virtue of the metabolism of dopamine to H_2O_2 both enzymatically by monoamine oxidase (MAO) (22) and nonenzymatically by

autooxidation (23). Because striatal MAO activity increases with age (24), increased H_2O_2 and hence free radical production may also occur with aging. In addition, there may be also be an increase in autooxidation with age (25). Most of these factors apply not only to the striatum, but also to the substantia nigra. The application of our MR methodology at 1.5 T, however, did not allow us to obtain reproducible nigral ΔR_{2app} measurements, largely because of the small size of the substantia nigra and because of artifacts introduced by small head movements.

The majority of previous studies of brain iron content with MR imaging have employed either T_2-weighted images or quantitative local T_2 measurements. With conventional T_2-weighted imaging at a field strength of 1.5 T, reduced signal is normally evident in the globus pallidus, red nucleus, dentate nucleus, and substantia nigra (26). Olanow *et al.* have previously reported striatal changes on T_2-weighted images occurring with age, and have suggested that these changes are due to increasing striatal iron concentration (7). Although these changes are related in part to local increases in iron concentration, the resultant signal intensity is determined by a combination of mechanisms depending not only on the iron distribution, but also on the heterogeneity of magnetic susceptibility in the cellular milieu of individual brain structures, and on the motional modulation of interproton dipolar interactions. Local water content is a very important determinant of T_2. Separating the effects of iron from those of other mechanisms is essential for in vivo quantification of regional iron variations with MR, since previous studies have failed to show a consistent correlation between the direct measurement of tissue iron content and apparent T_2 (27,28).

Our methodology provides a non-invasive measurement of regional brain iron which is more specific than T_2-weighted images or quantitative local T_2 measurements. This methods is based on the assumption that the largest single fraction of iron is stored

as ferritin (2), and that ferritin accumulation within the confines of glial cells (3,10) gives rise to a heterogeneous distribution of iron. These iron-containing cells become paramagnetic centers whose magnetic dipole fields enhance the dephasing of transverse proton magnetization during an MR study.

We have exploited the interecho time dependence of the transverse relaxation which is evident when ferritin is confined by intact cell membranes thus giving rise to a heterogeneous magnetic environment (29). We have shown previously that the interecho time dependence of the transverse decay can be used to provide a specific index of the tissue concentration of iron which is sequestered within cells (see Chapters 3 and 4). This index, ΔR_{2app}, is not subject to the same shortcoming as direct T_2-based methods because it separates the effects of iron from those of other transverse relaxation mechanisms. The ability to effect this separation stems from the magnitude and spatial scale over which the iron-rich glial cells produce field inhomogeneities, as compared with those which characterize magnet generated inhomogeneities or susceptibility difference effects between tissue structures. Although ΔR_{2app} is itself echo time dependent, our previous data show that for a fixed difference in refocussing interval, its value is specifically sensitive to the iron concentration (see Chapters 3 and 4). The subtraction of the two relaxation rate images isolates the interecho time dependent relaxation contributions and removes the intrinsic transverse relaxation terms which are independent of interecho time but vary with local water content. The subtraction of a background to give ΔR_{2app} standardizes each result against normal brain variability and interscan variations, as well as removing the minor refocussing interval dependent decay terms which arise from susceptibility differences between brain structures.

An experimental shortcoming is noticeable in our in-vivo measurement and it might have affected the caudate data of ΔR_{2app}. The shortcoming stems from the lack

of dynamic range that our method has for accommodating the long T_2 of cerebrospinal fluid (CSF). This range is governed by the fixed 60 ms duration of the preparatory subsequence. Lack of dynamic range might have affected our ΔR_{2app} measurements in the caudate head because of the proximity of the lateral ventricles. This experimental uncertainty is reflected in the large variation of caudate ΔR_{2app} seen in Figure 5.2. Neither pallidal nor putamen measurements, however, should have been affected by this shortcoming.

In summary, we have utilized a novel, non-invasive MR technique to quantify changes in iron content in the basal ganglia occurring with age in normal subjects. We have demonstrated a significant positive relationship between increasing age and ΔR_{2app}, an index of local iron content, in both the putamen and caudate. These observations suggest that the probability of striatal free radical production may increase with age and that striatal iron content may be a risk factor for the development of age-related damage to nerve endings in the striatum. Future implementation with a higher magnetic field strength system (e.g., 3.0 T) should improve the signal to noise ratio, thereby enabling faster studies to be performed, lessening the artifact induced by patient movement, and allowing assessment of smaller structures such as the substantia nigra.

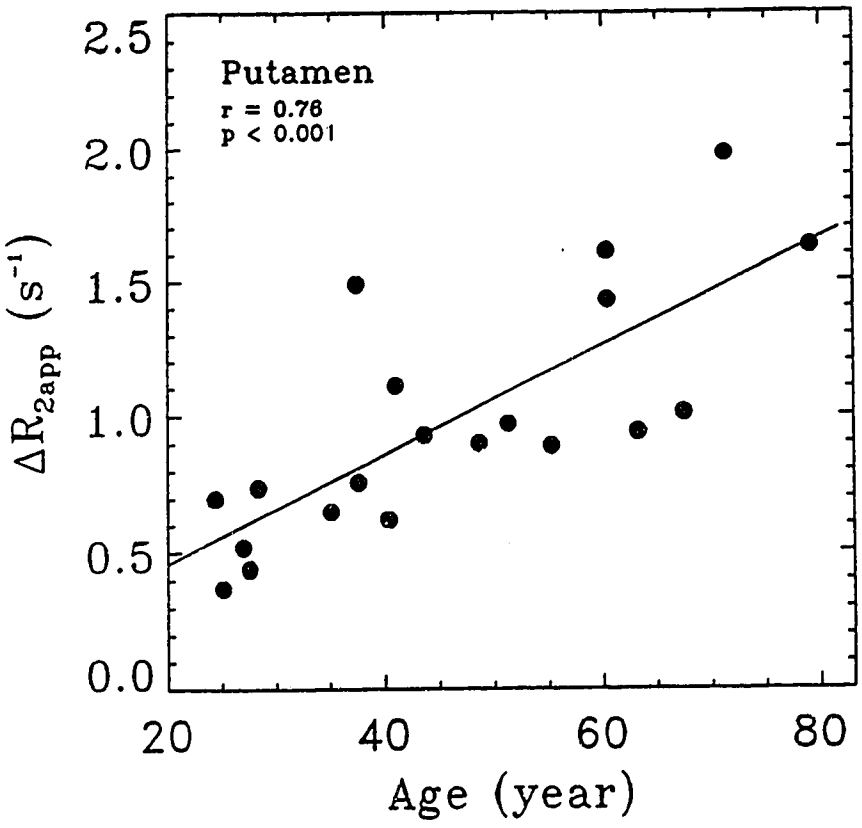

Figure 5.1. The relationship between age and putamen iron content (ΔR_{2app}) in normal subjects. The line represents the best linear fit of the data (r=0.76, p<0.001).

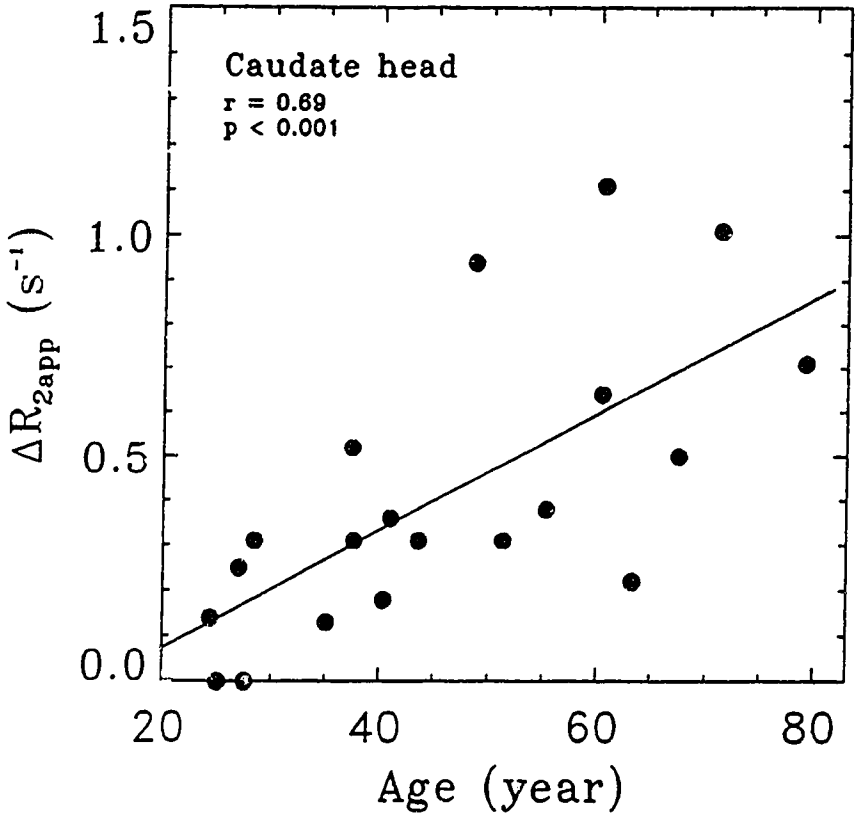

Figure 5.2. The relationship between age and caudate iron content (ΔR_{2app}) in normal subjects. The line represents the best linear fit of the data (r=0.69, p<0.001). Calculations from regions with very low iron content occasionally yielded small negative values for ΔR_{2app}. These are equated to zero on the figure.

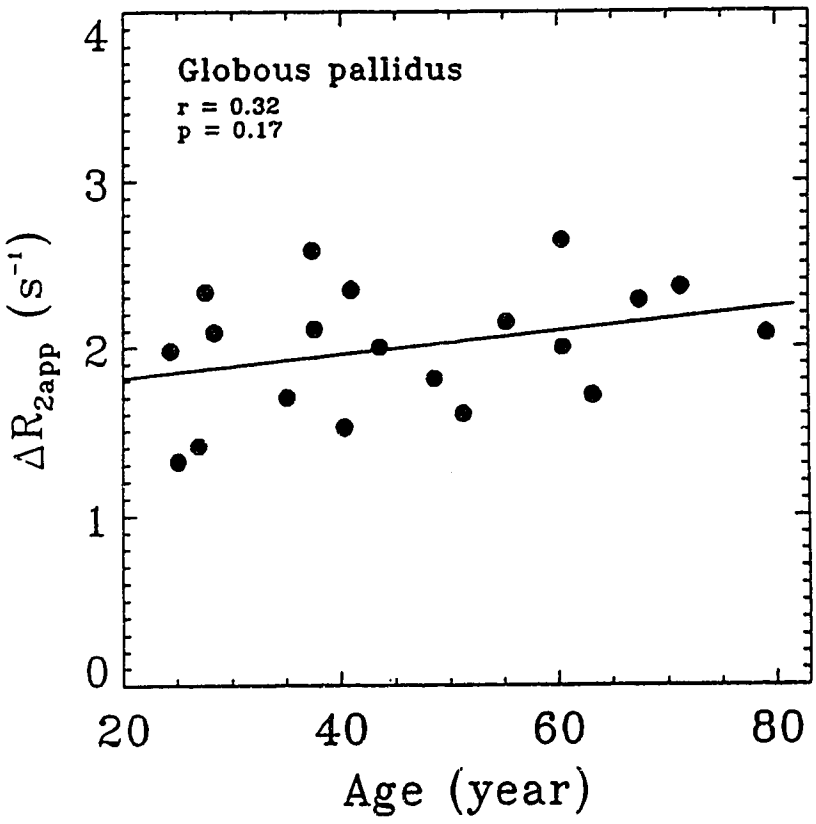

Figure 5.3. The relationship between age and pallidal iron content (ΔR_{2app}) in normal subjects ($r = 0.32$, $p = 0.17$).

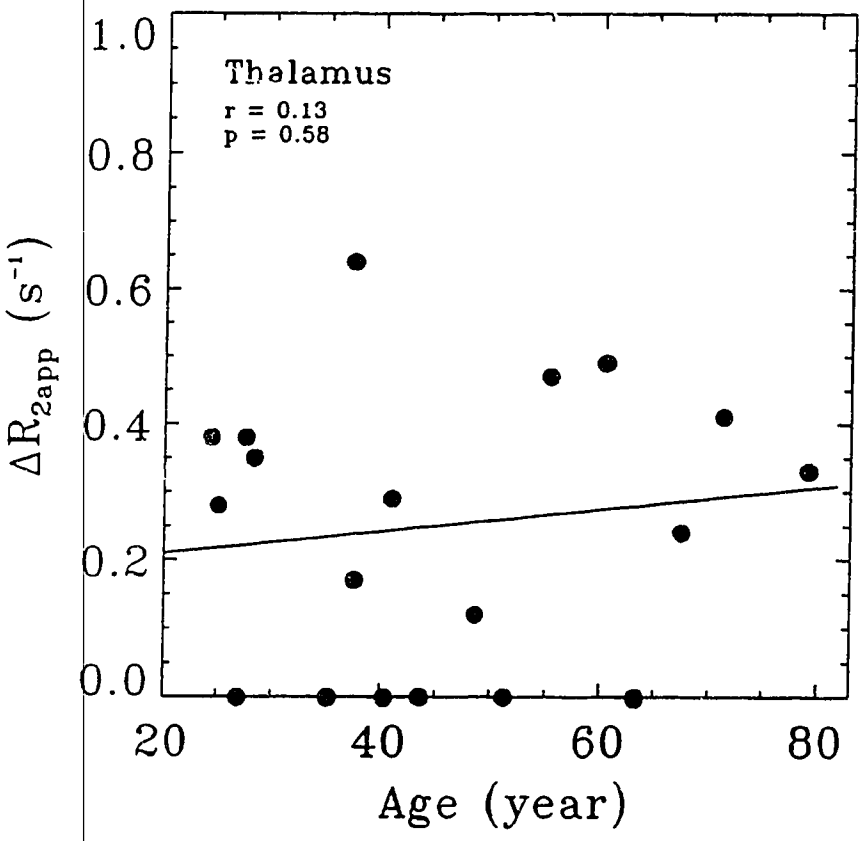

Figure 5.4. The relationship between age and thalamic iron content (ΔR_{2app}) in normal subjects (r = 0.13, p = 0.58). Calculations from regions with very low iron content occasionally yielded small negative values for ΔR_{2app}. These are equated to zero on the figure.

5.5 References

1 D.P. Perl, P.F. Good, Comparative techniques for dtermining cellular iron distribution in brain tissues. *Ann Neurol* 32, S76-S81 (1992).

2 B. Hallgren, P. Sourande, The effect of age on the non-haemin iron in the human brain. *J Neurochem* 3, 41-51 (1958).

3 J.M. Hill, R.C. Switzer, The regional distribution and cellular localization of iron in the rat brain. *Neuroscience* 11, 595-603 (1984).

4 P. Riederer, E. Sofic, W.D. Rausch, B. Schmidt, P.G.P. Reynolds, K. Jellinger, M.B.H. Youdim, Transition metal, ferritin, glutathione, and ascorbic acid in parkinsonian brains. *J Neurochem* 52, 515-520 (1989).

5 M.B.H. Youdim, D. Ben-Schachar, S. Yehuda, P. Riederer, The role of iron in the basal ganglion. *Adv Neurol* 53, 155-162 (1990).

6 F.Q. Ye, W.R.W. Martin, J. Hodder, P.S. Allen, Brain iron imaging exploiting heterogeneous-susceptibility-enhanced proton relaxation. *in* "Proc., SMR, 2nd Annual Meeting, San Francisco, 1994," p. 5.

7 C.W. Olanow, R.C. Holgate, R. Murtagh, C. Martinez, MR images in Parkinson's disease and aging. *in* "Parkinsonism and aging" (D.B. Calne, *et al*, Eds), pp135-144, Raven Press, New York, 1989.

8 J.B. Fishman, J.B. Rubin, J.V. Handrahan, Receptor-mediated transcytosis of transferrin across the blood-brain barrier. *J Neurosci Res* 18, 299-304 (1987).

9 J.R. Connor, S.L. Menzies, S.M. St. Martin, E.J. Mufson, Celluar distribution of transferrin, ferritin and iron in normal and aged human brains. *J Neurosci Res* 27, 595-611 (1990).

10 B. Halliwell, J.M.C. Gutteridge, Role of free radicals and catalytic metal ions in human disease. *Methods Enzymol* 186, 1-85 (1990).

11 B. Halliwell, Oxygenation radicals as key mediators in neurological disease: fact or fiction? *Ann Neurol* 32, S10-S15 (1992).

12 Y. Zhang, O. Marcillar, C. Giulivi, The oxidative inactivation of mitochondrial electron transport chain components and ATPase. *J Biol Chem* 265, 16330-16336 (1990).

13 J.T. Curnutte, B.M. Babior, Chronic granulomatous disease. *Adv Hum Genet* 16, 229-297 (1987).

14 B. Neier, H. Radeke, S. Selle, et al., Human fibroblasts release reactive oxygen species with immunoregulatory potential. *Free Radic Res Commun* 8, 149-160 (1990).

15 G.A.C. Murrell, M.J.O. Francis, L. Bromley, Modulation of fibroblast proliferation by oxygen free radicals. *Biochem J.* 265, 659-665 (1990).

16 B. Halliwell, Superoxide, iron, vascular endothelium, and reperfusion injury. *Free Radic Res Commun* 5, 315-318 (1989).

17 F.E. Maly, The B-lymphocyte: a newly-recognized source of reactive oxygen species with immunoregulatory potential. *Free Radic Res Commun* 8, 143-148 (1990).

18 B. Halliwell, J.M.C. Gutteridge, Iron as a biological pro-oxidant. *ISI Atlas Sci Biochem* 1, 48-52 (1988).

19 B. Halliwell, J.M.C. Gutteridge, Oxygen free radicals and iron in relation to biology: some problems and concepts. *Arch Biochem Biophys* 246, 510-514 (1986).

20 C.W. [illegible] introduction to the free radical hypothesis in Parkinson's disease. *Ann Neurol* 32, S2-S9 (1992).

21 B. Halliwell, Oxidants in the central nervous system: some fundamental questions. *Acta Neurol Scand* 126, 23-33 (1989).

22 G. Cohen, The pathobiology of Parkinson's disease: biochemical aspects of dopamine neuron senescence. *J. Neural Transm.* suppl 19, 89-103 (1983).

23 D.G. Graham, Oxidative pathways for catecholamines in the genesis of neuromelanin and cytotoxic quinones. *Mol. Pharmacol.* 14, 633-643 (1979).

24 L.J. [illegible]te, L.T. Kremzner, Biochemical changes in normal aging in human brain. *Adv. Neurol.* 38, 19-30 (1983).

25 B. Fornstedt, E. Pileblad, A. Carlsson, In vivo autoxidation of dopamine in guinea pig striatum increases with age. *J. Neurochem.* 55, 655-659 (1990).

26 B. Drayer, P. Burger, R. Darwin, S. Riederer, R. Herfkens, G. A. Johnson, MRI of brain iron. *AJR* 147, 103-110 (1986).

27 J.C. Chen, P.A. Hardy, W. Kucharczyk, M. Clauberg, G. Joshi, A. Vourlas, M. Dhar, R.M. Henkelman, MR of human postmortem brain tissue: correlative study between T_2 and assays of iron and ferritin in Parkinson and Huntington disease. *AJNR* 14, 275-281 (1993).

28 J.C. Chen, P.A. Hardy, M. Clauberg, G. Joshi, J. Parravano, J.H.N. Deck, R.M. Henkelman, L.E. Becker, W. Kucharczyk, T_2 values in the human brain:

comparison with quantitative assays of iron and ferritin. *Radiology* 173, 521-526 (1989).

29 F.Q. Ye, P.S. Allen, Ferritin as a Susceptibility Agent, *in* "Proc., SMRM, 12th Annual Meeting, New York, 1993," p. 800.

CHAPTER 6[1]

Basal Ganglia Iron Content in Parkinson's Disease Measured With Magnetic Resonance

6.1 Introduction

Parkinson's disease (PD) is characterized by a loss of dopaminergic neurons projecting from the substantia nigra to the striatum. Clinical rating scales currently provide the most widely used method to assess the degree of motor dysfunction in PD and, by assumption, the degree of nigral cell loss (1-4). While these scales provide a means of assessing clinical severity, they are based on the assessment of deficits which are subject to both intra-observer and inter-observer variability and are very sensitive to the treatment status of the individual patient. They provide an indication of the patient's functional status at a given time but cannot provide an accurate indication of the severity of the underlying neuronal loss itself unless all anti-parkinsonian medications are withdrawn long enough for their clinical effects to completely subside before the patient is assessed. Because this is seldom practical, clinical rating scales only approximate the severity of the underlying nigral pathology and striatal dopamine depletion.

An objective and non-invasive method of measuring the severity of the pathological changes of PD, independently of function, is suggested by the accumulation of iron in the basal ganglia in PD and by the potential for quantifying this accumulation with magnetic resonance (MR). It was established by Spatz in 1924 and subsequently confirmed by others (5-7) that brain iron concentration is maximal in

---

[1] A version of this chapter has been submitted for publication. F.Q. Ye, P.S. Allen, W.R.W. Martin, Basal ganglia iron content in Parkinson's disease measured with magnetic resonance. *Movement Disorder* (1995).

globus pallidus, substantia nigra, red nucleus, caudate and putamen. Biochemical studies have reported increased iron content in substantia nigra from patients with PD or other neurodegenerative disorders affecting the basal ganglia (8-10) although others have reported conflicting observations (11). The degree of increase may be related to disease severity as indicated by the observation that there is little difference between controls and PD patients with mild pathology whereas in severe PD there is a highly significant increase of iron within the substantia nigra (12).

With conventional T_2-weighted magnetic resonance imaging (MRI), performed at a field strength of 1.5 T, reduced signal is normally evident from the substantia nigra, dentate nucleus, red nucleus, and globus pallidus (13). This decrease, in part related to a local increase in iron content, is multi-factorial and only partially separates PD patients from normal controls (14). To improve the in-vivo measurement of tissue iron content, we have developed an MRI method which quantifies the effects of paramagnetic centres sequestered inside cellular membranes (15). Because regional brain iron concentration is much greater than that of other paramagnetic ions such as manganese and copper (11), this method enables an index of tissue iron content to be calculated for basal ganglia substructures. This method exploits the dependence of the transverse magnetization decay on the interecho time in a train of 180° radio frequency pulses. This dependence is dominated by the local field inhomogeneities due to cellular sequestration of iron. We report here an application of this method in a series of normal controls and patients with PD in order to determine the relationship between basal ganglia iron content and the presence and symptomatic severity of PD. A preliminary report of this work has appeared previously (16).

6.2 Methods

6.2.1 Patients

Patients (n=12) were recruited from the Edmonton General Hospital/University of Alberta Movement Disorder Clinic. These patients all had a clinical diagnosis of PD with at least two of three cardinal manifestations, namely resting tremor, rigidity, and bradykinesia. None had other significant neurological abnormalities, including postural hypotension or clinical evidence of cerebellar dysfunction. All of these patients had a definite and prolonged symptomatic response to levodopa and were receiving levodopa/carbidopa at the time of this study. Clinical severity was estimated from the motor subscore (section 18-42) of the Unified Parkinson's Disease Rating Scale (UPDRS) (4), and functional capacity for activities of daily living was rated according to Schwab and England (2). These clinical assessments were performed while patients were "on". Patients ranged in age from 43 to 79 yr (mean ± SD = 63.9 ± 11.2 yr). A control group (n = 13) of neurologically normal individuals ranged from 40 to 79 yr of age (mean ± SD = 58.0 ± 12.5 yr).

One additional patient, age 54 yr, with a tentative diagnosis of striatonigral degeneration (SND) was studied. This patient had a history of gradually progressing bradykinesia, rigidity affecting the trunk and all limbs, and severe gait dysfunction with start hesitation, festination, and impaired postural reflexes. Thus far, she has not developed a rest tremor. By about 5 yr after the onset of symptoms, she was almost completely mute, had a markedly flexed posture with considerable anteropulsion, and required a walker when standing or walking. She has not had significant postural hypotension, or cerebellar abnormalities and her eye movements have remained normal. Although there was an initial benefit from levodopa/carbidopa 300/75 mg daily, by 4-5 yr after onset there was virtually no response to a daily dose of 1000/100 mg.

6.2.2 Magnetic Resonance Studies

To quantify the enhanced transverse relaxation of water protons due to local iron accumulation, a spin echo based sequence was used that permitted the initial imaging magnetization to be sensitized to the interecho time (or refocusing interval) dependence of the observable transverse magnetization decay rate R_{2app} ($1/T_{2app}$) by means of a preparatory sub-sequence (A detailed description of the image sequence is presented in Chapter 4). This sub-sequence consisted of a variable train of hard (non-selective) 180° refocusing pulses that provided a partially decayed transverse magnetization prior to the image acquisition part of the overall sequence. The image acquisition part employed a slice-selective refocusing pulse (slice thickness 5 mm) and a fixed echo time of 25 ms. Measurement were performed on a Philips GYROSCAN 1.5 T system using a standard head coil and 128 phase-encoding steps. Image field of view was 16 cm. T_1 effects were minimized by using a repetition time (TR) of 2200 ms. The phases of all 180° refocusing pulses were $\pi/2$ shifted from the excitation pulse. Three variants of the preparatory sub-sequence were used in combination in order to derive the interecho time dependence. The first variant provided the full transverse magnetization by means of a single 90° excitation pulse and no relaxation delay prior to the image acquisition sub-sequence. In the second variant, a single 180° pulse in a delay period of 60 ms followed the excitation pulse to provide a refocused, but partially decayed transverse magnetization. The third variant employed a train of ten 180° pulses, separated by an interecho time of 6 ms, to replace that single 180° pulse in the second variant but maintained the total decay time of 60 ms. From the data sets obtained with these sequence variants, two separate R_{2app} images were derived, each one reflecting a two point fit to R_{2app} at every pixel and using the first variant to provide the initial point in each case. By subtracting the two R_{2app} images, a δR_{2app} difference image was obtained.

Initially, a sagittal T_1-weighted image was employed to facilitate the selection of a single transverse slice parallel to and 5 mm above the line drawn from the anterior to the posterior commissure (the AC-PC line). Data were then acquired from this single slice using the methodology described above. The entire patient procedure took between 50 and 90 minutes.

6.2.3 Data Analysis

Numerical values were obtained from regions-of-interest (ROIs) which were initially located manually on the globus pallidus (GP), putamen (PM), caudate head (CD), and thalamus (TH) bilaterally by means of T_2-weighted images. These ROIs were then automatically transposed to the δR_{2app} images. Irregular ROIs were fitted to the structures in question to maximize the number of pixels (pixel size 1.25 x 1.25 mm^2) for each ROI. The average ROI sizes (± 1 SD) were 36 ± 10 pixels for GP, 61 ± 13 for PM, and 12 ± 4 for CD. A circular ROI (18 ± 5 pixels) was placed on the thalamus. To provide a reference in each individual studied, a large ROI (~2000 pixels) was defined that encompassed most of the slice but excluded the ventricles and basal ganglia. From this ROI, an average background δR_{2app} value was obtained. This background reflects any interecho time dependence of the magnetization decay due to mechanisms other than accumulated iron, and as such it was in lieu of measurements from basal ganglia structures devoid of iron. It should be noted that the effects of accumulated iron are an order of magnitude greater than those of other mechanisms showing an interecho time dependence. The background average allows for standardization against interscan variability. The numerical values of a regional ΔR_{2app} which are quoted below are the difference between the regional δR_{2app} and the average background value. Regional ΔR_{2app} provides an index for local tissue iron content.

The significance of any ΔR_{2app} difference between the control and PD groups was assessed with an unpaired t test. Linear regression analysis was used to determined whether ΔR_{2app} correlated with the clinical scores.

6.3 Results

Although the patient group was slightly older than the control group, this difference was not of statistical significance ($p = 0.22$). The regional ΔR_{2app} for the patient group was significantly elevated in GP ($p = 0.010$), in PM ($p = 0.014$) and in CD ($p = 0.014$). There was, however, no significant difference between the groups in regional ΔR_{2app} from the thalamus ($p = 0.163$). The quantitative data are summarized in Table 6.1. In controls, there was an increasing trend of ΔR_{2app} with increasing age in all regions examined, but this reached statistical significance only in the putamen ($p = 0.012$). There was no correlation between ΔR_{2app} and age in the PD group.

In the patient with presumed SND, ΔR_{2app} was substantially higher in both GP and PM than in either controls or PD. In PD, average putamenal ΔR_{2app} was increased over control values by about 42% as compared to almost 300% in the SND patient. Average pallidal ΔR_{2app} was increased over controls by about 33% in PD as compared to slightly over 200% in SND.

There was a significant association between clinical symptomatology and ΔR_{2app} in GP and PM, with the most severely affected patients having the highest regional ΔR_{2app} values. The UPDRS motor subscore ranged from 21 to 48 and showed a positive correlation with pallidal ΔR_{2app} values ($r = 0.72$, $p = 0.009$) but no significant correlation with ΔR_{2app} values from PM. Functional ability as indicated by the Schwab and England activities of daily living scale ranged from 30 to 90% and was inversely correlated with ΔR_{2app} in both GP ($r = -0.64$, $p = 0.025$) and PM ($r = -0.76$, $p = 0.004$).

These correlation relationships are presented in Figure 6.1. On the Schwab and England scale, lower scores are equated with higher disability whereas on the UPDRS, higher scores correlate with increased symptomatic severity. This explains the negative correlation with the Schwab and England scales and the positive correlation with the UPDRS. Caudate and thalamic ΔR_{2app} values were correlated with neither of the clinical measures of disease severity.

6.4 Discussion

We found a significant increase in iron content, as indicated by increased ΔR_{2app}, in the globus pallidus and putamen of patients with PD compared with healthy age-matched controls. In addition, there was a significant correlation between the increased iron content in globus pallidus and putamen and increased functional impairment and clinical severity of parkinsonian symptoms. Although we also observed a statistically significant (at the 95% level) difference in caudate ΔR_{2app}, we did not feel these measurements to be clinical significance because of methodological shortcomings applicable to the caudate ROI as discussed below.

6.4.1 MR methodology

The majority of previous MRI studies of brain iron content in patients with PD have employed T_2-weighted imaging or quantitative local T_2 measurements. With conventional T_2-weighted imaging at a field strength of 1.5 T, reduced signal is evident in the globus pallidus, red nucleus, dentate nucleus, and substantia nigra (13). The signal loss varies with the concentration of iron, the magnetic field strength, and the degree of T_2 weighting in the image. Although this reduction is caused in part by local increases in iron concentration, the resultant signal intensity in a T_2-weighted image is determined by a combination of mechanisms depending not only on the iron

distribution, but also on the heterogeneity of magnetic susceptibility in the cellular milieu of individual brain structures, and on the motional modulation of interproton dipolar interactions. Separating the effects of the iron from those of the other mechanisms is essential to the quantification of regional iron variations, since both in vitro and clinical studies have failed to show a consistent correlation between iron content and apparent T_2 (17-18).

In peripheral tissue, the largest single fraction of iron is stored in ferritin (5), a complex comprising a protein shell (apoferritin) surrounding a crystalline core of hydrous ferric oxide. Within the brain, ferritin and iron accumulates largely in glial cells, particularly in oligodendrocytes and microglia (6, 19), thus giving rise to a heterogeneous distribution of the iron because it is confined by the membranes of these cells. The iron-rich cells become paramagnetic centers whose magnetic dipole fields enhance the dephasing of transverse proton magnetization during an MR study.

There have been two experimentally observed characteristics of ferritin-induced proton relaxation which have important consequences for the development of a quantitative method of measuring regional brain iron content. The first of these is the field strength dependence of the proton transverse relaxation rate in ferritin solutions (20). The second is the interecho time dependence of the transverse relaxation when the ferritin is confined by intact cell membranes thus giving rise to a heterogeneous magnetic environment on the scale of the water diffusion path (21). The field dependence has been exploited by Bartzokis *et al.* (22), who found that in ferritin containing phantoms and also in live brain, the change in observed transverse relaxation rate between 0.5 and 1.5 T may be a specific measure of tissue ferritin. Use of the field dependence, however, suffers from the significant disadvantage for clinical studies of

requiring that comparative images be obtained in clinical MRI systems with at least two different field strengths.

At a single field strength, we have shown that interecho time dependence of the transverse decay can be used to provide a specific index of the tissue concentration of iron sequestered in cells (see Chapters 3 and 4). That index, ΔR_{2app}, is not subject to the same shortcomings as direct T_2-based methods because it separates the effects of iron from those of other transverse relaxation mechanisms. The ability to effect this separation arises from the magnitude and spatial scale over which the iron-rich glial cells produce field inhomogeneities, as compared with those which characterize either magnet generated inhomogeneities or susceptibility difference effects between tissue structures. These differences translate into temporal sensitivity (resolution) through the rate at which diffusing water molecules are able to sample the significant variations due to each inhomogeneity source. Because this diffusional displacement takes time, interecho time dependence of the magnetization decay results, a decay which is dominated by the field inhomogeneities due to the iron rich cells. Although ΔR_{2app} is itself echo time dependent, previous data show that for a fixed difference in interecho time, its value is specifically sensitive to the iron concentration (see Chapters 3 and 4). The subtraction of the two relaxation rate images separates out the interecho time dependent relaxation contributions and removes the intrinsic transverse relaxation terms which do not depend on interecho time but vary with local water content. The subtraction of a background to give ΔR_{2app} fulfills the goal of standardizing each result against normal brain variations and interscan variations, as well as removing the minor interecho time dependent decay terms arising from susceptibility differences between brain structures.

Several sources of experimental uncertainty potentially affect our results. Because our methodology employs subtraction to determine ΔR_{2app}, it is sensitive to head movement between data sets. This sensitivity is reflected by our inability to obtain reproducible values from small structures such as the substantia nigra. A second source of experimental uncertainty stems from the lack of dynamic range that our method has for accommodating the long T_2 of cerebrospinal fluid (CSF). This range is governed by the fixed 60 ms duration of the preparatory sub-sequence. Lack of dynamic range might have affected our ΔR_{2app} measurements in the caudate head because of the proximity of the lateral ventricles. Neither pallidal nor putamen measurements, however, should have been affected by either of these shortcomings.

An alternative method of separating out the relaxation effects of tissue iron has been reported recently (23). This employs a pair of multiecho sequences to facilitate subtraction of R_2 and R_2^*, and expose the iron-dependent component of the relaxation.

6.4.2 Iron in Parkinson's disease

The relevance of basal ganglia iron accumulation to the pathogenesis of PD is controversial. An early study by Earle, before the introduction of levodopa, suggested an increase in iron content in formalin-fixed sections of the midbrain in PD (8). Others have confirmed the presence of increased iron levels within the substantia nigra (9, 10) although this is a controversial finding (11). The degree of increase appears to be related to disease severity as indicated by the observation that there is no profound difference between controls and PD patients with mild pathology (7) whereas in severe PD (Hoehn and Yahr stage 4), there is a highly significant increase of iron within the substantia nigra (12). Ordidge *et al.* have recently reported increased nigral iron content in PD, measured with a novel MR technique implemented on a 3.0 Tesla magnet (23).

We were unable to study nigral iron content at the lower field strength of 1.5 T because the reduced signal to noise ratio rendered us more sensitive to motion artifacts. However, our results do suggest increased iron content in basal ganglia structures, namely the globus pallidus and the putamen, and moreover, suggest that the degree of increase in these structures is also related to disease severity. We postulate that increased iron accumulation in the putamen is related to pathology affecting nigrostriatal neurons projecting to this structure. The relationship between iron and clinical symptomatology suggests increasing iron content with disease progression. We presume the iron is primarily in glial cells (oligodendrocytes) on the basis of post postmortem studies in normal individuals (19), but its cellular localization in PD has not been directly addressed. Glial iron accumulation may be a secondary response to cell death in the nigrostriatal neuronal system. Increased nigral iron content has been reported in other basal ganglia diseases with nigral destruction such as progressive supranuclear palsy and multiple system atrophy (24), indicating that this increase is not specific to PD. Dexter *et al.* (24) have suggested the possibility of increased iron uptake, via the transferrin receptor, by cells exposed to metabolic stress. This is supported by work suggesting an upregulation of transferrin receptors on surviving neurons in MPTP treated mice (25), and by the reported increase in transferrin receptors and iron uptake associated with regenerating motor neurons (26).

An alternative possibility is that the increased iron is causally related to the disease process itself. Free iron can be highly damaging to structural membrane components, possibly by lipid peroxidation secondary to increased production of free oxygen radicals, and on this basis a role for iron in the etiology of PD has been proposed (12, 27). As previously noted, the majority of iron in peripheral tissues which is not involved in biochemical reactions is bound in a non-reactive form of ferritin (5). It is not known what percentage of basal ganglia iron in the normal or PD brain is

bound to ferritin or how much is present in a free and reactive form. Our methodology does not allow us to determine non-invasively in what form the increased basal ganglia iron exists.

Of interest is our observation of increased pallidal iron in PD. In vitro measurements of pallidal iron in PD have produced conflicting results with Dexter *et al.* (24) reporting a decrease and Chen *et al.* (18) reporting an increase. The globus pallidus is not generally recognized as being involved in the pathology of PD although there is evidence of some mild neuronal loss in its external segment (28). There is a sparse plexus of dopamine-containing nerve terminals in the globus pallidus, collateral from the nigrostriatal pathway (29). Even if there is significant pathology in these few terminals in PD, it seems unlikely that this could account for the prominent ΔR_{2app} abnormalities which we observed. The pallidal abnormalities were also related to the severity of clinical symptomatology to an extent which was similar to that of the putamen changes. This might indicate a more general abnormality related to brain iron metabolism in PD. The globus pallidus is one of the brain regions which is known to have a high concentration of iron in normal subjects. It would be of interest to study other regions, such as the red nucleus and the dentate nucleus, which are also known to have a high iron content, but which are not generally associated with the pathology of PD.

Increased nigral iron content has also been reported previously in other basal ganglia diseases associated with nigral destruction such as progressive supranuclear palsy and multiple system atrophy (MSA) (24), indicating that this increase is not specific to PD. Our observations in a single patient with presumed SND support this finding and indicate a substantial quantitative difference in basal ganglia iron content between PD and SND, particularly in the putamen. This is consistent with the reported

correlation of the changes on T[illegible]ghted imaging with direct post-mortem measurements of iron content in SND (30).

Could our results be affected by the inadvertent inclusion of patients with MSA (and the associated high basal ganglia iron content) in the PD group? The differential diagnosis of akinetic movement disorders during life can be difficult with the diagnosis of PD being incorrect in as many as 20% of patients (31). We think this to be an unlikely source of error in the present study for several reasons. First, none of our patients had major clinical features (other than parkinsonism) associated with either the Shy-Drager or olovopontocerebellar atrophy variants of MSA. Second, the two patients with the highest pallidal iron content, approaching that seen in probable SND, had been symptomatic and clearly levodopa-responsive for 11 and 18 years, unlike the history expected in SND. Lastly, we observed the putamenal iron content in probable SND to be much greater than that in any of the PD group, supporting our impression that the PD patients were distinct from the one individual with probable SND.

In summary, we have implemented a novel, non-invasive MRI technique to quantify changes in iron content in the basal ganglia in PD. We have demonstrated a significant increase in an index of local iron content, ΔR_{2app}, in the striatum and pallidum of PD patients, and have shown these changes to correlate with the severity of clinical symptomatology. Although these changes may not be specific for PD, the correlation with clinical severity suggests the possibility of applying this method in serial studies of disease progression. Future implementation with a system of higher magnetic field strength (e.g., 3.0 T) should improve the signal to noise ratio, thereby enabling faster studies to be performed, lessening the artifact induced by patient movement, and allowing assessment of smaller structures such as the substantia nigra.

Table 6.1.
Regional ΔR_{2app} (mean ± SD, in s^{-1}) in patients and controls.

Regions	Normal controls (n = 13)	Parkinson's disease (n = 12)	Striatonigral degeneration (n = 1)
Putamen	1.29 ± 0.59	1.83 ± 0.46 *	3.79
Globus pallidus	2.13 ± 0.48	2.83 ± 0.65 *	4.33
Caudate	0.60 ± 0.35	0.91 ± 0.37*	0.80
Thalamus	0.26 ± 0.22	0.49 ± 0.38	0.39

* significantly different from normal controls at the 95% level of significance.

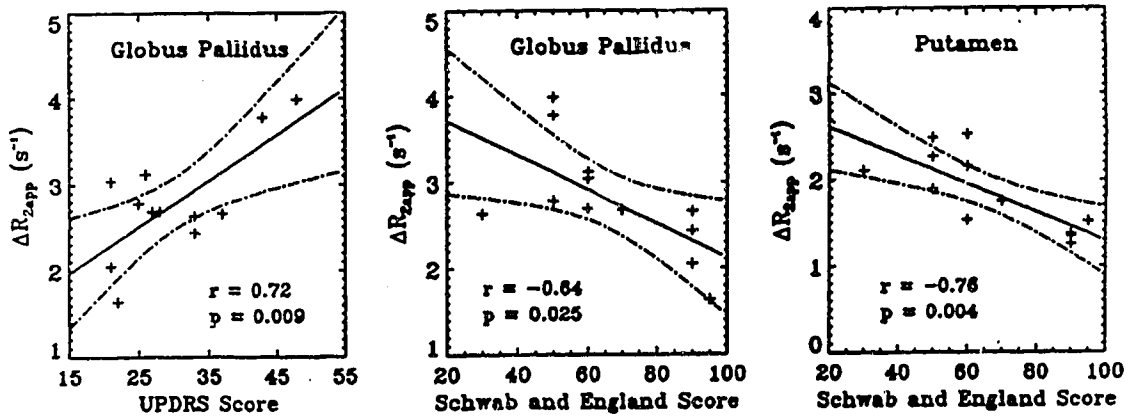

a. b. c.

Figure 6.1. The correlation between the regional ΔR_{2app} and the assessment of clinical symptomatology. a. pallidal ΔR_{2app} versus UPDRS motor score; b. pallidal ΔR_{2app} versus Schwab and England activities of daily living score; c. putamen ΔR_{2app} versus Schwab and England activities of daily living score. The regression lines (solid) and 95% confidence limits (dot dashed) are indicated.

6.5 References

1 M.M Hoehn, M.D. Yahr, Parkinsonism: onset, progression and mortality. *Neurology (NY)* 17, 427-442 (1967).

2 R. S. Schwab, A. C. England, in "Third Symposium on Parkinson's Disease" (F. J. Gillingham, I. M. L. Donaldson, eds.), p152-157, Livingstone, Edinburgh, 1969.

3 R.C. Duvoisin, The evaluation of extrapyramidal disease, *in* "Monoamines: noyaux gris centraux et syndrome de Parkinson" (J. de Ajuriagerra, Eds.), pp313-325, 1970.

4 S. Fahn, R. L. Elton, in "Recent Developments in Parkinson's Disease" (S. Fahn, R. L. Elton, eds.), vol 2, pp153-163, Macmillan, Florham Park, 1987.

5 B. Hallgren, P. Sourande, The effect of age on the non-haemin iron in the human brain. *J Neurochem* 3, 41-51 (1958).

6 J. M. Hill, R. C. Switzer, The regional distribution and cellular localization of iron in the rat brain. *Neuroscience* 11, 595-603 (1984).

7 P. Riederer, E. Sofic, W.D. Rausch, B. Schmidt, P. G.P. Reynolds, K. Jellinger, M.B.H. Youdim, Transition metal, ferritin, glutathione, and ascorbic acid in parkinsonian brains. *J Neurochem* 52, 515-520 (1989).

8 K.M. Earle, Studies on Parkinson's disease including x-ray fluorescent spectroscopy of formalin fixed brain tissue. *J Neuropathol Exp Neurol* 27, 1-14 (1968).

9 D.T. Dexter, F.R. Wells, A.J. Lees, F. Agid, P. Jenner, C.D. Marsden, Increased nigral iron content and alterations in other metal ions occurring in brain in Parkinson's disease. *J Neurochem* 52, 1830-1836 (1989).

10 E. Sofic, P. Riederer, H. Heinsen, H. Beckmann, G.P. Reynolds, G. Hebenstreit, M.B.H. Youdim, Increased iron (III) and total iron content in post mortem substantia nigra of parkinsonian brain. *J Neural Transm* 74, 199-205 (1988).

11 R.J. Uitti, A.H. Rajput, B. Rozdilsky, M. Bickis, T. Wollin, W.K. Yuen, Regional metal concentrations in Parkinson's disease, other chronic neurological diseases, and control brains. *Can J Neurol Sci* 16, 310-314 (1989).

12 M.B.H. Youdim, D. Ben-Schachar, S. Yehuda, P. Riederer, *in* "Advances in Neurology, Vol 53: Parkinson's Disease: Anatomy, Pathology and Therapy" (M.B. Streifler, *et al.*, Eds), pp155-162, Raven Press, New York, 1990.

13 B. Drayer, P. Burger, R. Darwin, S. Riederer, R. Herfkens, G. A. Johnson, MRI of brain iron. *AJR* 147, 103-110 (1986).

14 A. Antonini, K.L. Leenders, D. Meier, W.H. Oertel, P. Boesiger, M. Anliker, T2 relaxation time in patients with Parkinson's disease. *Neurology* 43, 697-700 (1993).

15 F.Q. Ye, W.R.W. Martin, J. Hodder, P.S. Allen, Brain iron imaging exploiting heterogeneous-susceptibility-enhanced proton relaxation. *in* "Proc., SMR, 2nd Annual Meeting, San Francisco, 1994," p. 5.

16 W.R.W. Martin, F.Q. Ye, J. Hodder, P.S. Allen, Putamenal iron content in Parkinson's disease measured by nuclear magnetic resonance imaging. *Ann Neurol* 36, p. 280A (1994).

17 J.C. Chen, P.A. Hardy, M. Clauberg, G. Joshi, J. Parravano, J.H.N. Deck, R.M. Henkelman, L.E. Becker, W. Kucharczyk, T_2 values in the human brain: comparisor with quantitative assays of iron and ferritin. *Radiology* 173, 521-526 (1989).

18 J.C. Chen, P.A. Hardy, W. Kucharczyk, M. Clauberg, G. Joshi, A. Vourlas, M. Dhar, R.M. Henkelman, MR of human postmortem brain tissue: correlative study between T_2 and assays of iron and ferritin in Parkinson and Huntington disease. *AJNR* 14, 275-281 (1993).

19 J.R. Connor, S.L. Menzies, S.M. St. Martin, E.J. Mufson, Celluar distribution of transferrin, ferritin and iron in normal and aged human brains. *J Neurosci Res* 27, 595-611 (1990).

20 J. Vymazal, R.A. Brooks, O. Zak, C. McRill, C. Shen, G. Di Chiro, T1 and T2 of ferritin at different field strengths: effect on MRI. *Magn Reson Med* 27, 368-374 (1992).

21 F.Q. Ye, P.S. Allen, Ferritin as a Susceptibility Agent, *in* "Proc., SMRM, 12th Annual Meeting, New York, 1993," p. 800.

22 G. Bartzokis, M. Aravagiri, W.H. Oldendorf, J. Mintz, S.R. Marder, Field dependent transverse relaxation rate increase may be a specific measure of the tissue iron stores. *Magn Reson Med* 29, 459-464 (1993).

23 R.J. Ordidge, J.M. Gorell, J.C. Deniau, R.A. Knight, J.A. Helpern, Assessment of relative brain iron concentration using T2-weighted and T2*-weighted MRI at 3T. *Magn Reson Med* 32, 335-341 (1994).

24 D.T. Dexter, P. Jenner, A.H.V. Schapira, C.D. Marsden, Alterations in levels of iron, ferritin and other trace metals in neurodegenerative diseases affecting the basal ganglia. *Ann Neurol* 32, S94-S100 (1992).

25 D.C. Mash, J. Sanchez-Ramos, W.J. Weiner, Distribution and number of transferrin receptors in Parkinson's disease and the MPTP-treated mice. *Ann Neurol* 28, 230-231 (1990).

26 M.B. Graeber, G. Raivich G.W. Kreutzberg, Increase of transferrin receptors and iron uptake in regenerating motor neurons. *J Neurosci Res* 23, 342-345 (1989).

27 M.B.H. Youdim, D. Ben-Schachar, P. Riederer, Is Parkinson's disease a progressive siderosis of substantia nigra resulting in iron and melanin induced neurodegeneration? *Acta Neurol Scand* 80 (Suppl 126), 47-54 (1989).

28 K. Jellinger, Overview of morphological changes in Parkinson's disease. *in* "Advances in Neurology, Vol 45: Parkinson's Disease" (M.D. Yahr, K.J. Bergmann, Eds.), pp1-18, Raven Press, New York, 1987.

29 O. Lindvall, A. Bjorklund, Dopaminergic innervation of the globus pallidus by coliaterals from the nigrostriatal pathway. *Brain Res* 172, 169-173 (1979).

30 A.E. Lang, T. Curran, J. Provias, C. Bergeron, Striatonigral degeneration deposition in putamen correlates with te slit-like void signal of magnetic resonance imaging. *Can J Neurol Sci* 21, 311-318 (1994).

31 A.J. Hughes, S.E. Daniel, L. Kilford, A.J. Lees, Accuracy of clinical diagnosis of idiopathic PD. *J Neurol Neurosurg Psychiatry* 55, 181-184 (1992).

CHAPTER 7

General Discussion and Conclusions

7.1 General Discussion and Conclusions

The principal motivation of this work was to develop a non-invasive technique for measuring the changes in brain iron due to Parkinson's disease. To do this, it was necessary to investigate the relaxation enhancement effect of brain iron on the water protons, so as to develop an MRI method for the non-invasive quantification of brain iron deposition.

At the beginning this study, in late 1991, T_2-shortening seen in the basal ganglia nuclei on MR images had been interpreted as the result of iron deposition (1,2). However, because no consistent correlation could be found between the iron concentration of excised tissue and the transverse relaxation time (3), it was realized that reliable iron quantification could not be obtained with simple T_2-imaging. Moreover, the mechanism postulated for the transverse relaxation enhancement in brain (1,4,5) was largely based on the modelling of relaxation enhancement in ferritin solutions (6,7), a model which did not take into account the enhancement effect of the heterogeneous glial sequestration of iron and ferritin (8).

Based on previous biomedical observations of an interecho time dependence of the transverse magnetization decay, e.g., in deoxygenated blood (9) and in liver injected with superparamagnetic iron oxide contrast agent (10), we postulated that the heterogeneous glial sequestration of paramagnetic iron would give rise to local, microscopic field inhomogeneities over distances of a few tens of microns, that would in turn produce an interecho time, Δ_{180}, dependence of the transverse relaxation of the water protons in iron-rich brain. We further postulated that this interecho time dependence of

the apparent transverse relaxation rate, R_{2app}, would provide a quantitative measure of the sequestered iron.

The postulated mechanism of the relaxation enhancement was systematically studied (both experimentally and theoretically) using an experimental model system of paramagnetic suspensions of red blood cells (RBC). This study is described in Chapter 2. The mechanism when incorporated into a computer simulation of the experimental data reproduced the dependencies of the transverse relaxation enhancement on Δ_{180}, on the intra/extra cellular magnetization difference ΔM, and on changes in cell shape (Figures 2.1, 2.2, and 2.4). The degree of consistency between theory and experiment augurs well for the validity of the mechanism. However, a very recent publication (11) showing the ability of a very different model to provide a similar consistency with one aspect of the data, namely, the interecho time dependence, means that further experiments will be required to clarify the ambiguity between a single cell model and a multicell model. Notwithstanding the dichotomy over the role of transmembrane passage when the cells are far from spherical, the cells which sequester iron in brain tissue, namely oligodendrocytes, are generally round in shape, and any uncertainties surrounding the role of shape distortions for RBC are far less important in iron-rich brain tissue.

The ability of the Δ_{180}-dependent enhancement of R_{2app} to reflect the different iron content of various brain structures was confirmed next from normal postmortem basal ganglia grey matter. The evaluation is reported in Chapter 3, where a correlation between a measure of the relaxation enhancement, δR_{2app}, and iron concentration at the 99% level of significance is described. It was clear from this in-vitro study that at 2.35 T, see Figure 3.2, the relaxation enhancement was sensitive enough to distinguish the globus pallidus and possibly the putamen from each other and from the other brain

structures even with the small sample size of 5 brains and even when the brains had shown no evidence of iron-accumulating disease.

To implement an imaging method for the in-vivo quantification of iron based on the τ_{180}-dependence of R_{2app}, a spin echo sequence was modified to include a preceding CPMG stage for the preparation of the transverse magnetization (Figure 4.1). The efficacy of the imaging sequence at 1.5 T was tested both on phantoms and on a group of age-range-limited healthy controls. Over a relevant but limited range of magnetization difference values, the phantom study demonstrated a linear dependence of δR_{2app} on the internal magnetization difference with a sensitivity of ~ $2s^{-1}A^{-1}m$. In the group of 11 healthy subjects, δR_{2app} proved capable of distinguishing quantitatively certain iron-rich basal gangiia structures. Among four brain structures that were analyzed, the precision of δR_{2app} was sufficient to distinguish the globus pallidus and the putamen from each other and from the two other structures of lesser iron content (i.e., the thalamus and frontal white matter), at the 99% level of significance. This study is presented in Chapter 4.

A different imaging protocol for the relative assessment of brain iron concentrations has recently been presented by Ordidge *et al.* (12). Their method was based on a difference between R_2- and R_2^*- weighted images to derive a regional line broadening effect, R_2'. Because R_2^* is more sensitive than R_2 to the local field inhomogeneities, so R_2' might be expected to be more sensitive than δR_{2app} to brain iron deposition. Our reason for choosing R_2 contrast instead of R_2^* contrast was to avoid some significant artifacts on R_2^*-weighted images that arose from global field inhomogeneities. Ordidge *et al.* (12) overcame this problem with a novel technique of field inhomogeneity correction which requires for its implementation a series of several images.

Our second in-vivo application was to a group of normal adult volunteers whose ages spanned a range of 5 decades. In the putamen and in the caudate head of these volunteers, significant increases in a second measure of the relaxation enhancement, ΔR_{2app}, were found that correlated with increasing age (ΔR_{2app} is not quite identical to δR_{2app}, because it incorporates some background subtraction, see Chapter 5). The correlation coefficients for the two regions were respectively r = 0.76 and r = 0.69 (Figures 5.1 and 5.2). The possibility of measuring age-related human brain iron variations raises the intriguing question of whether or not this method can be of value for testing the role of iron in promoting the free radical mediated neuronal damage.

The third in-vivo application was a preliminary clinical study of patients with Parkinson's disease (see Chapter 6). Twelve patients with Parkinson's disease were compared with age-matched controls. It was observed that the patient group displayed an average 42% increase over the normal group in ΔR_{2app} in the putamen and a similar 33% increase in the globus pallidus (Table 6.1). The ΔR_{2app} in these two structures also correlated with the severity of clinical symptomatology and functional impairment at the 95% level of significance, with the more severely affected patients having the higher ΔR_{2app} values (Figure 6.1). The results give us optimism that with a more thorough testing, and at the higher field strength of 3 T, ΔR_{2app} may provide a quantitative, non-invasive correlate with the severity of the pathological changes underlying Parkinson's disease. Ordidge *et al.* working at 3 T found a more dramatic increase in the relative iron content in the substantia nigra of a group of patients with Parkinson's disease (12). The substantia nigra was not exploited in our study because of its small volume and our lack of an effective means of accommodating small scale motion artifacts.

As a result of the concurrent and independent work on the measurement of brain iron, there is at the present time significant promise that a non-invasive index of brain

iron is at hand. That is not to say that further improvements could not be made. With reference to this study, for example, the field calculation of Chapter 2 could be reprogrammed to handle the non-spherical cell surface numerically. The simulation would then naturally include all three types of water diffusion in the overall relaxation enhancement evaluation. A snapshot fast imaging sequence should be implemented to replace the standard spin echo sequence for imaging the pre-prepared transverse magnetization. It would effectively speed up the imaging acquisition and make the method less prone to subject movement. It would be even better if a R_2*-weighted image could be acquired by simply disabling the hard refocussing pulses in the preparatory sequence, then both δR_{2app} and R_2' could be obtained by adding only one new image data set. To do this however, the large artifacts from global field inhomogeneity on T_2*-weighted image would first need to be removed (12)

Further study is still required on the proposed relaxation enhancement model in iron-rich brain tissues, and a few fundamental questions remain to be answered. For example, how much does brain iron contribute to R_{2app}, and what proportion of that contribution is interecho time dependent or field strength dependent? Is there a significant portion of brain iron in a non-paramagnetic form and therefore not capable of affecting proton relaxation? To what absolute precision can brain iron be quantified with MR relaxation methods? Clear answers to these questions would really establish if MRI can provide a reliable, quantitative measure for iron concentration or only a relative index of brain iron changes.

7.2 References

1 B. Drayer, P. Burger, R. Darwin, S. Riederer, R. Herfkens, G. A. Johnson, MRI of brain iron. *AJR* 147, 103-110 (1986).

2 B.P. Drayer, Basal ganglia: significance of signal hypointensity on T2-weighted MR images. *Radiology* 173, 311-312 (1989).

3 J.C. Chen, P.A. Hardy, M. Clauberg, G. Joshi, J. Parravano, J.H.N. Deck, R.M. Henkelman, L.E. Becker, W. Kucharczyk, T_2 values in the human brain: comparison with quantitative assays of iron and ferritin. *Radiology* 173, 521-526 (1989).

4 J. N. Rutledge, S. K. Hilal, A. J. Silver, R. Defendini, S. Fahn, Study of movement disorders and brain iron by MR. *AJNR* 8, 397-411 (1987).

5 A. Bizzi, R. A. Brooks, A. Brunetti, J. M. Hill, J. R. Alger, R. S. Miletich, T. L. Francavilla, G. Di Chiro, Role of iron and ferritin in MR imaging of the brain: a study in primates at different field strengths. *Radiology* 177, 59-65 (1990).

6 S.H. Koenig, R.D. Brown III, J. F. Gibson, R. J. Ward and T. J. Peters, Relaxometry of ferritin solutions and the influence of the Fe^{3+} core ions. *Magn Reson Med* 3, 755-767 (1986).

7 P. Gillis and S.H. Koenig, Transverse relaxation of solvent protons induced by magnetized spheres: Application to ferritin erythrocytes and magnetite. *Magn. Reson. Med.* 5, 323-345 (1987).

8 R. Connor, S.L. Menzies, S.M. St. Martin, E.J. Mufson, Celluar distribution of transferrin, ferritin and iron in normal and aged human brains. *J Neurosci Res* 27, 595-611 (1990).

9 K.R. Thulborn, J.C. Waterton, P.M. Matthews, and G.K. Radda, Oxygenation dependence of the transvers relaxation time of water protons in whole blood at high field. *Biochem. Biophys. Acta* 714, 265-270 (1982).

10 S. Majumdar, S.S. Zoghbi, J.C. Gore, The influence of pulse sequence on the relaxation effects of superparamaganetic iron oxide contrast agents. *Magn Reson Med* 10, 289-301(1989).

11 P. Gillis, S. Peto, F. Moiny, J. Mispelter, C.A. Cuenod, Proton transverse nuclear magnetic relaxation in oxidized blood: a numerical approach. *Magn. Reson. Med.* 33, 93-100 (1995).

12 R.J. Ordidge, J.M. Gorell, J.C. Deniau, R.A. Knight, J.A. Helpern, Assessment of relative brain iron concentrations using T_2-weighted and T_2*-weighted MRI at 3.0 T. *Magn. Reson. Med.* 32,335-341 (1994).